

---

**pH-Triggered Assembly/Disassembly  
of Magnetic Nanoparticles  
and Directed Assembly of Magnetic  
Nanocapsules  
in Polymer Films**

---

Diplomarbeit zur Erlangung des Grades  
eines Diplom-Chemikers  
im Fachbereich Chemie, Pharmazie und Geowissenschaften  
der Johannes Gutenberg-Universität Mainz  
vorgelegt von  
Jochen Eckhard Willersinn  
geboren am 19.09.1988  
in Mainz

Mainz 2014

This thesis was performed under the supervision of Prof. Dr. Katharina Landfester between December 2013 and August 2014 at the Max Planck Institute for Polymer Research in Mainz.

# Contents

<b>1</b>	<b>Introduction</b>	<b>1</b>
<b>2</b>	<b>Theory</b>	<b>3</b>
2.1	Colloids . . . . .	3
2.1.1	Emulsions . . . . .	3
2.1.2	Stability of emulsions . . . . .	4
2.1.3	Emulsion polymerization . . . . .	5
2.2	Hybrid nanoparticles . . . . .	6
2.3	Magnetism . . . . .	9
2.3.1	Magnetic induction and magnetization . . . . .	9
2.3.2	Magnetic flux density . . . . .	9
2.3.3	Susceptibility and permeability . . . . .	10
2.3.4	Magnetic and shape anisotropy . . . . .	11
2.3.5	Magnetism of small particles . . . . .	12
2.4	Magnetic alignment of nanoparticles and their complexing . . . . .	12
2.5	Self-Healing . . . . .	13
<b>3</b>	<b>Results and Discussion</b>	<b>15</b>
3.1	Oleate capped Fe <sub>3</sub> O <sub>4</sub> nanoparticles . . . . .	15
3.2	Magnetic Spherical Colloidal Building Blocks . . . . .	17
3.2.1	Synthesis of the magnetite containing polystyrene nanoparticles . . . . .	17
3.2.2	Size-separation of the magnetite containing polystyrene nanoparticles . . . . .	21
3.2.3	Attempts on creating nanochains with magnetic polystyrene nanoparticles . . . . .	27
3.2.4	Conclusion . . . . .	29
3.3	pH-triggered assembly/disassembly of magnetic polystyrene nanoparticles . . . . .	30
3.3.1	Synthesis of <i>N</i> -methyl-diaminoethyl functionalized magnetic nanoparticles . . . . .	30
3.3.2	Synthesis of <i>N</i> -methyl-diaminoethyl functionalized nanoparticles stabilized with Lutensol AT 50 . . . . .	33
3.3.3	<i>Tert</i> -butyloxycarbonyl protection of 4-[ <i>N</i> -(Methylaminoethyl)aminomethyl]styrene and nanoparticle synthesis . . . . .	34
3.3.4	Deprotection of the protected nanoparticles . . . . .	37
3.3.5	Chain formation of <i>N</i> -methyl-diaminoethyl functionalized nanoparticles with copper complexing . . . . .	38
3.3.6	Examination of the influence of ultrasound and base on the nanochain dispersion . . . . .	42
3.3.7	Nanochain formation with Nanoparticles stabilized with Lutensol AT 50 . . . . .	47
3.3.8	pH triggered disassembly of the nanochains . . . . .	48
3.3.9	Reassembly of <i>N</i> -methyl-diaminoethyl functionalized nanoparticles . . . . .	54
3.3.10	Conclusion . . . . .	55

---

3.4	Magnetic nanocapsule synthesis and polymer film formation . . . . .	56
3.4.1	Synthesis of magnetic nanocapsules . . . . .	56
3.4.2	Synthesis of the magnetic nanocapsules containing DCPD . . . . .	61
3.4.3	Magnetic polymer films . . . . .	61
3.4.4	Conclusion . . . . .	74
3.5	Superamphiphobic Surfaces Containing Magnetic Spherical Colloidal Building Blocks . . . . .	75
3.5.1	First Setup . . . . .	75
3.5.2	Second Setup . . . . .	76
3.5.3	Third Setup . . . . .	76
3.6	Conclusion . . . . .	77
<b>4</b>	<b>Summary and Outlook</b>	<b>79</b>
<b>5</b>	<b>Apparatus and Methods</b>	<b>82</b>
5.1	Centrifugation . . . . .	82
5.2	Dynamic Light Scattering (DLS) . . . . .	83
5.3	Electron microscopy . . . . .	84
5.3.1	Transmission electron microscope (TEM) . . . . .	84
5.3.2	Scanning electron microscope (SEM) and X-ray analysis . . . . .	84
<b>6</b>	<b>Experimental Part</b>	<b>86</b>
6.1	Synthesis of oleate capped $\text{Fe}_3\text{O}_4$ nanoparticles . . . . .	86
6.2	Magnetic spherical colloidal building blocks . . . . .	86
6.2.1	Synthesis of magnetic polystyrene nanoparticles . . . . .	86
6.2.2	Size-separation of magnetic polystyrene nanoparticles . . . . .	87
6.2.3	Chain formation with magnetic polystyrene nanoparticles . . . . .	87
6.3	Synthesis of <i>N</i> -methyl-diaminoethyl derived polystyrene magnetic nanoparticles	87
6.3.1	Synthesis of the <i>N</i> -methyl-diaminoethyl magnetic nanoparticles . . .	88
6.3.2	Synthesis of Lutensol AT 50 stabilized <i>N</i> -methyl-diaminoethyl functionalized magnetic nanoparticles . . . . .	88
6.3.3	<i>tert</i> -butyloxycarbonyl protection of 4-[ <i>N</i> -(methylaminoethyl) aminomethyl] styrene . . . . .	88
6.3.4	Synthesis of <i>tert</i> -butyloxycarbonyl-protected <i>N</i> -methyl-diaminoethyl-functionalized magnetic nanoparticles . . . . .	89
6.3.5	Deprotection of Boc-protected <i>N</i> -methyl-diaminoethyl-functionalized magnetic nanoparticles . . . . .	89
6.3.6	Chain formation of <i>N</i> -methyl-diaminoethyl functionalized magnetic nanoparticles with copper complexing . . . . .	89
6.3.7	Chain formation of <i>N</i> -methyl-diaminoethyl functionalized nanoparticles stabilized with Lutensol with copper complexing . . . . .	90
6.3.8	pH triggered disassembly of the nanochains . . . . .	90
6.3.9	Reassembly of the nanoparticles . . . . .	90

---

6.4	Synthesis of magnetic nanocapsules and polymer film formation . . . . .	91
6.4.1	Synthesis of magnetic polystyrene nanocapsules . . . . .	91
6.4.2	Synthesis of magnetic nanocapsules containing DCPD and hexadecane	91
6.4.3	Synthesis of P(MMA- <i>co</i> -BA) nanoparticles . . . . .	92
6.4.4	Polymer-film formation . . . . .	92
6.5	Superamphiphobic surfaces with magnetic spherical colloidal building blocks	92
6.5.1	First Setup . . . . .	92
6.5.2	Second Setup . . . . .	93
6.5.3	Third Setup . . . . .	94
6.6	Chemicals . . . . .	95
6.7	Devices and methods . . . . .	97

## 1 Introduction

The use of hybrid nanocomposites is of increasing interest for many applications in energy conversion and storage [1, 2, 3, 4], optical and electronic sensors, life sciences [5, 6], and the use of polymer films and composite materials.

One-dimensional structures in nanometer and micrometer scale are attractive for possible applications in energy conversion and energy storage, and surface coating.[7] These structures are usually synthesized using electrospinning [8, 9] processes or template assisted methods.[10, 11] A simple and versatile method is the directed self-assembly of nanoparticles.[12, 13] With the magnetic directed assembly of magnetic nanoparticles, linear assemblies can be easily created using an external magnetic field. The fusing of nanoparticles in one-dimensional structures with a variety of morphologies can be obtained with magnetic hybrid polystyrene nanoparticles, which exhibit a fusing behavior above the glass transition temperature.[14] Once assembled, the one-dimensional structures are not able to adapt to a change in the requirements of the application. Therefore, systems offering a reversible locking mechanism for the linear alignment of the magnetic nanoparticles are of high interest. The assembled linear structures can disassemble by an external trigger. This was already demonstrated for a redox-responsive locking system based on an iron-hydroxamate complex responsive to the presence of a reducing agent.[15] Another possibility is a pH sensitive assembly/disassembly system using magnetic hybrid nanoparticles fused by a complex.[16] Assembly/disassembly of linear systems of gold nanoparticles coated with nanobrushes, which were sensitive to changes in pH has already been reported.[17] A novel pH sensitive system of magnetic hybrid nanoparticles with a copper amine complex based to the  $[\text{Cu}(\text{en})_2]^{2+}$  complex was developed. It is reported that polymers containing this functionality possess the ability to complex transition metal ions and form linked structures.[18, 19] Magnetic hybrid nanoparticles containing *N*-methyl-diaminoethyl functionalities were synthesized and their ability to form linear chains by the formation of a copper complex in a magnetic field was studied. Furthermore, the pH dependent disassembly of formed the nanochains was investigated.

The interests in polymer films and polymer coatings in were steadily increasing recently [20, 21, 22]. The development of novel materials and the protection of these materials is of high interest in this field.

Besides the protective use of polymer coatings, polymer materials containing inorganic components such as silver or iron oxide show promising properties for the application in solar cells [23], data storage systems [24], and sensing.[25] Using magnetic nanocomposites expands the applicative possibilities to microelectronic materials [26], display units [27], optical-, and electronic sensors.[28] The directed linear alignment of magnetic particles in the composite material can be performed by the application of an external magnetic field.[29, 30]

Self-healing agents, such as polymers or capsules can be incorporated into the polymer composites to improve their durability.[31, 32, 33] The incorporation of self-healing materials allows the cure of damaged areas in the composite material, such as cracks or fractures. Another possibility is the use of magnetic materials in magnetorheological elastomers as self-healing stimulus.[34]

A combination of nanocapsules containing self-healing agents and magnetic nanocapsules

provides a method to improve the long-term self-healing efficiency of materials. The incorporation of extrinsic self-healing agents leads to a homogeneous distribution of the carriers. Exposed areas of the composite material that are more susceptible to damages need a higher concentration of self-healing agent to maintain their long-term stability similar to the rest of the composite material. The directed alignment of magnetic nanocapsules containing a self-healing agent in a polymer film is a possible solution for this problem.

This thesis aims to explore the merging behavior of magnetic nanoparticles aligned with different triggers and to extend the magnetic alignment of nanomaterials to novel fields. Four different projects were investigated:

- Size dependent merging behavior of magnetic polystyrene nanoparticles. Different size distributions of magnetic nanoparticles were prepared by centrifugation and the merging behavior of different size combinations was studied.
- pH-triggered assembly/disassembly of magnetic nanoparticles. The nanoparticles were functionalized with a pH dependent locking system.
- Synthesis of magnetic nanoparticles was extended to magnetic nanocapsules. The nanocapsules were incorporated in a polymer film and the alignment of the nanocapsules in the polymer film with a permanent magnetic field present was investigated.
- Finally, the formation of superamphiphobic surfaces with magnetic polystyrene nanoparticles was investigated

## 2 Theory

The following chapter deals with the theoretical considerations of physical and chemical topics, which are important to understand the topic of the thesis. Beginning with description of colloidal systems, emulsions and the synthesis of hybrid polymer dispersions, this chapter also explains the differences between particle and capsule formation, and the principles of magnetism and polymer self-healing.

### 2.1 Colloids

Colloids are ubiquitous in the surrounding environment, as in form of pigments, fog or even during the preparation of wine. They are heterogeneous systems where a material is dispersed in another material, called the continuous phase.[35] All physical state combinations except gas in gas are possible, as shown in Table 1.

**Table 1:** Various colloidal systems and their physical state.

Description	Continuous phase	Dispersed phase	Example
mixture	solid	solid	polymer blends
solid dispersion	solid	liquid	doped crystals
solid foam	solid	gaseous	aerogels, pumice
dispersion / suspension	liquid	solid	pigment, ink
emulsion	liquid	liquid	milk
foam	liquid	gaseous	soap foam
aerosol	gaseous	solid	smoke
aerosol	gaseous	liquid	fog

The size of a colloid can vary from several micrometers to the nanometer scale. For a colloid with a size of few nanometers, a real solution with a homogeneously distributed material is obtained instead of a dispersion. Unlike transparent solutions, a dispersion of nanoparticles of a diameter above 30 nm is usually cloudy. The reason for this is that light is scattered at the larger nanoparticles, which causes a cloudiness of the dispersion.

#### 2.1.1 Emulsions

Emulsions are dispersed systems of liquid droplets (dispersed phase) in a liquid (continuous phase) that are stabilized by electrostatic or steric effects. In most cases the stabilization is fulfilled by a surfactant. Several approaches were developed to form emulsions, such as micro-, macro- and miniemulsions.[36, 37] Another approach is the suspension polymerization. The emulsions types differ in the preparation method and in the size of the resulting dispersed droplets. The thermodynamical or kinetic stabilization is also different for the emulsion types. The emulsions are formed by an external contribution of energy into the system. This energy can be contributed by stirring, ultrasound or with a high pressure homogenizer.



Two emulsion types can be prepared, direct and indirect emulsions. Direct emulsions consist of an unpolar phase dispersed in a continuous polar phase, which is in most cases water. Indirect emulsions use unpolar phases as continuous phase in which the polar phase is dispersed.[38]

### 2.1.2 Stability of emulsions

For the stability of miniemulsions, two factors play an important role: Coalescence and Ostwald ripening.[39, 40]

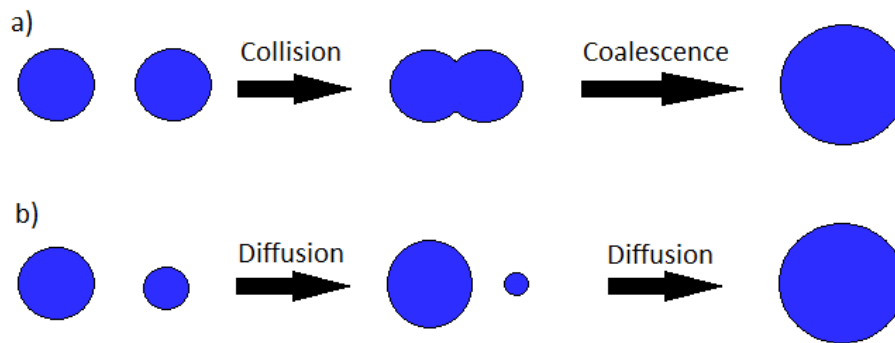


**Figure 2.1:** Both Coalescence (a) and Ostwald ripening (b) lead to droplets size increase.

The Ostwald ripening in emulsion describes the molecular diffusion degradation of droplets.[39] For an oil in water emulsion a polydispersity in the size of the formed droplets is always present. If the droplets are not stabilized against diffusion, smaller droplets will dissolve to form larger droplets. The reason for this is the difference in the Laplace pressure for different droplet sizes. The Laplace pressure  $p_{\text{Laplace}}$  is given by

$$p_{\text{Laplace}} = \frac{2\gamma_j}{R} \quad (2.1)$$

Here,  $\gamma_j$  is the interface energy between continuous phase and dispersed phase and  $R$  is the radius of the droplet.[38] As shown in equation 2.1, large droplets possess a lower Laplace pressure than small droplets. Therefore, diffusion of the droplet dispersed phase will occur from the small droplet to the large one and the small droplet will vanish to minimize the Laplace pressure. A necessary requirement for the diffusion is certain solubility of the dispersed phase in the continuous phase. The Ostwald ripening can be suppressed by using a very hydrophobic material, which is insoluble in the continuous phase. For direct miniemulsions, the so called ultrahydrophobe hexadecane is often used. The ultrahydrophobe leads to the formation of an osmotic pressure  $\Pi_{\text{osm}}$  in the droplet.

$$\Pi_{\text{osm}} = \frac{RT \cdot c}{M} \quad (2.2)$$

In this case  $R$  is the ideal gas constant,  $T$  the temperature,  $c$  the concentration and  $M$  the molar mass of the ultrahydrophobe. The osmotic pressure acts as counterbalance to the Laplace pressure, stabilizing the droplet against diffusion.

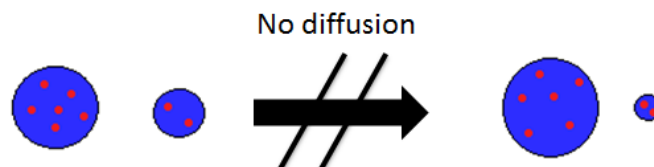


**Figure 2.2:** Suppression of Ostwald ripening by an ultrahydrophobe.

Coalescence means the collision of two or more droplets in an emulsion followed by a merging process.[39, 40] However, the collision of three or more droplets is very improbable. The droplets of the dispersed phase are not static due to Brownian motion and therefore always moving through the continuous phase. Without any stabilization the collision leads to a coalescence of the droplets. This can be prevented by the use of a surfactant, which protects the droplets with charge repulsion or steric hindrance from coalescence. A further possibility to stabilize the droplets is an increase in viscosity of the continuous phase.[41]

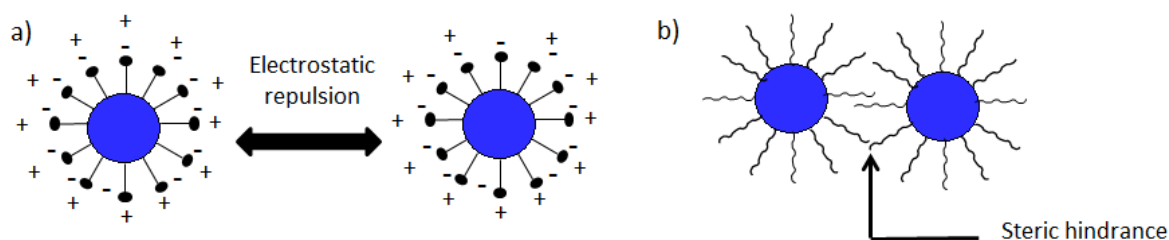


**Figure 2.3:** Stabilization of droplets by (a) electrostatic repulsion with ionic surfactants and (b) steric hindrance with nonionic surfactants.

### 2.1.3 Emulsion polymerization

The polymerization of the different emulsion types can form latex particles with different sizes. The surfactant concentration and the preparation method for the specific emulsions are the most important properties for the differences.

For a microemulsion, the surfactant concentration has to exceed a threshold, which is determined by the surfactant type and the temperature. For this concentration, the surface tension of the formed droplet oil/water surface is close to zero, which means that a thermodynamically stable emulsion is generated. Not all formed droplets are nucleated in the nucleation step of the polymerization. For that reason, the monomer of the non-nucleated droplets diffuses to the nucleated droplets and the latex particle diameter increases.[42, 43]

If the surfactant concentration is below the threshold value of a microemulsion and the surface tension is larger than zero, a kinetically stabilized macroemulsion is formed.[44] A macroemulsion consists of large monomer droplets stabilized by surfactant and empty or monomer swollen micelles in which oligoradicals can enter during the propagation step of the polymerization. The micelles containing polymer radicals are fed by monomer diffusing from the monomer droplets. Therefore, the micelles formed in the emulsification step are growing during the polymerization and latex particles larger than 100 nm are yielded. Unlike micro- and macroemulsions, no significant monomer transport occurs in a miniemulsion polymerization. The droplet size remains the same during the polymerization process.

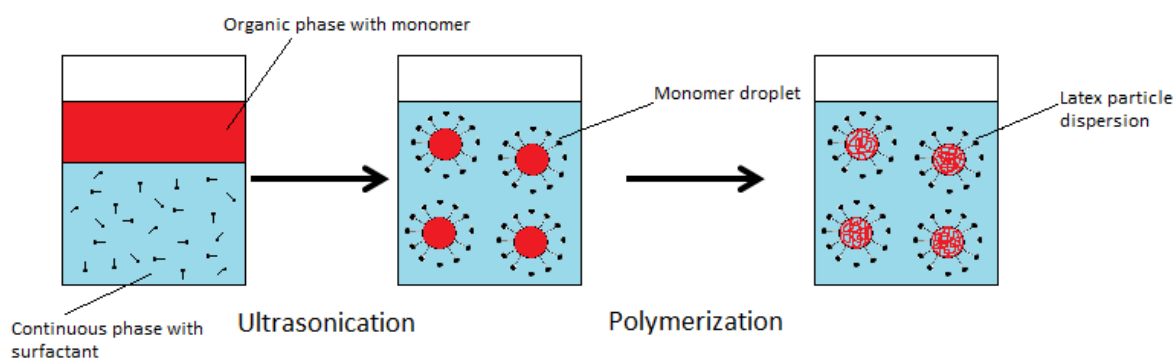


**Figure 2.4:** The synthesis of a nanoparticle dispersion with the miniemulsion technique.

With a low surfactant concentration the droplet surface is only partially covered with surfactant. Furthermore, the miniemulsion droplets have a small size from 30 nm to 500 nm. These small sizes can only be generated with high shear forces. It is possible to form miniemulsions with an ultraturrax, a high pressure homogenizer or with ultrasonication, for example. An ultrahydrophobe is used to prevent monomer diffusion. This results in each miniemulsion droplet acting as nanoreactor, where the size does not change during the polymerization.[45, 39]

## 2.2 Hybrid nanoparticles

The miniemulsion technique is practicable for the formation of polymer particles with several monomer compositions and polymerization methods.[46, 47] It is also possible to generate functional hybrid nanoparticles with this technique. A wide variety of applications is possible with the encapsulation of small molecules, solids and liquids into the polymer particle. The technical approach for the encapsulation of the different materials depends on their solubility in the monomer phase.

The encapsulation of materials that are soluble in the monomer phase, such as dyes [48, 49], organometal complexes [50], and organic molecules [51] can be performed easily with the miniemulsion process.[52] The material is added to monomer phase and homogeneously distributed in the formed droplets after the homogenization process. The final morphology of

the composite nanoparticle is determined by the solubility of the encapsulated compound in the polymer matrices. If the compound is soluble in the polymer, a nanoparticle is formed where the component is homogeneously distributed in the polymer. A material that is insoluble in the polymer leads to a phase separation between polymer and compound in the particle.

Compared to the encapsulation of soluble components the incorporation of materials that are insoluble in the dispersed phase, such as inorganic crystallites, amorphous nanostructures, organic pigments, and insoluble dyes is more challenging. The interfacial tension between, inorganic material, monomer or polymer, and the continuous phase of the miniemulsion turned out to be the main problem for the encapsulation of such structures. Inorganic structures possess a hydrophobic character and are therefore difficult to disperse in typical organic monomer phases. The surface of the components has to be hydrophobized by coating or surface modification before they can be used.

Insoluble materials that are more hydrophobic than the monomer, such as carbon-black particles and the pigment phthalocyanin blue can be dispersed in the monomer phase in a miniemulsion process.[53, 54] The hydrophobic materials can then be encapsulated in the polymerization step.[46]

When more hydrophilic components, such as titanium dioxide [55] or magnetite [56, 57], should be incorporated in hydrophobic polymers, the hydrophilic components need to become more hydrophobic. Without a further hydrophobization, the incorporation is very inefficient since the polymer cannot attach on the particles. This is achieved by a hydrophobization with organic carbon acids. For example, oleic acid for magnetite or stearic acid for calcium carbonate nanoparticles is used for the embedding in polystyrene particles.

Directly adding the hydrophobized inorganic nanoparticles to the monomer phase and performing a miniemulsion polymerization only results in nanocomposite particles with a small amount of the inorganic component with an inhomogeneous distribution of the inorganic nanoparticles in the polymer nanoparticles. The inorganic components form clusters due to strong interactions. A co-sonication must be used to embed the inorganic nanoparticles homogeneously in the droplet.[58, 59]

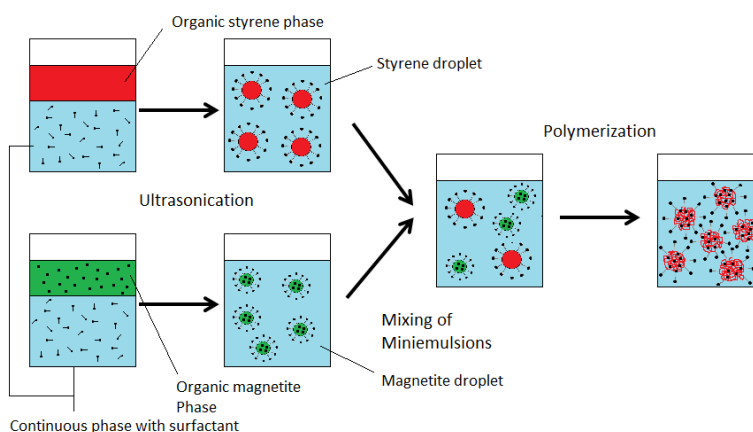


**Figure 2.5:** Synthesis of composite nanoparticles by a co-sonication illustrated for polystyrene magnetite nanoparticles.

The dispersions of hydrophobized material and monomer are generated separately, and then combined. After the polymerization, hybrid nanoparticles with inorganic contents of up to 40% can be obtained.[60]

For the encapsulation of liquids, broad range of different monomers can be used in various miniemulsion related techniques. The most important is the method of phase separation of liquid and polymer during the polymerization.[61, 62, 46, 52]

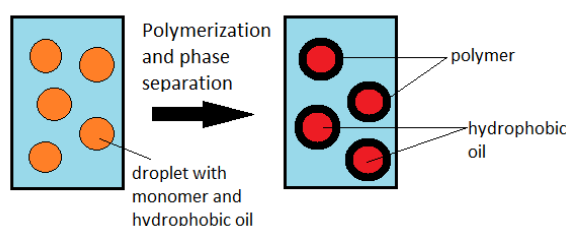


**Figure 2.6:** Phase separation method for nanocapsule synthesis.

With this technique, polymer nanocapsules can be obtained by a miniemulsion polymerization of a monomer droplet containing a high concentration of the ultrahydrophobe hexadecane, for example. Whereas monomer and oil are miscible in the miniemulsion, the polymer is insoluble in the oil and a phase separation occurs. A polymer shell encircling the more hydrophobic oil is formed during the polymerization.

The morphology of the nanocapsules can be influenced by the choice of the monomer or monomer mixture, because differences in the hydrophilicity of the polymer affect the capsule formation. A PMMA hexadecane miniemulsion system for example has a good tendency to form nanocapsules due to the higher hydrophilicity of PMMA compared to hexadecane, than a polystyrene hexadecane system. Polystyrene is more hydrophobic, therefore the addition of a suitable comonomer or an adjustment of the surfactant is necessary to allow a nanocapsule formation.[46]

## 2.3 Magnetism

### 2.3.1 Magnetic induction and magnetization

When an external magnetic field  $H$  is applied on a material, the response of the material is called magnetic induction  $B$ . [63, 64, 65] The relationship between magnetic induction and magnetic field is a material property and is called magnetization  $M$ .

$$\vec{B} = \mu_0 \cdot (\vec{H} + \vec{M}) \quad (2.3)$$

Here,  $\mu_0$  is the magnetic field constant. The magnetization is defined by the magnetic moment per volume unit.

$$M = \frac{d\mu}{dV} \quad (2.4)$$

### 2.3.2 Magnetic flux density

The magnetic flux density describes the flux  $\phi$  of the magnetic field lines in a material. The difference behavior of the magnetic flux density can be divided in three categories: [64]

- For  $\phi_{mat} < \phi_{outside}$ , the material is called diamagnetic. The material magnetizes itself in a way that the inner magnetic field of the material proportionally decreases with the strength of the applied external magnetic field. Since there is no magnetic dipole moment present in the material, it cannot respond to the magnetic field.
- If  $\phi_{mat} > \phi_{outside}$ , a paramagnetic material (Na or Al) is present. The material has magnetic dipole moments, which are arbitrary orientated in the material. An anti ferromagnetic material (FeO or MnO) can be also present, where the magnetic dipole moments are ordered in an anti-parallel fashion. The total magnetic moment of both material is therefore zero.
- If  $\phi_{mat} \gg \phi_{outside}$  is the case for a material, it is called ferro- or ferrimagnetic . In ferromagnetic materials, the magnetic dipole moments are oriented in the same spacial direction. The magnetic spins of ferrimagnets are coupled similar to anti ferromagnetic spins, but the spacial orientation one magnetic dipole moment is stronger . Therefore the magnetic moment is larger than zero.

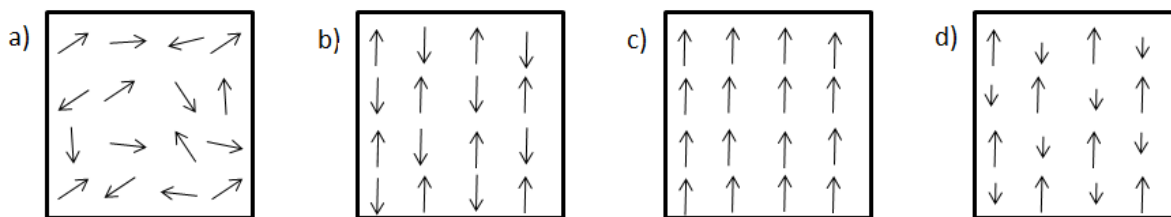


**Figure 2.7:** Magnetic dipole moment orientations for the different categories: (a) diamagnetism, (b) anti ferromagnetism, (c) ferromagnetism and (d) ferrimagnetism.

### 2.3.3 Susceptibility and permeability

The determination of magnetic properties cannot be taken out directly by the magnetization or the magnetic field, but by the change of these parameters in an applied field. This is called the magnetic susceptibility  $\chi$ .

$$\chi = \frac{M}{H} \quad (2.5)$$

The magnetic susceptibility indicates how strong a material reacts to the external magnetic field. The permeability  $\mu$

$$\mu = \frac{B}{H} \quad (2.6)$$

is a criterion for how permeable a material is for the external magnetic field.

The graphical depictions of  $M$  or  $B$  against the magnetic field  $H$  are called magnetization curves. For para-, antiferro- and diamagnetic materials, the magnetization increases linear with magnetic field and the magnetization is very low even for strong magnetic fields. Ferro- and ferrimagnetic materials show a very strong magnetization already for weak magnetic fields  $H$ . Also a saturation in the magnetization is visible. An increase of the magnetic field strength has only a small effect on the slope of the magnetization curve.

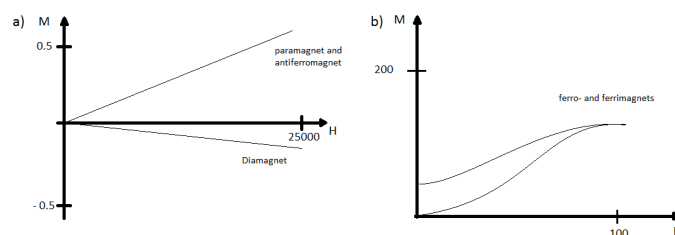


**Figure 2.8:** The schematic magnetization curves of (a) para-, antiferro- and diamagnets are linear with the applied field and show only a low magnetization for high fields. (b) The magnetization curves of ferro- and ferrimagnets show a high magnetization for low fields. The saturation of the magnetization is also visible.

If the applied magnetic field strength is decreased to zero after the saturation magnetization was reached, a rest magnetization of the material is still present. The magnetization cannot be reduced to zero by simply turning off the magnetic field. This phenomenon is called hysteresis. Hysteresis behavior can be observed for both polarities of the magnetic field and a hysteresis loop can be created by scanning the magnetization from the negative to the positive saturation field strength.

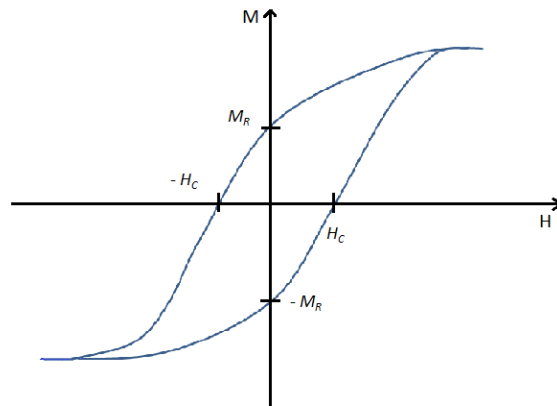


**Figure 2.9:** Schematic hysteresis loop of a ferromagnetic material.

The rest magnetization, called remanence  $M_R$  is still present when the magnetic field is turned off. The magnetic field has to be reverted in polarity to bring the rest magnetization to zero. The field strength necessary to force the magnetization to zero is called coercivity  $H_C$ . According to the value of the coercivity, ferromagnetic materials can be distinguished into hard and soft ferromagnets. Hard ferromagnets need a strong magnetic field to overcome the rest magnetization, whereas soft ferromagnets only need a weak field.

### 2.3.4 Magnetic and shape anisotropy

The magnetic properties of materials strongly depend on the spacial direction from which they are measured. For example, the value of the magnetic field of a cuboid ferromagnet differs on each side of the magnet. Magnitude and type of the magnetic anisotropy have an influence on the magnetization and hysteresis loops. The magnetic anisotropy of materials is an intrinsic value and depends on its crystal and macroscopic structure. Totally crystalline materials show a magnetization along the preferred crystallographic direction. Therefore the crystal structure of the material is of high importance for the choice of an appropriate material which fulfills the demanded requests. Since many materials are polycrystalline, a total crystalline anisotropy cannot be obtained. Only for perfect spherical materials, a regular magnetization in all directions is possible. If the material is not completely spherical, the magnetization occurs more easily along the direction of the longer axis than along the short axis of the material.



### 2.3.5 Magnetism of small particles

Crystalline ferro- (Fe, Ni, Co) and ferrimagnetic ( $\text{Fe}_3\text{O}_4$ ) substances are characterized by a coupling of their magnetic moments to a higher total moment below the Curie temperature. Due to the domain structure of the crystals, a hysteresis behavior is observed where all domains are oriented parallel to the external magnetic field. The amount of magnetic domains decreases with the decrease of the particle size. Magnetic nanoparticles possess only a single magnetic domain. A small one-domain nanoparticle ( $< 15$  nm) has a very high magnetic moment of several thousand  $\mu_B$ . Below the ordering temperature, the nanoparticles behave similar to a paramagnetic material, but with a huge magnetic moment. Therefore, they are called superparamagnets.

The magnetic anisotropy energy  $K \cdot V$  decreases with smaller particle volumes. At a diameter of 10 nm, the anisotropy energy is so low, that it is in the comparable range of the thermal energy  $K_B T$ . Therefore, the thermal energy can overcome the magnetic anisotropy energy and can easily change the magnetization of the particle from one to another direction. For this transformation, no external field is necessary.

Due to the competition of thermal energy and magnetic anisotropy energy, assemblies of several small particles are formed that show a magnetization behavior similar to a paramagnetic material, but with a much higher local magnetic moment than for a paramagnetic area. For that reason, the small particles already align in the same order at very small external magnetic fields. For an anisotropy value of zero, the magnetic moment can point in any direction and the particles show a paramagnetic behavior, which can be described using a derived Langevin function,

$$M = m \left( \coth(\alpha) - \frac{1}{\alpha} \right); \quad \alpha = \frac{mH}{K_B T} \quad (2.7)$$

with  $m$  as the magnetic moment per particle. For large  $m$  values,  $\alpha$  becomes also large. For that reason, the saturation magnetization can already be reached for small magnetic fields.

## 2.4 Magnetic alignment of nanoparticles and their complexing

When magnetic hybrid nanoparticles are directed through a ring magnet, the external magnetic field induces a magnetic dipole in each superparamagnetic nanoparticle and the particles align in a linear fashion driven by the dipole-dipole interactions. A strong magnetic field of several mT is necessary to guarantee a linear alignment of the nanoparticles along the magnetic field direction. Therefore, permanent ring magnets are used because they possess a strong linear magnetic field in their inner ring. Due to the attraction of the magnetic field of the ring magnet, the linear aligned nanoparticles overcome the electrostatic or steric repulsion of the surrounding surfactant and the inner-particle distance decreases drastically. The application of an external trigger such as a temperature above the glass transition stage  $T_g$  or the addition of a metal ion in the case of functionalized nanoparticles, locks the nanoparticles to linear assemblies.

Depending on which trigger was used, the assembly is reversible or irreversible. An increase of

the temperature above the  $T_g$  merges the nanoparticles irreversibly because the polymer chains of the nanoparticles can entangle.[14] The use of a metal complex as a locking functionality can be reversible. The application of an external trigger such as a change in the pH or a redox reaction [15] can destroy the complex and the locked nanoparticles can disassemble.

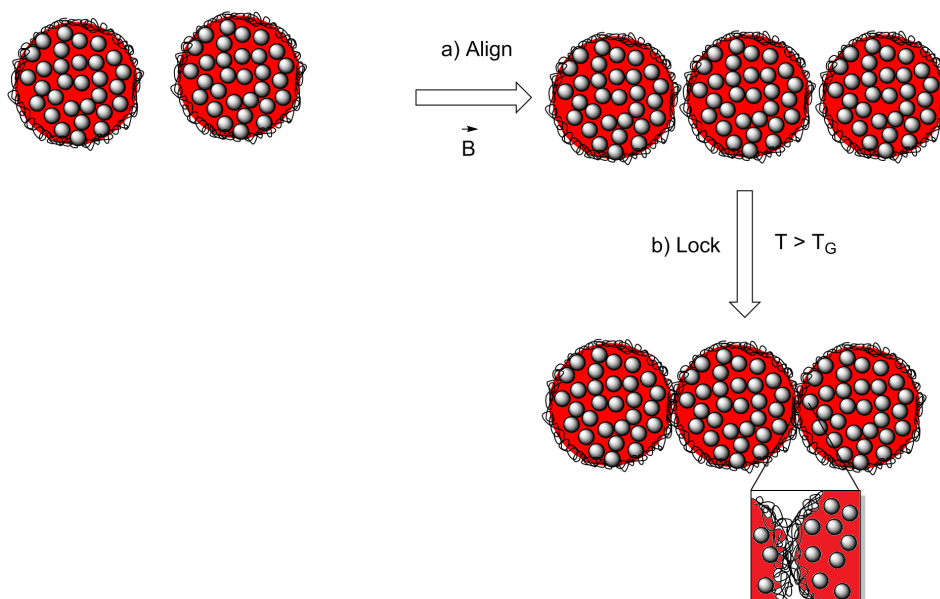


**Figure 2.10:** Schematics depicting the assembly of the nanoparticles. The linear alignment is achieved upon application of an external magnetic field (a). The temperature above the glass transition temperature locks the linear alignment by an entanglement of the polymer chains (b).

## 2.5 Self-Healing

As for many materials like steel and concrete, mechanical damages can occur in components made of polymers. In this case, cracks in the polymer components are problematic. These cracks can have a length of a few micrometers up to several centimeters, depending on the structure of the material. Small cracks can already damage the polymer component so severe, that a use of that component is not possible any more. A repair of the component is often expensive or sometimes impossible if the damage occurred inside the component.

A solution for this problem is the self-healing concept of polymer components. The damaged area can be cured by the application of of intrinsic or extrinsic self-healing agents. Intrinsic self-healing materials are in most cases polymer materials that have the ability to repair themselves after a damage occurred.[31, 32] Extrinsic self-healing material possess containers filled with the self-healing agent that are embedded in the polymer material. The encapsulated self-healing monomer is embedded together with a catalyst in the polymer component.[33]

If a crack in the material gets into contact with the capsule and destroys the shell, the self-healing agent can fill the crack and the catalyst which is in contact to the self-healing agent polymerizes the self-healing agent to cure the damage. For this self-healing system, the ring

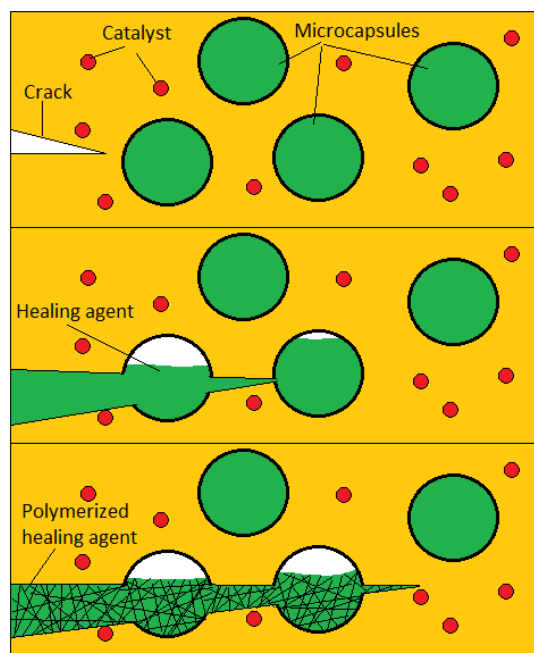


**Figure 2.11:** Schematic self-healing mechanism described by White et al. [33].

opening metathesis polymerization (ROMP) of dicyclopentadiene with a Grubbs catalyst is favored since the catalyst has a high activity and a good tolerance towards functional groups, oxygen, and water. Furthermore the living polymerization system provides a possibility of several healing steps.

The size and composition of the nanocapsules has to be adjusted to fulfill the desired requests of the polymer material for a possible application in a variety of components. Urea formaldehyde containers with a size of  $200\ \mu\text{m}$  were synthesized for thick polymer films, for example. With sonication techniques, the size of the urea formaldehyde capsules could be decreased to a size range between  $200\ \text{nm}$  and  $1.6\ \mu\text{m}$ , which allowed a possible use of the self-healing system for thin polymer films.[66]

The use of miniemulsion technique allowed an encapsulation of self-healing agents into small capsules of PLLA, and PMMA.[67] This expands the possible application fields of the self-healing nanocapsules. For example, a PLLA capsule already degrades when it gets into contact with water and releases the self-healing agent. This is beneficial to avoid moisture damage in the polymer components. In opposite to this easy degradable systems, capsules with a silica shell were prepared to obtain a high stability towards temperature and external influences.[67, 68] All these advantages improve the durability of fragile and cost intensive polymer components and a possible transition of the self-healing concept of polymer materials to brittle materials like glassware and ceramics is quite high.

## 3 Results and Discussion

### 3.1 Oleate capped $\text{Fe}_3\text{O}_4$ nanoparticles

The synthesis of the oleate capped  $\text{Fe}_3\text{O}_4$  nanoparticles yielded 15.8 g (88% of the theoretical value) of a black sticky solid, which showed a strong magnetic behavior.

The X-ray crystallography spectrum shows reflexes which refer to the spectra of magnetite.

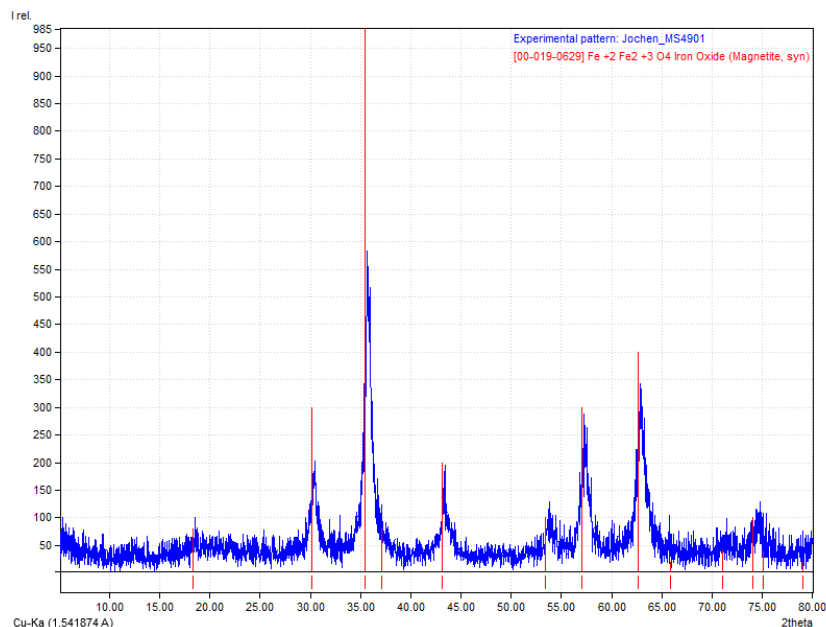


**Figure 3.1:** The XRD spectrum of oleate capped magnetite nanoparticles matches with the reflexes of bulk magnetite.

The diffractogram displayed in Figure 3.1 shows broad reflexes for the oleate capped  $\text{Fe}_3\text{O}_4$  nanoparticles. The broadness of the reflexes refers to the capping with oleic acid. The XRD patterns could be ascribed to magnetite (JCPDS File No. 19-0629).

The TEM images show a size distribution from 6 nm to 20 nm (compare Figure 3.2).

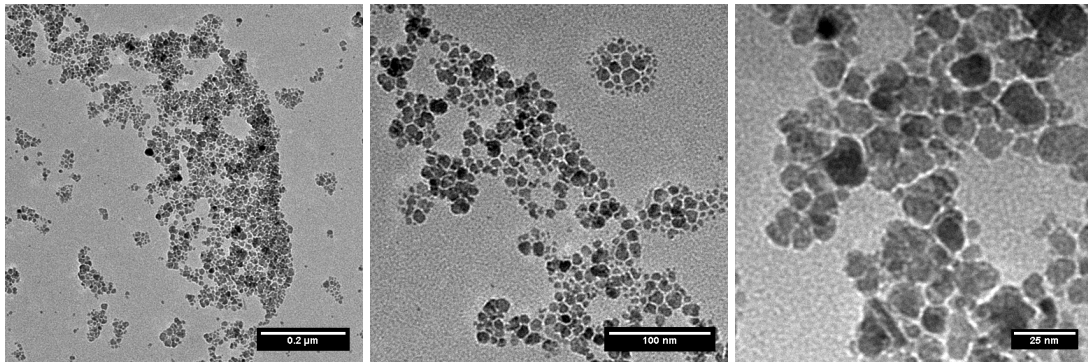


**Figure 3.2:** TEM micrographs of oleate capped magnetite nanoparticles.

As visible in the micrographs, the nanoparticle shape is not round, but has several corners which result in an octagonal, hexagonal, or even cubic like shape. Notches and edges are also visible. The mean diameter of the  $\text{Fe}_3\text{O}_4$  nanoparticles was determined to be 8 nm by TEM. The thermogravimetric analysis shows a decrease in the nanoparticle mass of 32.4% in total, which refers to the decomposition of oleic acid (compare Figure 3.3).

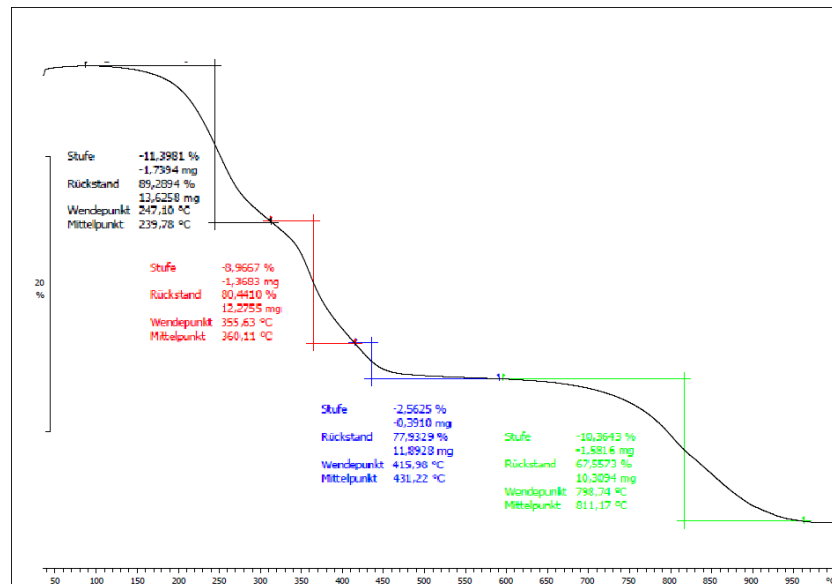


**Figure 3.3:** Thermogravimetric analysis of oleate capped  $\text{Fe}_3\text{O}_4$  nanoparticles.

The thermogravimetric analysis displays that 67.6% of a nanoparticle consists of  $\text{Fe}_3\text{O}_4$ . Since the melting point of magnetite is 1538 °C [69] it can be concluded that only the oleic acid decomposed during the heating process.

The saturation magnetization of the oleate capped nanoparticles was determined with a vibrating sample magnetometer (VSM) measurement to be at  $56.83 \text{ emu} \cdot \text{g}^{-1}$ .

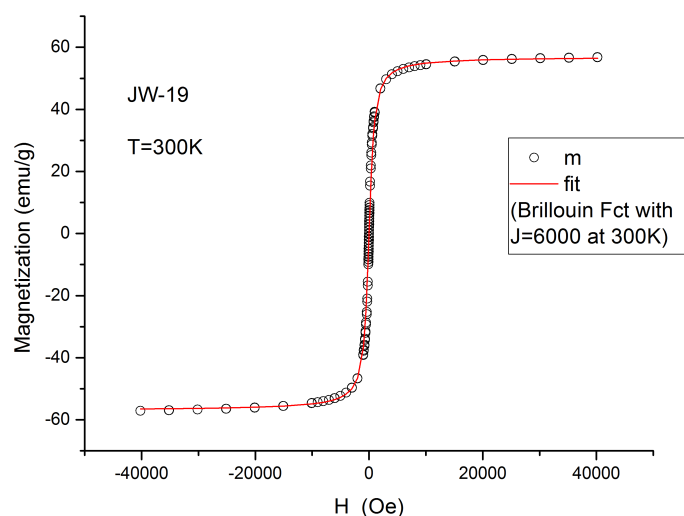


**Figure 3.4:** VSM magnetization curve of oleate capped  $\text{Fe}_3\text{O}_4$  nanoparticles.

The magnetization curve of the oleate capped magnetite nanoparticles shows no hysteresis. The lack of a hysteresis is a typical property of superparamagnetic nanoparticles [70, 65]. Compared to the saturation magnetization value of bulk magnetite, which is  $92 \text{ emu} \cdot \text{g}^{-1}$  [70], the saturation magnetization of the oleate capped nanoparticles is rather low. If the mass percentage of the oleic acid is subtracted from the magnetization, a saturation value of  $83.6 \text{ emu} \cdot \text{g}^{-1}$  can be obtained, which is close to the bulk saturation magnetization. This is suitable for the needed purpose of the linear magnetic alignment of nanoparticles.

## 3.2 Magnetic Spherical Colloidal Building Blocks

### 3.2.1 Synthesis of the magnetite containing polystyrene nanoparticles

For the synthesized dispersions with different amount of *n*-octane and different sonication amplitudes the mean diameters were determined with DLS. The results summarized in Table 2 show, that the amount of *n*-octane as well as the sonication times used have an effect on the mean diameter of the dispersion.

**Table 2:** Mean diameters of different magnetic polystyrene nanoparticles for the different *n*-octane amounts and sonication amplitudes.

Sample	$m_{n\text{-octane}}$	Amplitude / %	$d_H / \text{nm}$	$\sigma / \text{nm}$
JW-04	0.6	70	147	61
JW-05	7.5	70	206	74
JW-09	10.0	30	232	76
JW-10	10.0	30	193	73

An increasing amount of *n*-octane increases the particle diameter. Comparing JW-09 and JW-10, the influence of the sonication time is also visible. A longer sonication time results in a decrease in the mean particle diameter at the same *n*-octane concentration and amplitude.

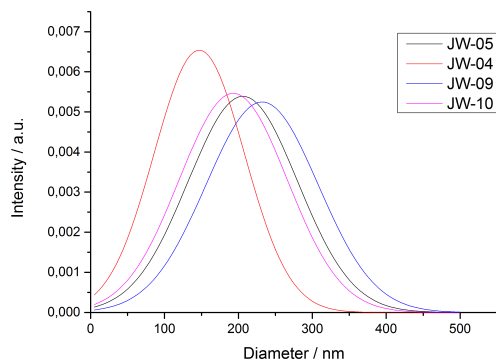


**Figure 3.5:** DLS Gaussian distribution curves of the four different nanoparticle dispersions.

The standard deviation of the nanoparticle dispersions is more or less unaffected by the amount of *n*-octane and sonication amplitudes (Figure 3.5). The polydispersity of the four hybrid nanoparticle dispersions is a result of the co-sonication miniemulsion process. The effects of the variation of the *n*-octane concentration and sonication amplitudes are visible in the TEM micrographs (compare Figure 3.6, Figure 3.7, Figure 3.8 and Figure 3.9).

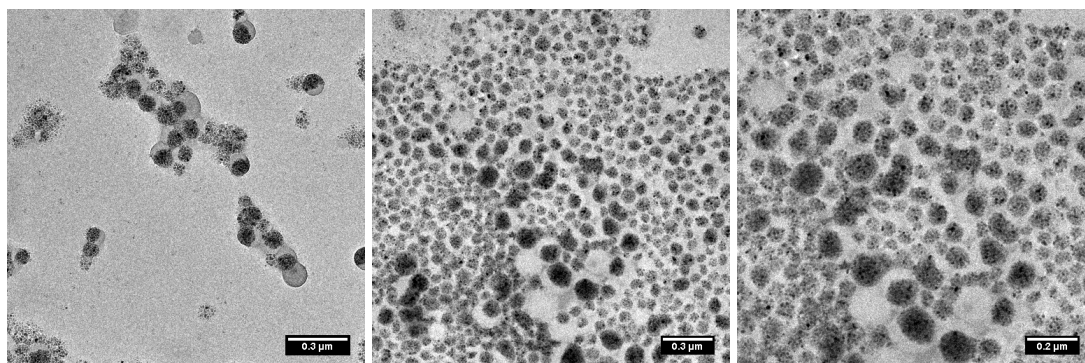


**Figure 3.6:** TEM micrographs of JW-04 with a low *n*-octane content.

A low *n*-octane concentration and high sonication amplitudes as it is the case for JW-04 results in an inhomogeneous magnetite distribution inside the nanoparticles (see Figure 3.6). A partial phase separation of magnetite and polystyrene in the nanoparticles with only one side of magnetite inside is visible as well as nanoparticles only containing polystyrene. Several nanoparticles show only a little amount of magnetite, while others are highly loaded. Due to

the inhomogeneity of the nanoparticles, this dispersion is not useful for the chain formation investigations and was not further used.

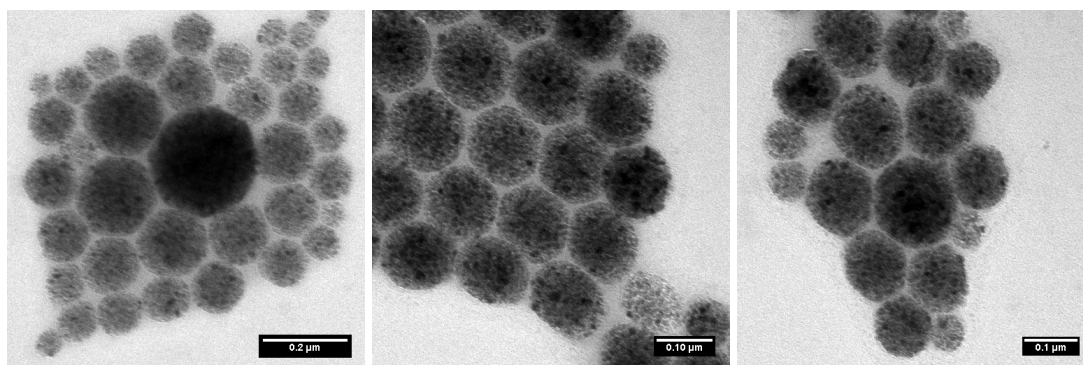


**Figure 3.7:** TEM micrographs of JW-05 with a higher *n*-octane content.

Nanoparticles synthesized using a higher *n*-octane concentration and equal sonication amplitude, show a homogeneous magnetite distribution (see Figure 3.7). No phase separated nanoparticles where one side of the nanoparticle possesses magnetite inside are visible and the magnetite is well distributed inside the nanoparticles. Therefore, this nanoparticle dispersion was used for further investigations and was size-separated by centrifugation. The  $\zeta$ -potential of the sample JW-05 was determined as  $\zeta = -91.6 \text{ mV} \pm 10.1 \text{ mV}$  at neutral pH.

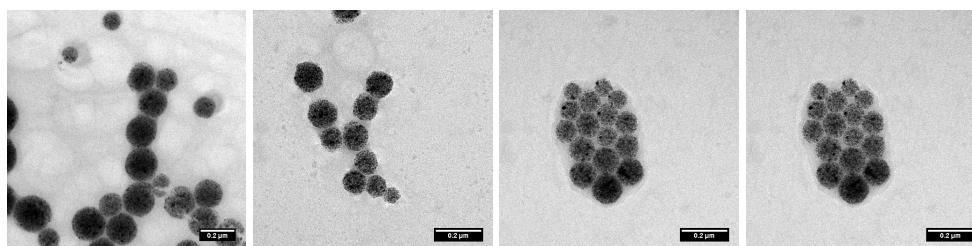


**Figure 3.8:** TEM micrographs of JW-09.

A further increase of the *n*-octane concentration and a low sonication amplitude result in a magnetite distribution for nanoparticles of JW-09 which is as homogeneous as for JW-05 (compare Figure 3.8). Furthermore, the magnetite loading is higher than in JW-05. For that reason, this dispersion was used to investigate the conditions for the chain merging process.



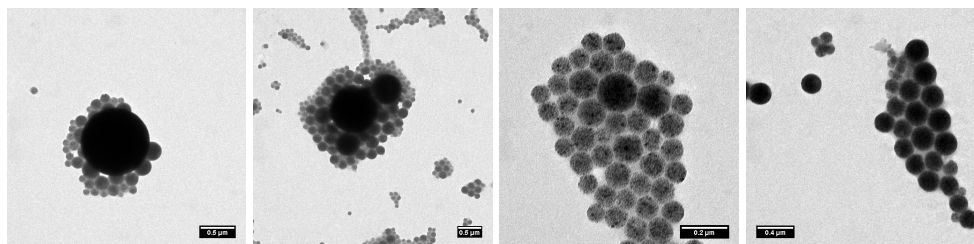


**Figure 3.9:** TEM micrographs of JW-10.

The micrographs of the JW-10 dispersion show similar nanoparticles as JW-09 (see Figure 3.9). Larger nanoparticles of diameters above 500 nm are present in this dispersion. This is caused by the low sonication amplitude. Therefore, they were also size separated by centrifugation for further investigation.

In conclusion, it can be stated that the amount of *n*-octane affects the magnetite distribution in the nanoparticle dispersions. For a homogeneous magnetite loading of the nanoparticles, a larger amount of *n*-octane is necessary. A low amount of *n*-octane results in inhomogeneous nanoparticles. The incorporation of magnetite nanoparticles in polystyrene nanoparticles is more efficient for higher *n*-octane concentrations. The  $\text{Fe}_3\text{O}_4$  nanoparticle droplets are better hydrophobized and incorporated more easily in the styrene droplets during the miniemulsion polymerization. With a higher amount of *n*-octane the oleate capped magnetite nanoparticles have a larger volume in which they can re-disperse. This avoids the formation of large aggregates of magnetite nanoparticles. Since smaller nanoparticles have a higher chance to be incorporated into the styrene droplets, the samples JW-05, JW-09 and JW-10 with a higher amount of *n*-octane display a higher incorporation rate for magnetite nanoparticles. Additionally, the sonication amplitude has a certain effect on the particle size. For lower sonication amplitudes, larger nanoparticles are formed in the sample than for higher amplitudes. The lower shear rate increases the amount of larger droplets during the miniemulsion process and the larger droplets form larger nanoparticles.

The thermogravimetric analysis of JW-09 shows a decrease of the mass by 23.9% until 300 °C. The decrease is related to the decomposition of the surfactant SDS and oleic acid. The second step, which results in a loss of mass by 16% is related to the decomposition of the copolymer. The total mass decrease is 39.2%. According to the TGA of the oleate capped nanoparticles, 60.8% of the JW-09 nanoparticles consist out of magnetite, which agrees with the expectations related to the TEM micrographs. A high amount of magnetite in the nanoparticles leads to a large magnetic dipole moment of the nanoparticle when an external magnetic field is applied. For that reason, it is more easy for the nanoparticle dipoles to interact with each other.

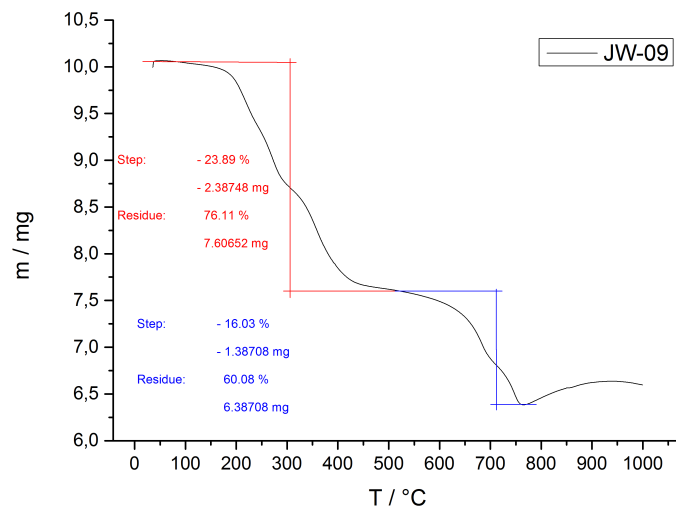


**Figure 3.10:** Thermograph of the JW-09 nanoparticles.

### 3.2.2 Size-separation of the magnetite containing polystyrene nanoparticles

For the planned investigation of the size dependent assembly behavior of the synthesized magnetic polystyrene nanoparticles, the samples JW-05 and JW-10 were size separated with a centrifuge at different revolutions per min and examined with DLS and TEM.

**JW-05 examination** Several TEM micrographs were recorded for each of the separated sediments. The following micrographs show the results of the centrifugations at different rpm (see Figure 3.11).

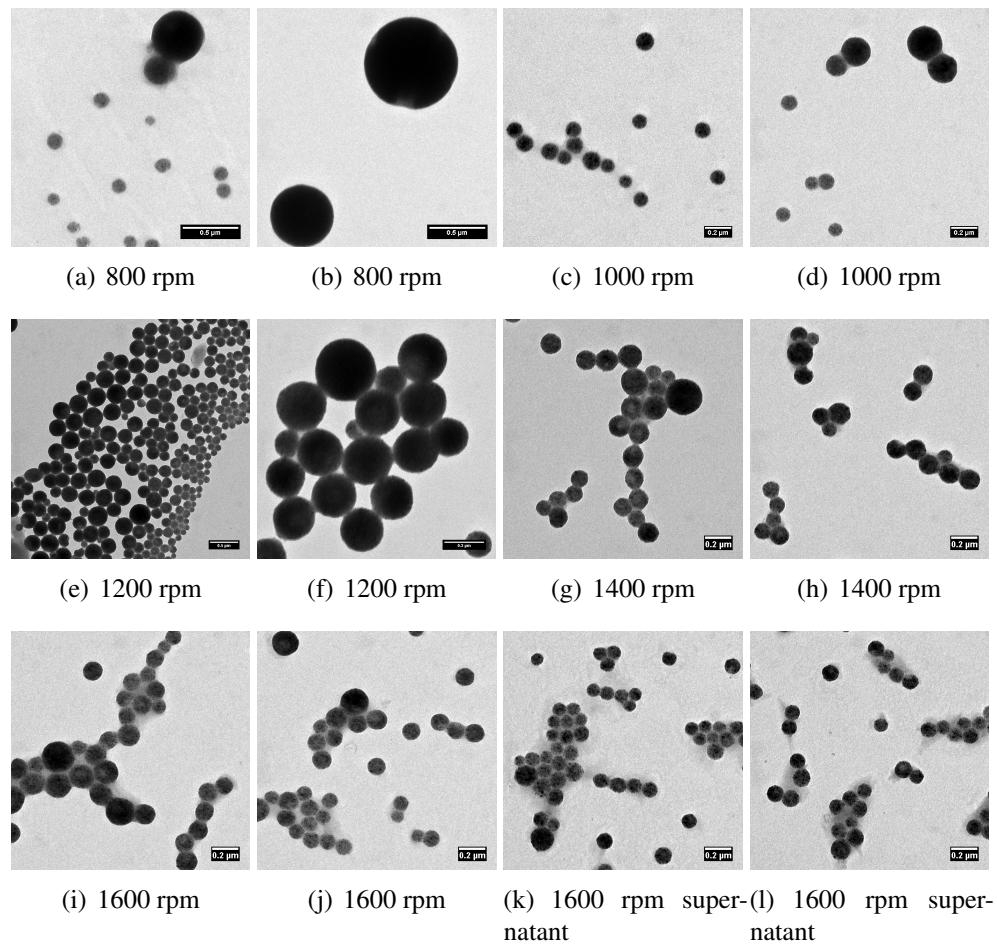


**Figure 3.11:** TEM micrographs of the size separated magnetic nanoparticle samples achieved by the size separation of the JW-05 dispersion with a centrifuge at different revolutions per min.

The TEM micrographs of the centrifuged nanoparticles show that the centrifugation did not yield a particle dispersion with an uniform size distribution. Whereas the initial sample has a broad distribution, the first centrifuged sample with 800 rpm displays very large nanoparticles with diameters of  $\approx 500$  nm and nanoparticles with a size less than 200 nm. The average TEM diameters of the sedimented nanoparticle dispersions are decreasing for higher centrifugation forces. The dispersion of the sedimented nanoparticles of the 1200 rpm sample has a low bimodal distribution with a mean diameter of around 300 nm and does not fit in the decreasing trend.

To determine this trend, the TEM diameters of 100 particles per sample were measured using the GWYDDION software and the resulting average diameter was compared with the DLS mean diameters of the same centrifuged sample.

**Table 3:** Average diameters of the centrifuged nanoparticles of JW-05.

$\text{rpm}_{\text{centrifuge}}$	$D_h$ (nm)	$\sigma_{DLS}$ (%)	$D_{TEM}$ (nm)	$\sigma_{TEM}$ (%)
0	125	30	128	27
800	138	47	259	119
1000	136	32	159	44
1200	354	9	226	31
1400	225	16	177	29
1600	162	25	149	21
1600 Supernatant	155	13	112	15

A size separation of the polydisperse dispersion was attempted by removing certain nanoparticle sizes. Starting with the largest nanoparticles at a low centrifugation force smaller nanoparticles were subsequently separated off with an increasing centrifugation force. The supernatant of the 1600 rpm centrifugation should contain the smallest nanoparticles of the initial dispersion. Table 3 displays that this was not achieved completely. The sedimented nanoparticle dispersions show only a slight decrease in size with increasing centrifugation force. The chosen steps for the increase of the revolutions per min were not large enough to sediment a clear size range of nanoparticles. Therefore, the centrifugation steps sedimented a nanoparticle size distribution which overlapped with the centrifugation before and ensuing. This resulted in only a small decrease in the mean diameter of the different sedimented nanoparticles for the centrifugations. A comparison of the determined average TEM diameters with the DLS mean diameters for every sample shows that no relationship between the diameters is present. The diameters of DLS and TEM do not match as well as the standard deviations. The average diameters determined with TEM should be smaller than the hydrodynamic diameters, since the velocity of the nanoparticle with its surfactant layer is measured with DLS. The average diameters of the nanoparticles were determined without this layer. The hydrodynamic diameter is decreasing when the standard deviation increases. A broad distribution curve results in a decrease in the mean diameter, because more nanoparticles of a smaller diameter are present

and the curve is shifted to smaller mean diameters. This is not the case for the average diameters determined with TEM.

**JW-10 examination** The magnetic polystyrene nanoparticles of JW-10 were size-separated and the separated and re-dispersed sedimented nanoparticles were examined with TEM and DLS. The following micrographs in Figure 3.12 show the TEM results of the centrifuged samples.

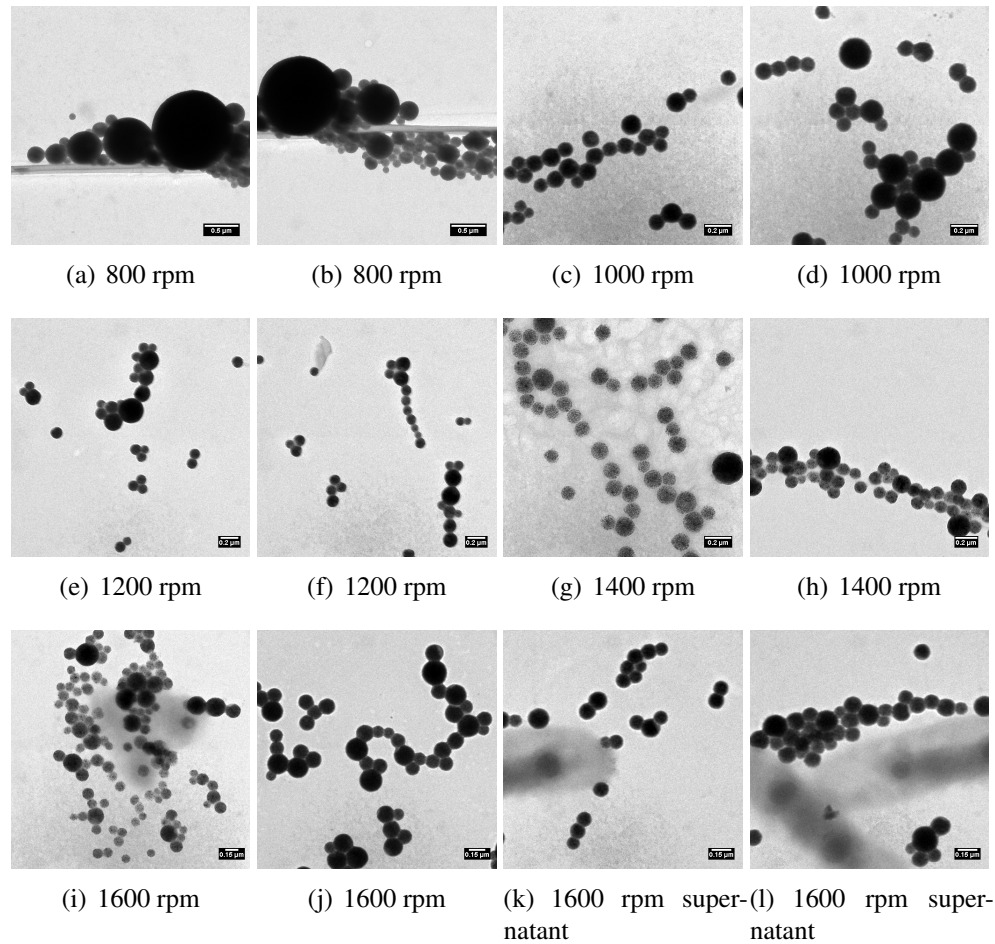


**Figure 3.12:** TEM micrographs of the size separated magnetic nanoparticle samples achieved by the size separation of the JW-10 dispersion with a centrifuge at different revolutions per min.

The micrographs show a similar result as for the JW-05 samples. The first centrifuged sample contains large nanoparticles with diameters above 500 nm. Low centrifugal forces remove large nanoparticles of higher densities from the dispersion because the centrifugal force pushes them to the ground. A stepwise increase of the centrifugal forces removes the next smaller

nanoparticle sizes. This is the case for the TEM average diameters in Table 4. Except the sample centrifuged at 1200 rpm, the TEM average diameters show a decreasing trend. Compared to this, the DLS mean diameters of the centrifuged samples show no decrease for increasing centrifugal forces.

**Table 4:** Average diameters of the centrifuged nanoparticles of JW-10.

$\text{rpm}_{\text{centrifuge}}$	$D_h$ (nm)	$\sigma_{DLS}(\%)$	$D_{TEM}$ (nm)	$\sigma_{TEM}(\%)$
0	193	38	-	-
800	174	24	198	121
1000	221	15	171	26
1200	194	19	226	31
1400	214	12	136	26
1600	176	23	123	16
1600 Supernatant	149	19	116	18

In comparison to the size separations of JW-05, the centrifuged samples of JW-10 show a larger mean diameter in DLS for the first two centrifugations, and are approaching similar mean diameters with increasing revolutions per min. As mentioned before, the sample of JW-05 at 1200 rpm does not follow any trend for the centrifugation. The fact that an excellent size separation as for JW-05 1200 rpm could not be achieved in all other samples, is caused by the difficulty of complete supernatant removal. The incomplete removal of the supernatant results in up to 30% of smaller nanoparticles that are visible in the TEM micrographs. These small nanoparticles are still dispersed and do not belong to the fraction of the sedimented ones. This results in an increase of the standard deviation and an simultaneous decrease in the average diameter.

A summary of the comparison of both, the TEM and DLS data for both experiments can be found in Figure 3.13 and Figure 3.14.

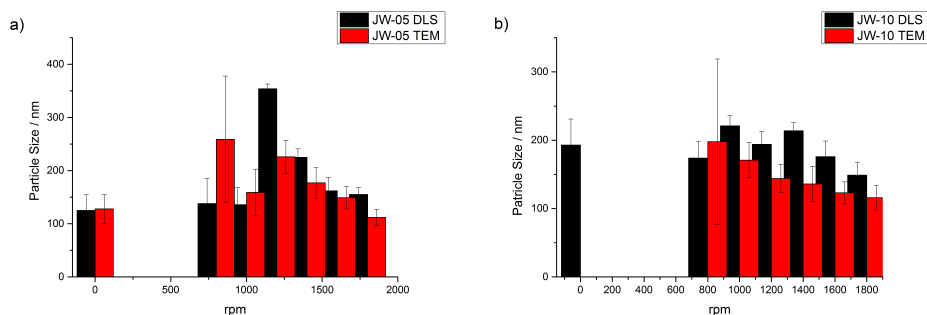


**Figure 3.13:** Pillar diagrams comparing DLS and TEM Diameters of the size separation of JW-05 (a) and JW-10 (b).

The pillar diagrams in Figure 3.13 visualize the difference between the mean diameters of DLS and TEM experiments. Another important aspect when comparing TEM with DLS data is the missing connection between hydrodynamic (DLS) and geometrical diameters (TEM). The assumption that the DLS values of the mean diameters are always larger than the ones of the TEM measurement can only be stated for higher centrifugation forces. For lower centrifugation forces, the TEM mean diameter is larger.

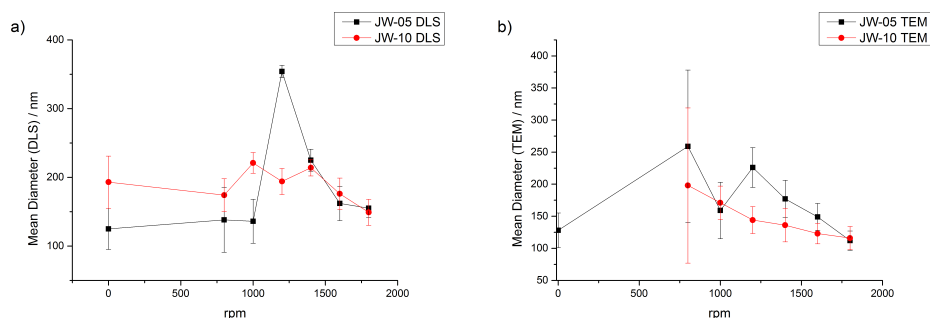


**Figure 3.14:** Direct comparison of DLS (a) and TEM (b) Diameters and standard deviation of JW-05 and JW-10.

The line diagrams in Figure 3.14 compare the DLS and TEM values of the measured samples. The DLS values of the first three centrifugations differ large in their mean diameters, with the JW-10 sample having a larger diameter than JW-05. Arriving at 1400 revolutions per min, the mean diameters are approaching towards each other, reaching almost similar size at 1600 rpm. For the TEM examination, the samples of JW-05 display the larger diameters, only come to a minimum at 1000 rpm. The mean diameter values of both samples again approach with higher centrifugation forces.

**Summary:** A size-separation of nanoparticles with a centrifuge is possible only to a certain degree. No clear size separated nanoparticle fractions were obtained but it was possible to separate broad size fractions, with very large and very small nanoparticles. With these nanoparticle fractions the merging behavior of different nanoparticle sizes can be investigated using larger or smaller fractions of nanoparticles or combining the largest with the smallest nanoparticles.

### 3.2.3 Attempts on creating nanochains with magnetic polystyrene nanoparticles

To examine which flow rate of the syringe pump is the best choice to create as long nanochains as possible, 2.5 ml of a previously purified dispersion of JW-09 was pushed through a capillary using different flow rates. The DLS results listed in Table 5 depict, that almost no change in the mean diameter occurred during the chain merging process.

**Table 5:** Mean diameters of formed chains at different flow rates.

Flow rate / ml/h	Mean diameter / nm	Standard deviation / nm
0	232	76
25	207	70
30	210	71
35	210	61

Compared to the mean diameter of the initial dispersion of JW-09, the mean diameters of the nanochain dispersions are also decreasing when higher force is applied. This behavior is visible when comparing the Gaussian distribution curves of the nanochain mean diameters in Figure 3.15.



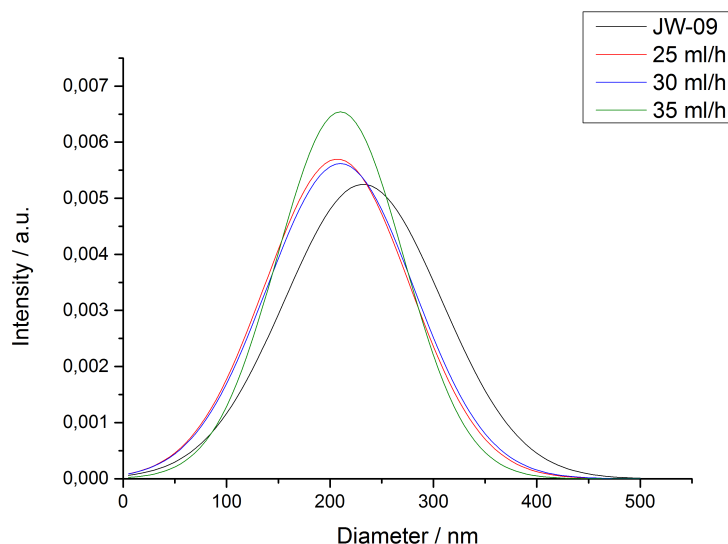


**Figure 3.15:** The Gaussian distribution curves plotted from the DLS mean diameters of the nanochain mean dispersions.

As displayed in the TEM micrographs, some shorter chains were synthesized in each of the samples.

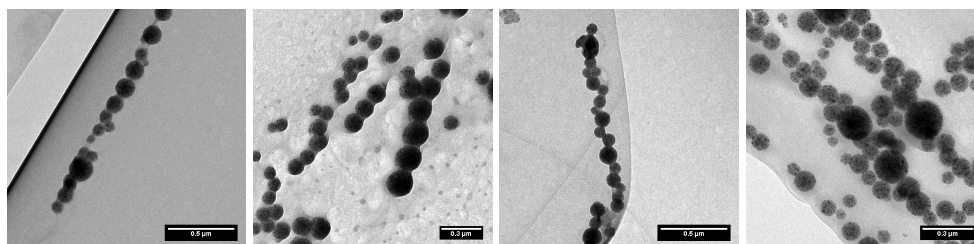


**Figure 3.16:** TEM micrographs of nanochains merged with a 25 ml/h flow rate.

The TEM micrographs of the 25 ml/h flow rate dispersion display several nanochains formed during the merging process. The chain lengths are between 0.5 and 2.0  $\mu\text{m}$ . It is visible that the nanoparticles of these chains are irreversibly merged together, as it was demonstrated before by Bannwarth et al. [14]. Despite obtaining nanochains with a length of more than ten nanoparticles, there are still many single nanoparticles visible in the images. The presence of nanoparticles that did not form linear assemblies displays that the entanglement of the polymer chains during the merging process is not efficient. The nanoparticles align in the magnetic field but only a small amount of them merges with the neighboring ones.

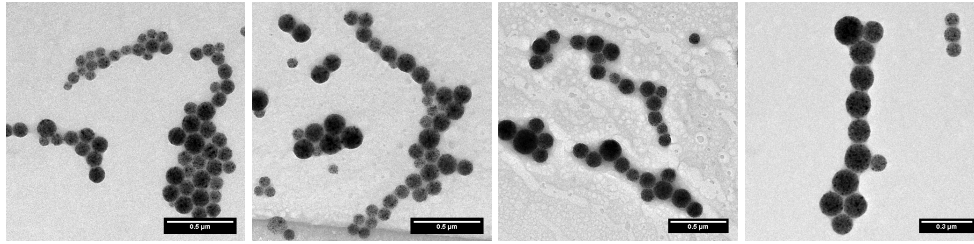


**Figure 3.17:** TEM micrographs of nanochains merged with a 30 ml/h flow rate.

A similar result at 30 ml/h flow speed for the nanochain formation is shown in the micrographs in Figure 3.17. There are several shorter chains visible surrounded by single nanoparticles.

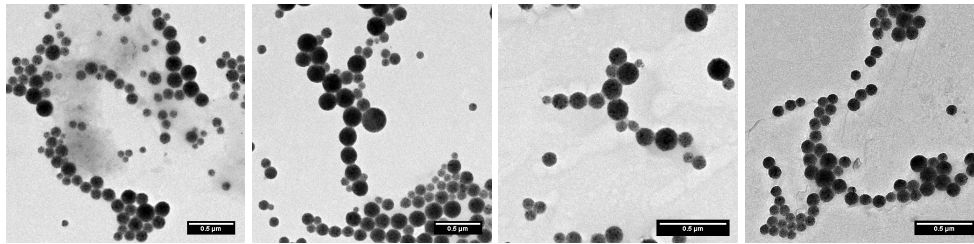


**Figure 3.18:** TEM micrographs of nanochains merged with a 35 ml/h flow rate.

The experiment conducted with a flow rate of 35 ml/h proves the outcome of the two prior ones (compare Figure 3.18). No longer nanochains were achieved with higher flow rates. With all three flow speed assessments showing the same results, yielding nanochains of a chain length, which is far below the results reported by Bannwarth et al. [14], it is hard to investigate the merging behavior of magnetic nanoparticles of different sizes. The nanochains do not have the necessary length to determine which nanoparticle size is incorporated preferentially and which nanoparticle prefers neighbors of a certain size.

### 3.2.4 Conclusion

The size separation of these nanoparticles was successful and resulted in a set of nanoparticles with narrow size distributions. The attempt to merge the synthesized magnetic polystyrene nanoparticles into chains was also successful, although the chains were rather short. Since the synthesized nanoparticles showed no high merging degree, the size separated nanoparticles were not used for further investigations.

In total, the synthesized nanochains did not possess the necessary length to proceed with the experiment of the merging behavior. The poor entanglement of the nanoparticle polymer chains during the merging process made it difficult to determine the rate of fitting for nanoparticles with different size. As no statistical representative chain lengths were obtained, the project was no longer pursued.

### 3.3 pH-triggered assembly/disassembly of magnetic polystyrene nanoparticles

The pH-triggered assembly/disassembly of magnetic polystyrene nanoparticles is fulfilled by the functionalization of the magnetic nanoparticles with the complexing group *N*-methyl-diaminoethyl that is able to complex transition metals. For the investigation of the system copper(II) was used. The disassembly should take place by the addition of hydrochloric acid to the nanochain dispersion.

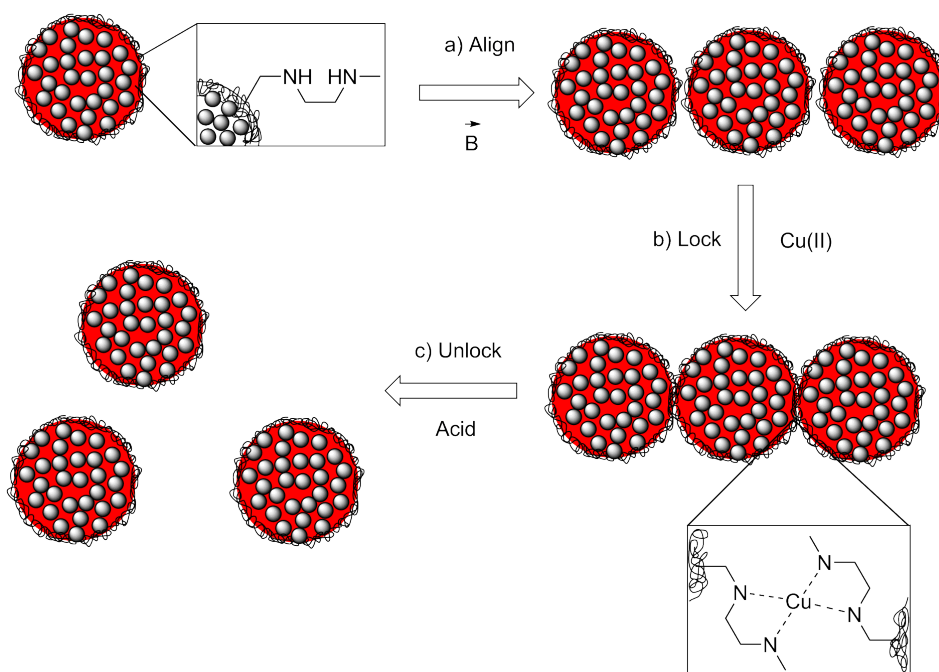


**Figure 3.19:** Schematics depicting the assembly/disassembly of the nanoparticles. The linear alignment is achieved upon application of an external magnetic field (a). The following copper complexing locks the linear alignment (b). The addition of acid protonates the amino functionalities and releases the particles (c).

#### 3.3.1 Synthesis of *N*-methyl-diaminoethyl functionalized magnetic nanoparticles

*N*-methyl-diaminoethyl functionalized nanoparticles with a mean diameter of 210 nm and a standard deviation of 52% were synthesized. The  $\zeta$ -potential was determined to be  $\zeta = -62.6 \text{ mV} \pm 26.0 \text{ mV}$ . The thermogravimetric analysis shows three steps in the nanoparticle decomposition.

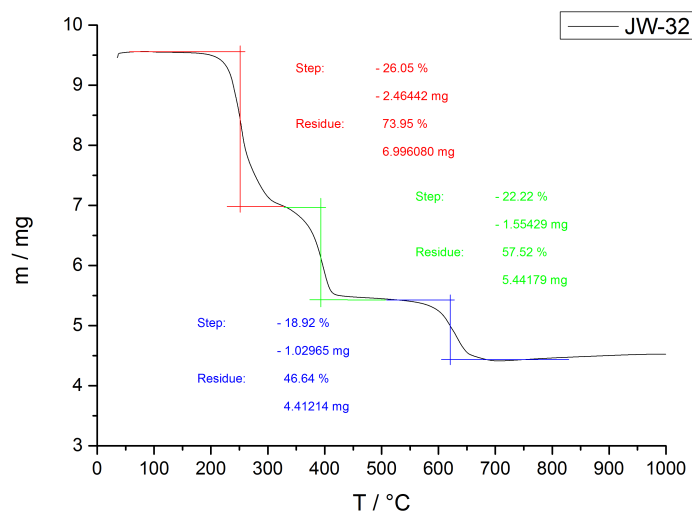


**Figure 3.20:** Thermograph of *N*-methyl diaminoethyl functionalized magnetic nanoparticles.

For the first step a loss in mass of 26.1% is recorded. The loss of is similar to the standard nanoparticles, where 23.9% of the weight was lost in the first step. It can be attributed to decomposition of SDS. The second step records a loss of 22.2% and is ascribed to the decomposition of oleic acid and the diaminoethyl functional group. The last step 18.9% is the final decomposition of polystyrene. In total, 46.6% of the *N*-methyl diaminoethyl functionalized nanoparticles can be imputed to magnetite. This is almost 15% less than for the standard particles. The decrease of the magnetite amount incorporated in the nanoparticles can be imputed to the higher surfactant concentration used for the stabilization of the nanoparticles compared to the standard ones. A 1 wt.% solution of SDS was always necessary to stabilize the nanoparticles for a longer time, whereas a 0.1% SDS solution was used for the standard nanoparticles. The TEM micrographs show 5-10% large nanoparticles up to 500 nm surrounded by many small particles of sizes between 30 nm and 80 nm (see Figure 3.21).

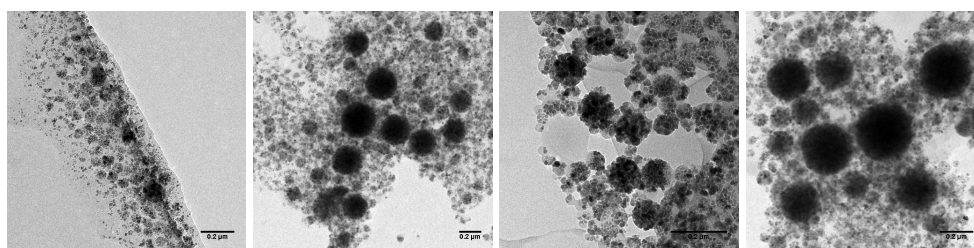


**Figure 3.21:** The TEM micrographs show a broad size distribution of *N*-methyl diaminoethyl-functionalized magnetic nanoparticles favoring small nanoparticles before centrifugation.

To improve this broad size distribution towards a narrow range of nanoparticle sizes, several centrifugations were carried out with different revolutions per min for 10 min. The supernatant was collected and centrifuged with higher revolutions per min. The sedimented nanoparticles

were redispersed in a 1 wt.% SDS solution and the size of the particles were determined by DLS and TEM.

**Table 6:** DLS data of diaminoethyl-functionalized magnetic nanoparticle centrifugation.

$\text{rpm}_{\text{centrifuge}}$	Mean diameter / nm	Std Dev. (%)
500	600	62
500 Supernatant	190	52
1000	329	40
1000 Supernatant	177	55

The first centrifugation enabled the large particles to separate from the very small ones, which can be stated by DLS as well as in TEM micrographs. While the sediment of the 500 rpm centrifugation shows a large nanoparticle size distribution in both DLS and TEM, the supernatant only shows nanoparticles of a diameter smaller than 300 nm.

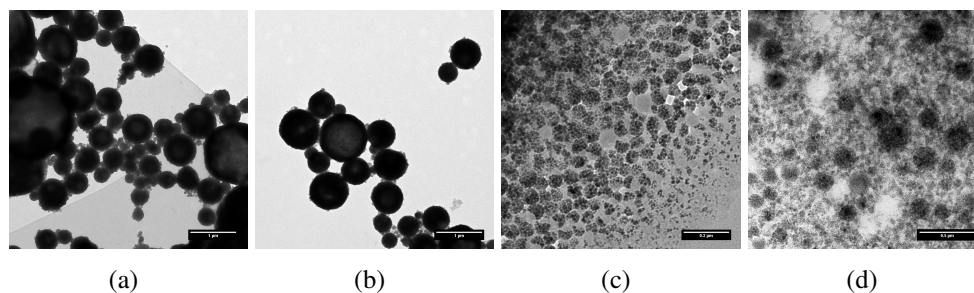


**Figure 3.22:** TEM micrographs of the centrifuged diaminoethyl-functionalized magnetic nanoparticles at 500 rpm (a and b) and the collected supernatant (c and d).

For this reason an additional centrifugation was performed in order to separate the nanoparticles of diameters below 100 nm from those with larger diameters. This goal was quite well achieved using 1000 rpm. The centrifugation yielded a mean diameter of 329 nm with a standard deviation of 40% for the sedimented nanoparticles and a mean diameter of 172 nm with a standard deviation of 55% for the supernatant.

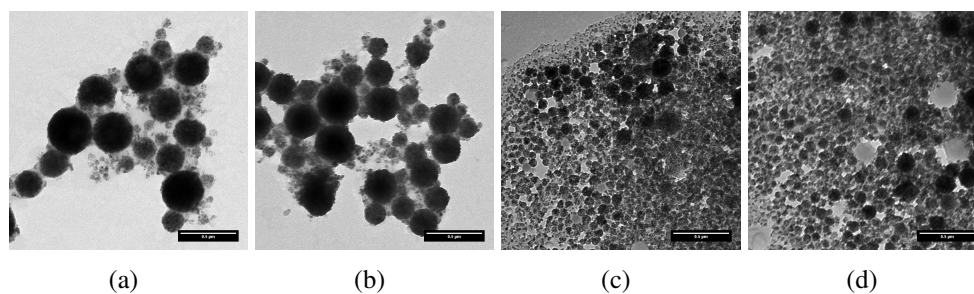


**Figure 3.23:** TEM micrographs of diaminoethyl-functionalized magnetic nanoparticles 1000 rpm (a and b) and supernatant (c and d).

Compared to the nanoparticles removed with the first centrifugation at 500 rpm in Figure 3.22 the removed nanoparticles of the second centrifugation (compare Figure 3.23) have a diameter of half the size of the first centrifugation. The mean diameter was reduced from 600 nm to 339 nm. The amount of small nanoparticles decreased to almost 20% compared to the original sample (see Figure 3.21).

With a major nanoparticle size range between 200 nm and 400 nm, the removed nanoparticles from the 1000 rpm centrifugation have a size distribution suitable for the merging process with copper ions. The sedimented nanoparticles of the 500 rpm centrifugation are too large and undesired branching can occur easily during the merging process. The supernatant of the 1000 rpm centrifugation still contains 5% of nanoparticles with a size between 150 nm and 250 nm. The rest of the supernatant dispersion consists of the very small nanoparticles.

Unfortunately, a further separation of the nanoparticles using centrifugation was not possible. The sedimented nanoparticle dispersion centrifuged with 500 rpm displays a low amount of the small nanoparticles, but a high concentration of large nanoparticles above 500 nm too. This combination is not suitable for the merging process, because a size dependent merging of the different nanoparticles sizes can occur. The nanoparticle dispersion from the sediment of the 1000 rpm centrifugation shows a higher amount of the small nanoparticles of 40%. Even though the amount of small nanoparticles is much higher than for the sediment of the 500 rpm centrifugation, the remaining 60% of the dispersion fulfill the criteria of size and magnetite distribution for the merging process. Compared to the size separation of the standard magnetic polystyrene nanoparticles, the removal of small nanoparticles is more difficult for *N*-methyl diaminoethyl functionalized nanoparticles. Even for low centrifugation forces the small nanoparticles cannot be removed completely. A reversible addition of small nanoparticles to the larger ones caused by hydrogen bonding during the centrifugation process is a possible reason. Furthermore, the problem of the difficult removal of the supernatant after the centrifugation contributed to the high amount of small nanoparticles.

### 3.3.2 Synthesis of *N*-methyl-diaminoethyl functionalized nanoparticles stabilized with Lutensol AT 50

The nanoparticles stabilized with Lutensol AT 50 had a mean diameter of 267 nm with a standard deviation of 51%. Compared to the SDS stabilized nanoparticles this is an increase

in the mean diameter by 21%. The increase of the mean diameter can be attributed to the larger surfactant layer of Lutensol AT 50 compared to SDS. The steric demanding Lutensol AT 50 molecules create a larger hydrodynamic diameter for the stabilized nanoparticle. The  $\zeta$ -potential of the Lutensol AT 50 sample decreased by 45% from - 56.1 mV to - 25.5 mV. The fact that a neutral potential was not achieved can be explained by the used anionic radical starter and the probable deprotonation of the diamino functionality during the synthesis.

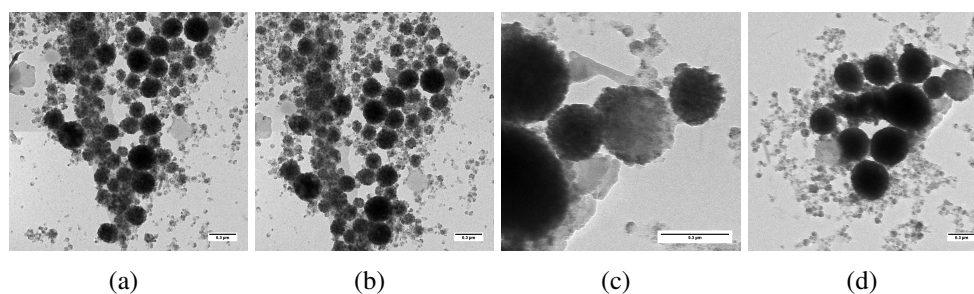


**Figure 3.24:** TEM micrographs of *N*-methyl-diaminoethyl functionalized nanoparticles stabilized with Lutensol AT 50.

The TEM micrographs show a decrease in the amount of the very small nanoparticles by 10% compared to the SDS stabilized nanoparticles. The amount of nanoparticles with a diameter between 200 nm and 350 nm is approximately 65%. Compared to the amount of nanoparticle in that size range present before, this is an increase of 5%. The increase of the amount of larger nanoparticles confirms the result of the DLS measurement. The reason for the increase of larger nanoparticles in the TEM micrographs is different from the DLS result. Since the surfactant layer does not contribute to the nanoparticle size in the TEM micrographs, a certain amount of smaller nanoparticles was removed during the dialysis. In total the TEM micrographs show no difference between nanoparticles stabilized with SDS and nanoparticles stabilized with Lutensol AT 50. The structure and the shape of the nanoparticles did not change during the surfactant exchange. The distribution of magnetite in the nanoparticles is homogeneous and no nanoparticle decomposition was observed. Therefore, the nanoparticles stabilized by Lutensol AT 50 were also used for further investigations on chain formation.

### 3.3.3 *Tert*-butyloxycarbonyl protection of 4-[*N*-(Methylaminoethyl)aminomethyl]styrene and nanoparticle synthesis

For the *tert*-butyloxycarbonyl-protection of 4-[*N*-(Methylaminoethyl)aminomethyl]styrene, a yellow and highly viscous liquid was obtained. The yield was determined to be 60 mg, which is 58% of the theoretical yield.

**$^1\text{H-NMR}$**  (300 MHz,  $\text{CDCl}_3$ ):  $\delta$  7.36 (d, 2 H); 7.19 (d, 2 H); 6.69 (dd, 1 H,  $^1J = 6$  Hz,  $^1J = 3$  Hz); 5.72 (d, 1 H,  $^1J = 6$  Hz); 5.22 (d, 1 H  $^1J = 3$  Hz); 4.43 (d, 2 H); 3.3 (d, 4 H); 2.85 (d, 3 H); 1.47 (d, 18 H)

$R_f$  : 0.51

The synthesized *N*-methyl diaminoethyl functionalized nanoparticles protected with Boc have a mean diameter of 204 nm with a standard deviation of 53 %. The  $\zeta$  potential was determined to be  $\zeta = -46.7 \text{ mV} \pm 5.57 \text{ mV}$ .

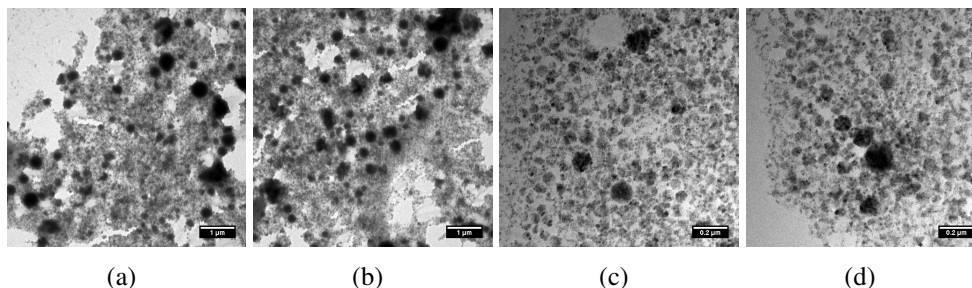


**Figure 3.25:** The dispersion of di-aminoethyl-functionalized magnetic nanoparticles protected with Boc contains a very high amount of small nanoparticles in the TEM micrographs.

Agglomerates of many very small particles are visible in the initial nanoparticle dispersion. The amount of these nanoparticles outnumbers the standard nanoparticle dispersion by far. The nanoparticle dispersion contains almost 98% of nanoparticles with a size below 100 nm and 2% of nanoparticles between 150 nm and 300 nm (compare Figure 3.25). Therefore, the synthesis of Boc-protected nanoparticles can be seen as not as effective as the standard synthesis with unprotected 4-[*N*-(methylaminoethyl)aminomethyl]styrene. Nevertheless, a purification by centrifugation was attempted. The initial dispersion was again purified with a centrifuge at 500 and 1000 rpm for 10 min.

**Table 7:** DLS data of centrifugations of *N*-methyl diaminoethyl-functionalized magnetic nanoparticles protected with Boc.

$\text{rpm}_{\text{centrifuge}}$	$D_H / \text{nm}$	$\sigma_{DLS} (\%)$
0	204	53
500	486	53
1000	320	41

The DLS data of the three centrifugations shows a similar distribution as for the unprotected *N*-methyl-diaminoethyl functionalized magnetic nanoparticles centrifuged at 500 rpm and 1000 rpm.

The first centrifugation at 500 rpm decreased the amount of small nanoparticles to 80%. As shown in Figure 3.26, the amount of nanoparticles in the preferred size range between 150 nm and 350 nm is still very low compared to the dispersion of the unprotected nanoparticles centrifuged at 500 rpm (compare Figure 3.22).



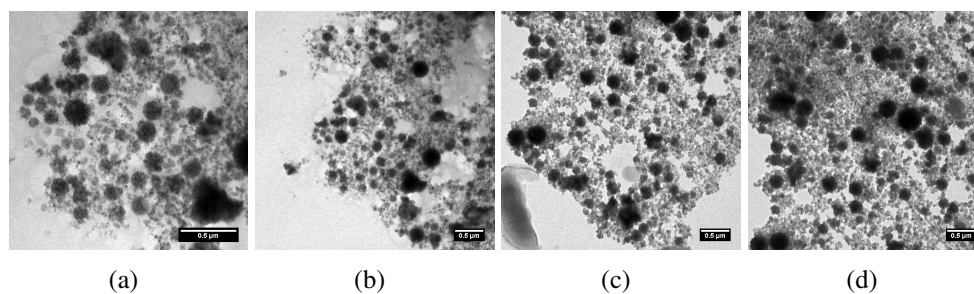


**Figure 3.26:** The centrifugation at 500 rpm for 10 min only increased the amount of nanoparticles between 150 nm and 350 nm in the TEM micrographs.

The removal of the small nanoparticles by centrifugation is more difficult than for the unprotected nanoparticles. The same revolution per min and centrifugation time results in an almost complete removal of the small nanoparticles for the centrifugation of the unprotected nanoparticle dispersion at 500 rpm. Only an enrichment of the larger nanoparticles above 150 nm was observed for the nanoparticles with the protected functionality. A second centrifugation at 1000 rpm for 10 min could further reduce the amount of small nanoparticles to 60% (see Figure 3.27). The mean diameter of the dispersion was 320 nm with a standard deviation of 41%.

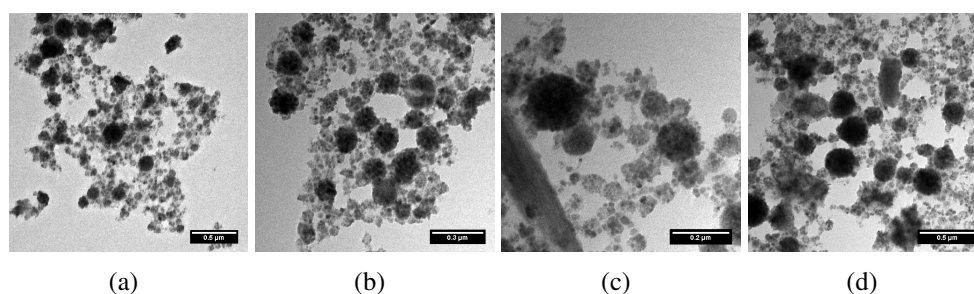


**Figure 3.27:** The centrifugation of the *N*-methyl diaminoethyl functionalized nanoparticles protected with Boc at 1000 rpm could further enrich the amount of large nanoparticles in the dispersion, which is visible in the TEM micrographs.

Although the mean diameter is in an acceptable range, the high amount of small nanoparticles disfavors the use of the *N*-methyl diaminoethyl functionalized nanoparticles protected with Boc for a chain merging experiment. The aim of the synthesis was too narrow the width of the size distribution of the nanoparticles. The protection of the *N*-methyl diaminoethyl functionality should avoid hydrogen bonding and reduce the amount of small nanoparticles. As shown before, the small nanoparticles are difficult to separate from the nanoparticles that possess the size distribution which is preferred for the merging process. Without the presence of the small nanoparticles, an extensive purification would not be necessary. Compared to the nanoparticles synthesized with the unprotected comonomer (compare Figure 3.21), the amount of small nanoparticles increased with the used of the protected comonomer. The TEM micrographs

show a higher concentration of small nanoparticles below 100 nm even after the purification with the centrifuge.

### 3.3.4 Deprotection of the protected nanoparticles

After a reaction time of 24 h the 500 rpm sample was examined with DLS and TEM. The mean diameter decreased by 6% from 486 nm to 457 nm with a standard deviation of 62%. The  $\zeta$  potential was determined to be  $\zeta = -35.3 \text{ mV} \pm 7.53 \text{ mV}$ . A decrease in the surface charge of about 10 mV could be observed. This change can occur due to the protonation of the amino functionalities. Compared to the DLS and  $\zeta$  potential values of the protected nanoparticles, no clear indication for a successful deprotection is can be stated.

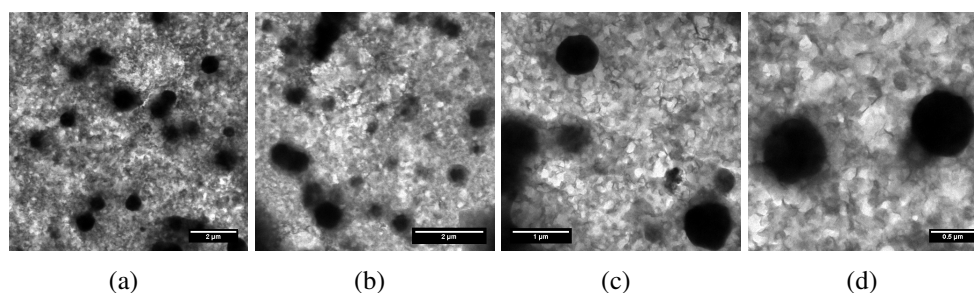


**Figure 3.28:** TEM micrographs of the deprotected diaminoethyl-functionalized magnetic nanoparticles show a decomposition of the nanoparticles.

The deprotection under acidic conditions lead to a destruction of the nanoparticle structure (Figure 3.28). Several larger spherical structures between 200 nm and 500 nm surrounded by decomposed material particle material were visible. It can be assumed that the smaller nanoparticles decomposed during the deprotection process. The high ionic strength that the sulfuric acid creates in the dispersion lead to a destabilization of smaller nanoparticles. They were no longer stabilized by the surfactant and aggregation of small nanoparticles occurred. It was possible to protect the amino functionalities of the monomer with a *tert*-butyloxycarbonyl protection group and to synthesize nanoparticles with the protected comonomer. Unfortunately, the size distribution of the synthesized protected nanoparticles was not improved compared to the nanoparticles with unprotected functionalities. The removal of the protection group under acidic conditions resulted in a nanoparticle decomposition. Since the preparation of the *N*-methyl diaminoethyl functionalized nanoparticles protected with Boc affords more preparation steps and it was not possible to adjust the size distribution of the nanoparticles towards a majority of nanoparticles with a size between 200 nm and 300 nm. Therefore, the direct use of *N*-methyl-diaminoethyl functionalized nanoparticles without the protection group was favored for the merging process.

### 3.3.5 Chain formation of *N*-methyl-diaminoethyl functionalized nanoparticles with copper complexing

A chain merging experiment was performed with the redispersed sedimented nanoparticles of the 1000 rpm centrifugation of JW-27. Copper was used as linker between the nanoparticles.

**Table 8:** The hydrodynamic diameters of the formed nanochain dispersion and the initial initial dispersion of the nanoparticles.

Dispersion	$D_h$ / nm	$\sigma_{DLS}$ (%)
Nanoparticles	320	41
Nanochains	617	60

The mean diameter of the nanochain dispersion increased by 87% with a standard deviation that is 50% larger than the nanoparticle dispersion compared to the mean diameter of the nanoparticle dispersion. In contrast to the nanochains synthesized with the standard nanoparticles, a difference before and after the merging process is visible in the DLS data for the functionalized nanoparticles.

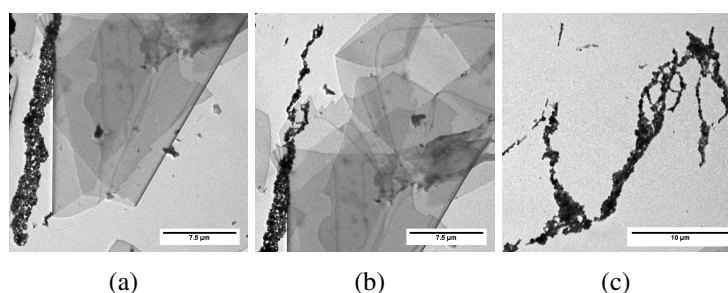


**Figure 3.29:** Large nanochain structures of more than 10  $\mu\text{m}$  could be formed using copper complex as locker for the nanoparticles.

Nanochains with chain lengths exceeding 10  $\mu\text{m}$  are present in the prepared dispersion (Figure 3.29). The nanochains have a thickness of one to five nanoparticles and there are several branching points visible. A magnification of the structures shown in Figure 29(c) displays how the branching points of the nanochains have formed (compare Figure 3.30).

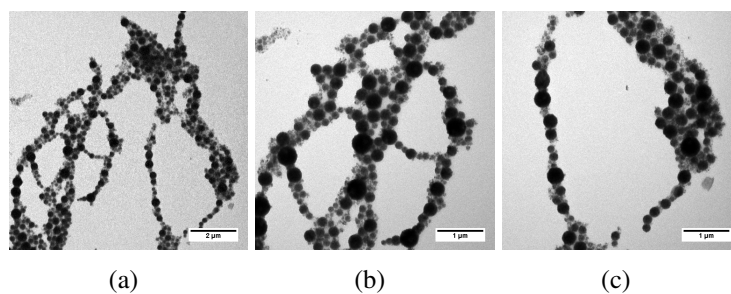


**Figure 3.30:** The magnified areas of the nanochains show a branched structure in the TEM micrographs.

When the magnetic nanoparticles reach the permanent ring magnet, they align in rows and the formation of the copper complex locks them together to form chains. Since there are still free *N*-methyl-diaminoethyl functionalities present at the particle surface and also unlocked copper in the dispersion, collisions between the formed nanochains result in branching points which can be seen in micrograph 30(b). When the local concentration of the nanoparticles and copper ions inside the magnetic field is high, the formation of chain structures with a thickness of three or more nanoparticles is preferred. High local concentrations of nanochains and nanoparticles can occur when the nanostructures are not able to overcome the attraction of the magnetic field. The nanochains and the nanoparticles get stuck inside the magnetic field and the degree of merging increases until the nanochains are able to overcome the magnetic field of the magnet.

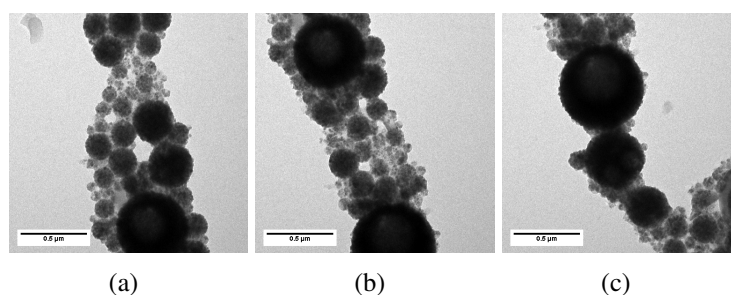


**Figure 3.31:** The magnifications shows that the small nanoparticles are connected between the large ones.

A higher magnification of the nanochains displays how the nanoparticles themselves are linked and even how the linkage between the chains works (Figure 3.31). The nanoparticles are linked in the expected manner, which means they get into touch with each other and form a certain degree of inter-particle entanglement created by the formed copper complexes. The linkage between the collided nanochains is also possible with the very small nanoparticles below 100 nm sizes present. These nanoparticles seem to coordinate in the holes between larger particles using the free ligand positions for complexing with lone copper ions still present in the dispersion.

The average aspect ratio of the nanochains was determined by analyzing the length to width ratio of several chains in the TEM micrographs.

**Table 9:** Determined aspect ratios of nanochains locked with a copper complex.

nanochain	length / $\mu\text{m}$	width / $\mu\text{m}$	aspect ratio
1	8.95	0.76	11.8
2	12.53	0.89	14.0
3	3.67	0.51	7.2
4	6.89	0.42	16.5
5	3.71	0.55	6.8
6	3.52	0.25	13.9
7	6.5	0.45	14.4
8	5.83	0.87	6.7
9	11.3	0.59	19.3
10	1.68	0.33	5.1
11	7.25	0.51	14.3
12	9.05	0.661	14.7
13	24.18	1.85	13.1
14	10.2	0.54	19.0
15	6.3	0.9	7.0
16	18.32	1.5	12.2
average	8.7	0.72	12.3
$\sigma$	5.81	0.42	4.3

The average value for the aspect ratio was 12.3. Nanochains locked with a copper complex had a broad distribution from 5 to 20 in the aspect ratio. The standard deviation of the aspect ratio is 4.3. The distribution originates from the parallel alignment of nanoparticles in the magnetic field where linear assemblies of nanoparticles align parallel to each other. The use of the copper complexing increases the probability that the parallel alignments also fuse resulting in thicker chains. Longer chains have a higher probability that more than one parallel alignment of nanoparticles fused together. Nanochains with chain lengths larger than 10  $\mu\text{m}$  possess widths of 1  $\mu\text{m}$  or higher, whereas nanochains below a length of 5  $\mu\text{m}$  possess a width of 300 nm to 500 nm which is in the diameter range of an average nanoparticle.

Two spectroscopic methods were used to detect the formed copper complex after the merging process, UV-Vis spectroscopy and ICP-OES. With the low copper concentration present in the dispersions it is difficult to determine a possible difference before and after the merging process. For that reason UV-Vis spectra of dispersions with the same concentration of nanoparticles and copper ions were recorded before and after the complex had formed. The two spectra were then normalized by a spectrum of a nanoparticle dispersion without copper with the same nanoparticle concentration as for the copper containing dispersions.

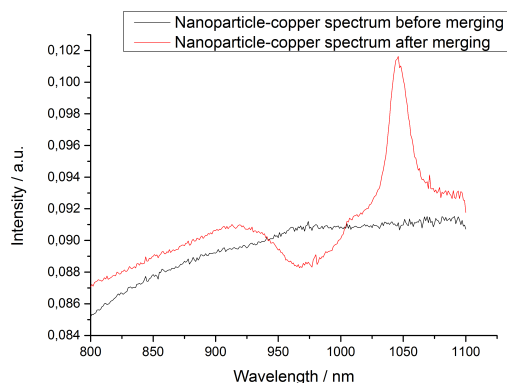


**Figure 3.32:** UV-VIS spectra of the copper containing dispersions before and after merging.

The two spectra in Figure 3.32 show that the absorption spectrum changed after the complexing. The nanochain spectrum shows two differences in the absorption curve compared to the dispersion before the formation process, a broad minimum at  $\approx 970$  nm, followed by a sharp peak at 1046 nm. Since the concentrations of the nanoparticles and the copper salt are exactly the same, the difference in the spectrum originates from the copper complex formed during the merging process.

A spectrum of a copper(II)chloride solution and a solution of a  $[\text{Cu}(\text{en})_2]\text{Cl}_2$  complex with a similar concentration displays a minimum at  $\approx 970$  nm and a sharp maximum at 1045 nm for the complex solution (compare Figure 3.33).

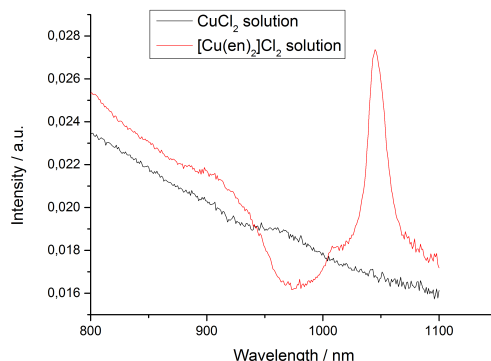


**Figure 3.33:** A spectrum of the copper salt solution and a solution of the formed complex results in the same signal differences as the nanoparticle and nanochain spectra.

The similarity of the complex spectrum and the spectrum of the nanoparticle dispersion after the merging process proves the formation of the copper complex with the *N*-methyl-diaminoethyl functionalized nanoparticles. Furthermore, the missing peaks for the complexing before the merging process shows that the complex is formed during the process. A complexing is only achieved when the distance between the nanoparticles is very low, which is the case when the nanoparticles are directed through the ring magnet and align along the magnetic field. The

UV-Vis experiment shows that the nanoparticles are locked with a copper complex, when they are aligned in a magnetic field.

The ICP-OES measurement afforded an average copper concentration of 1.60 mg/l in the purified dispersion. According to the initial concentration of 4 mg/l, 40% of the copper was complexed in the process. The result displays, that the nanoparticles are strongly attached to the copper complex. A decomposition of the complex is not achieved by reduction of the copper concentration in the continuous phase. The decomposition of the copper complex is only possible with an acidification of the dispersion and so the released copper ions can be detected.

### 3.3.6 Examination of the influence of ultrasound and base on the nanochain dispersion

With the proof that the nanoparticles are locked by a copper complex that is not affected by a change of the copper concentration, the effect of other external triggers was also studied. The sample was treated with ultrasound and base to examine the effect of a mechanical and chemical trigger.

**Treatment with ultrasound** After a 15 min treatment in an ultrasound bath the DLS mean diameter decreased from 617 nm to 283 nm with a standard deviation of 43%. Compared to the synthesized nanochains, this is a decrease of 54%. This is an indication for a decomposition of the nanochains when ultrasound is applied. The TEM micrographs however show that the opposite is the case (compare Figure 3.34).

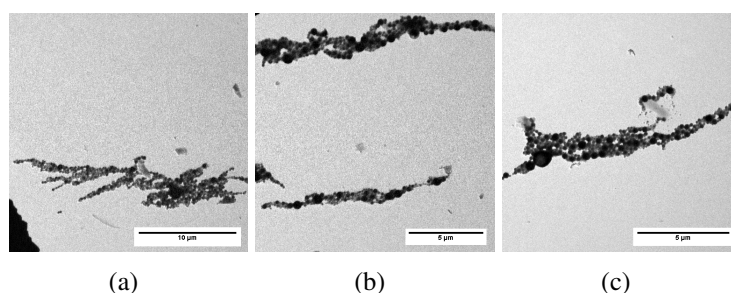


**Figure 3.34:** The mean diameter of the dispersion decreased, but the TEM micrographs still show nanostructures with a similar length as for the untreated nanochain dispersion.

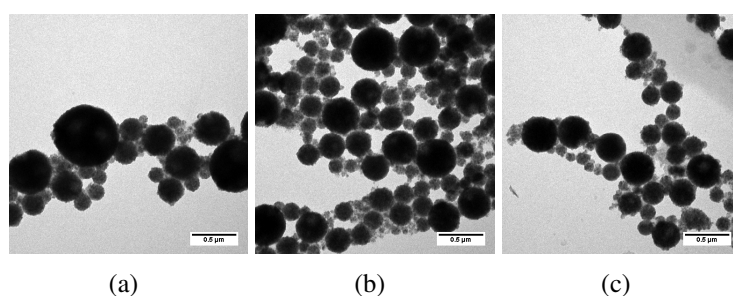
Nanochains with a length similar to the chain lengths of the ones before the treatment are shown in the micrographs. The average chain length exceeds 5  $\mu\text{m}$  and the aspect ratio determined with the TEM micrographs even increased by 6% to 12.9.

**Table 10:** Determined aspect ratios of nanochains locked with a copper complex after treatment with ultrasound.

nanochain	length / $\mu\text{m}$	width / $\mu\text{m}$	aspect ratio
1	11.8	0.78	15.1
2	15.57	0.86	18.1
3	7.12	0.3	23.5
4	4.61	0.44	10.4
5	5.25	0.42	12.4
6	7.61	0.6	12.7
7	7.16	.52	13.9
8	4.93	0.55	8.9
9	6.07	0.83	7.3
10	4.83	0.75	6.4
average	7.5	0.6	12.9

The aspect ratios of the investigated nanochains differ from the ones of the initial sample. Only few nanochains have length of more than  $8 \mu\text{m}$ . The mean chain length is  $1.2 \mu\text{m}$  shorter than for the initial chain dispersion. The nanochains treated with ultrasound have a shorter average length and are  $100 \text{ nm}$  thinner. They appear more linear compared to the nanochains that were not treated with ultrasound. The amount of nanochains with a width of three or more nanoparticles is 15% lower.

The locking pattern between the nanoparticles in the structures did not change compared to the initial sample (Figure 3.35). The nanoparticles are still connected at single points to another one. The nanostructures appear as several nanochains that aligned to a large structure.

**Figure 3.35:** The magnification of the TEM micrographs displays the nanochain structure after a treatment with ultrasound.

The result of the DLS measurement is not conforming with the structures displayed in the TEM micrographs. The reason is still part of current investigations. A possible explanation for the large difference between the TEM and DLS is accredited to the measuring method of the dynamic light scattering. The autocorrelation function of the DLS assumes solid spheres for



the calculation of the mean diameter. The aspect ratio for the spheres is therefore 1. Chainlike nanostructures with aspect ratios of more than 10 do not fulfill the restrictions of the Stokes Einstein equation. Therefore, the autocorrelation function calculates the wrong mean diameter that is too small compared to the values of the TEM examination.

**Treatment with base and ultrasound** The DLS measurement of the basic sample resulted in a mean diameter of 405 nm with a standard deviation of 49%. This is again a decrease of the prior determined mean diameter by 34%. The decrease is not as drastic as for the dispersion treated with ultrasound, but there is still a decrease in almost 200 nm. The TEM micrographs in Figure 3.36 show again long chains.

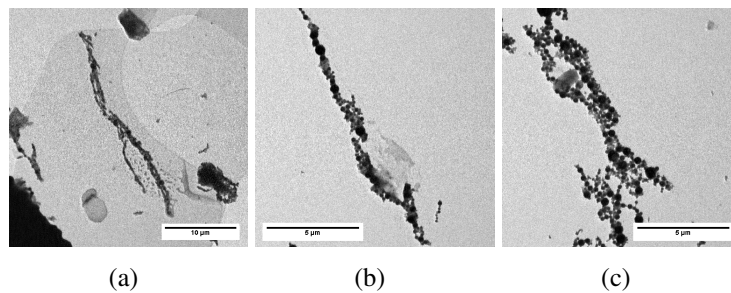


**Figure 3.36:** The TEM micrographs of the created nanochains after ultrasound and base treatment show no difference in comparison with the nanochains before the treatment.

The aspect ratio was determined by the evaluation of the TEM micrographs and also showed an increase by almost 10 % to 13.4 compared to the nanochain dispersion without external triggers.

**Table 11:** Determined aspect ratios of nanochains locked with a copper complex after treatment with base and ultrasound.

nanochain	length / $\mu\text{m}$	width / $\mu\text{m}$	aspect ratio
1	12.0	0.56	21.5
2	8.59	0.72	12.0
3	8.39	0.52	16.
4	5.76	0.79	7.5
5	8.64	0.44	19.9
6	6.67	0.97	6.9
7	2.44	0.31	7.9
8	11.82	0.89	12.0
9	12.18	0.77	15.8
10	6.08	0.57	10.7
11	7.5	0.99	7.6
12	5.89	1.54	3.8
13	12.48	0.52	24.2
14	15.58	0.72	21.6
average	8.86	0.74	13.4

The nanochain dispersion treated with a base possessed an average chain length of 8.86  $\mu\text{m}$ , which is similar to the nanochains without an external trigger. The average chain width increased by 20 nm from 0.72  $\mu\text{m}$  to 0.74  $\mu\text{m}$ . The chain width increases again with the length of the nanochain. Short chains have a small width of one or two nanoparticles, whereas large chains with a length of more than 10  $\mu\text{m}$  possess chain widths of 1  $\mu\text{m}$  and more and therefore a width of more than four nanoparticles. The structures of the assembled nanoparticles show no difference compared to the nanochains observed before the treatment (Figure 3.37). The addition of base to the nanochain dispersion has no effect on the structure of the nanochains. The nanoparticles are connected at several single spots.

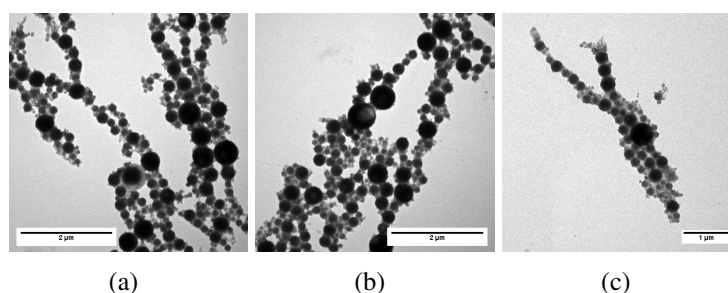


**Figure 3.37:** A magnification of TEM micrographs of the created nanochains after ultrasound and base treatment displays that the nanochain structure did not change compared to the nanochains without a treatment.

A connection between the resulted average values of the aspect ratios and the corresponding DLS data is not visible when the average chain lengths are compared with the mean diameters determined by DLS. The mean diameter is smaller for shorter average chain lengths. The difference between the average diameter of the sample treated with ultrasound and the sample without a treatment is 14%. The mean diameter is also smaller, but with 54% almost 4 times smaller than it is the case for decrease in the average length, but this connection is not present for the sample treated with ultrasound and base. The average chain length increased by 100 nm whereas the mean diameter decreased by 212 nm compared to the nanochains without an external influence.

The aspect ratios increase with increasing standard deviations of the nanochain dispersions. The treatment with ultrasound resulted in an increase of the aspect ratio by 5%, the treatment with base and ultrasound increased the aspect ratio by 9%. The corresponding standard deviations decrease by 28% and 43%, respectively.

**Table 12:** Comparison of average chain lengths, widths and aspect ratios with the mean diameter determined by DLS.

Treatment	length / $\mu\text{m}$	width / $\mu\text{m}$	aspect ratio	$D_H$ / nm	$\sigma_{DLS}$ (%)
No treatment	8.74	0.72	12.3	617	60
Ultrasound	7.5	0.6	12.9	283	43
Base and Ultrasound	8.86	0.74	13.4	405	34

The experiments demonstrated the stability of the copper complex locking the nanoparticles in the nanochains structures. The application of mechanical stress did not affect the structure of the nanochains that was observed before. The addition of base had also no effect on the nanochain structure. The differences in the average TEM values are not large enough to determine a drastic change in the nanochain structure. The disassembly with acid occurs in a sonication bath. If mechanical stress would affect the nanochains drastically, the ability of a differentiation between mechanical stress and the change of the pH value would not be possible.

The stability towards base is beneficial for the reassembly step of the disassembled nanoparticles. The neutralization of the dispersion and the deprotonation of the *N*-methyl-diaminoethyl functionalities after the disassembly should not affect the structure of the nanoparticles and the remaining nanochains.

### 3.3.7 Nanochain formation with Nanoparticles stabilized with Lutensol AT 50

The influence of the surfactant on the merging behavior of the nanoparticles was studied using the *N*-methyl-diaminoethyl functionalities stabilized with Lutensol AT 50. As demonstrated before, the *N*-methyl-diaminoethyl functionalities stabilized with SDS form long chains with a linear structure.

**Table 13:** Comparison of the synthesized nanochains stabilized with Lutensol AT 50 with the corresponding nanoparticles and the nanochains stabilized with SDS.

Dispersion	$D_H / \text{nm}$	$\sigma_{DLS} (\%)$
Nanoparticles (Lutensol AT 50)	267	52
Nanochains (Lutensol AT 50)	234	50
Nanochains (SDS)	617	60

The DLS data of the formed nanochains stabilized with Lutensol AT 50 showed a decrease in the mean diameter. This outcome was unexpected since the nanochains stabilized with SDS possessed a mean diameter that was much higher compared to the nanoparticle dispersion. Similar low size distributions were obtained for the nanochains stabilized with SDS after the treatment with ultrasound and base, but the TEM micrographs of both samples still displayed long nanochains. This was also the case for the nanochains stabilized with Lutensol AT 50 (see Figure 3.38).

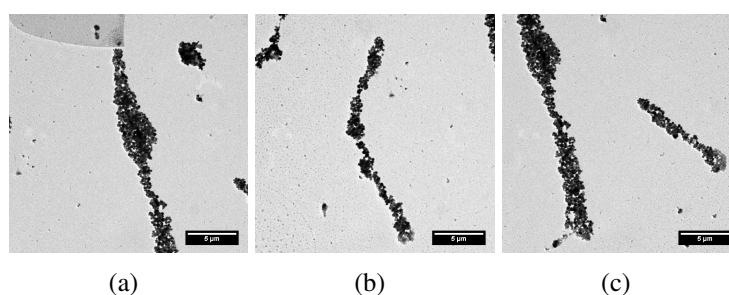


**Figure 3.38:** TEM micrographs of the *N*-methyl diaminoethyl-functionalized magnetic nanoparticle chains stabilized with Lutensol AT 50.

The resulted nanochains stabilized with Lutensol AT 50 have a mean length larger than  $5 \mu\text{m}$ . Compared to the nanochain structures stabilized with SDS, the length of the nanochains is

similar. The thickness of the nanochains stabilized with Lutensol AT 50 with more than five nanoparticles in average is much higher. Furthermore, the nanochains do not have the appearance of several shorter nanochains merged together as it was observed for the nanochains stabilized with SDS. The nanochains stabilized with Lutensol AT 50 appear as a rope of nanoparticles. They are more dense and no branching of chains is visible. A magnification of the nanochain structure in Figure 3.39 displays how the nanoparticles stabilized with Lutensol AT 50 are connected.

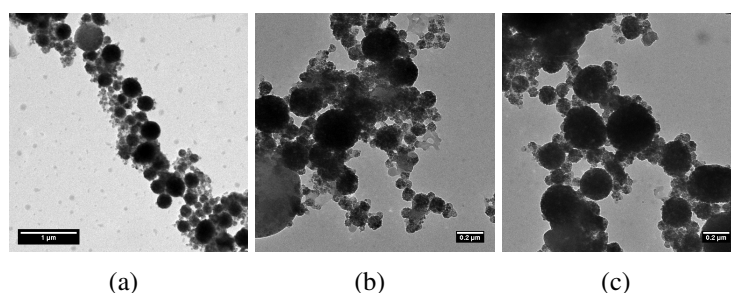


**Figure 3.39:** The magnification of the *N*-methyl diaminoethyl-functionalized magnetic nanoparticle chains stabilized with Lutensol shows a different nanochain structure.

Only in rare cases larger nanoparticles with mean diameter of more than 200 nm are directly connected. The major connection is fulfilled with small nanoparticles below a mean diameter of 80 nm. Therefore the nanochain structures stabilized with Lutensol AT 50 appear more dense compared to the structures stabilized with SDS.

The use of *N*-methyl-diaminoethyl functionalities stabilized with Lutensol AT 50 for a chain merging process with copper is also possible. The lower charge density at the nanoparticle surface lead to thicker nanochains, because more nanoparticles were incorporated. The repulsive effect of the nanoparticles is lower for steric repulsion than for ionic repulsion. Therefore the dipole-dipole attraction in the magnetic field can overcome the repulsive force more easily, when the nanoparticle is stabilized by Lutensol AT 50.

### 3.3.8 pH triggered disassembly of the nanochains

Nanochains were prepared with a dispersion of sedimented *N*-methyl-diaminoethyl functionalized nanoparticles of a 1000 rpm centrifugation to investigate the disassembly behavior.

**Table 14:** Mean diameters and standard deviations of the nanochain dispersion and the nanoparticle dispersion that was used for the chain synthesis.

Dispersion	$D_H$ / nm	$\sigma_{DLS}$ (%)
Nanoparticles	329	40
Nanochains (Disassembly)	440	50

The mean diameter of formed nanochains increased by 25% compared to the nanoparticle dispersion. This is not as high as the increase in the mean diameter of the nanochain dispersion for the investigation of the influence of ultrasound and base. Although the nanochains were prepared in the same way, the increase of the mean diameter is 22% lower for this nanochain dispersion. Furthermore, the resulted nanochains show a different structure (compare Figure 3.40). The incorporation of small nanoparticles in the nanochains is higher and the nanochains show a larger degree of branching.

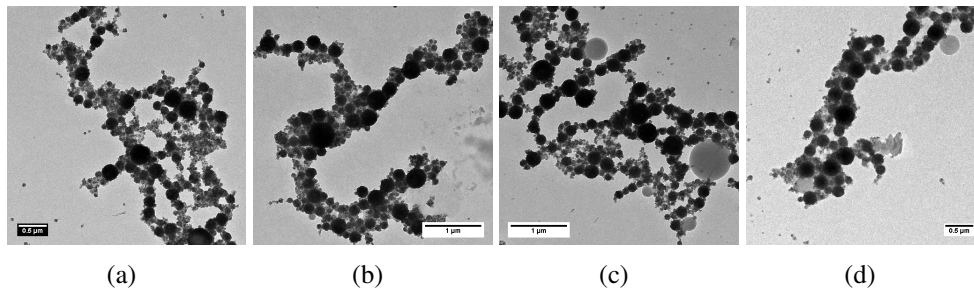


**Figure 3.40:** TEM micrographs of the created nanochains for acidification

The nanochain dispersion however displays a composition of the structures that was observed for the nanochain dispersions before. Nanostructures are formed by combined smaller nanochains. The average aspect ratio of the nanochain dispersion was determined with the evaluation of the TEM micrographs.

**Table 15:** Determined aspect ratios of nanochains locked with a copper complex before the disassembly.

nanochain	length / $\mu\text{m}$	width / $\mu\text{m}$	aspect ratio
1	8.22	0.51	16.0
2	3.6	0.47	7.7
3	5.66	0.39	14.6
4	6.81	0.72	9.4
5	2.67	0.29	9.3
6	3.16	0.28	11.4
7	16.95	0.84	20.2
8	5.19	0.44	11.8
9	4.42	0.35	12.6
10	9.32	0.48	19.4
average	6.6	0.48	13.3

With an average value of 13.3 the aspect ratio is 8% larger than for the first examined nanochain dispersion. The length of an average nanochain is 25% less and they are 33% thinner compared

to the preceding nanochain dispersion that was used for the investigation of the external trigger behavior. To investigate the necessary amount of acid to disassemble the nanochains the nanochain dispersion was acidified with 5, 10 and 15  $\mu\text{l/ml}$  of a 0.1 mol/l hydrochloric acid solution.

**Table 16:** Mean diameters and standard deviations of the nanochain dispersion for the subsequent addition of hydrochloric acid.

Dispersion	$D_H / \text{nm}$	$\sigma_{DLS} (\%)$
Nanoparticles	329	40
Nanochains	440	50
5 $\mu\text{l/ml}$ HCl	296	43
10 $\mu\text{l/ml}$ HCl	262	46
15 $\mu\text{l/ml}$ HCl	250	51

The addition of 5  $\mu\text{l/ml}$  of the hydrochloric acid solution resulted in a decrease in the mean diameter by 33%. The mean diameter of the acidified nanochain dispersion was already below the one of the initial nanoparticle dispersion. The further additions of hydrochloric acid decreased the mean diameter of the nanochain dispersion by 11% and 4%. The decrease of the mean diameters was one third of the diameter of dispersion before. An exponential dependance on the added amount of hydrochloric acid was visible for the percentage decrease of the mean diameter of the nanochains determined by DLS. Each addition of 5  $\mu\text{l/ml}$  hydrochloric acid decreased the mean diameter by 33%.

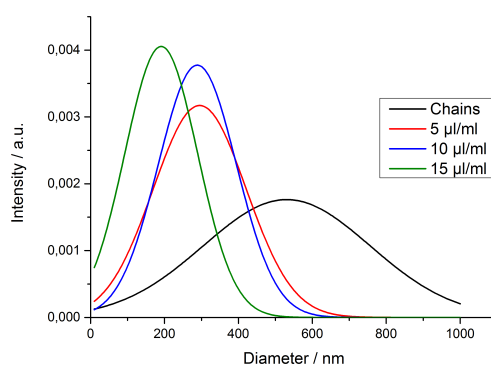


**Figure 3.41:** The acidification of the nanochains with different acid concentrations lead to a decrease in the mean diameter and standard deviation of the DLS values.

The graph shows the decrease of the mean diameter for increasing acid concentrations. Furthermore, the standard deviation decreases with increasing HCl amount. When the nanochains

are formed, the distribution is very broad due to the high anisotropy of the chains. With increasing degree of protonation, the nanochains start to disassemble. The Gaussian distribution curves of the protonated samples are already close to the nanoparticle distribution when 5  $\mu\text{l/ml}$  of the 0.1 mol/l hydrochloric acid is added. Further acidification only slightly affects the mean diameter and the standard deviation.

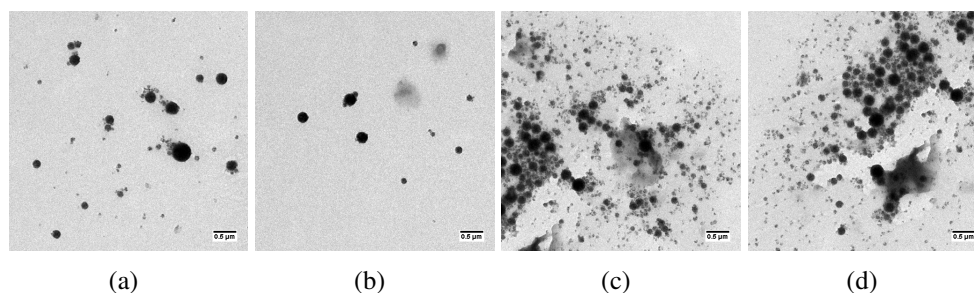


**Figure 3.42:** The nanochains have already disassembled after the addition of 5  $\mu\text{l/ml}$  acid

The micrographs in Figure 3.42 show that the nanochains disassembled. No nanochains were found in the 5  $\mu\text{l/ml}$  sample. Several single nanoparticles are visible without any aggregation around them. The areas of a higher nanoparticle amount visible in micrograph 42(c) and 42(d) can be accredited to drying effects. The aspect ratio of this sample was determined according to the TEM micrographs.

**Table 17:** Determined aspect ratios of nanochains locked with a copper complex after the disassembly.

nanochain	length / $\mu\text{m}$	width / $\mu\text{m}$	aspect ratio
1	0.431	0.248	1.7
2	0.37	0.21	1.8
3	1.34	0.48	2.8
4	0.48	0.16	3.1
5	0.94	0.43	2.2
6	0.21	0.27	0.8
7	1.26	0.43	2.9
8	0.4	0.5	0.8
9	0.49	0.33	1.5
10	0.51	0.17	3.0
average	0.58	0.33	1.9

There is a decrease in the average aspect ratio by 91%. The average length also decreased by 91%. With the micrographs, the DLS data, and the values of the aspect ratio it can be



stated that the pH-triggered disassembly of the nanochains was already successful for an acid concentration of  $5 \mu\text{l/ml}$ .

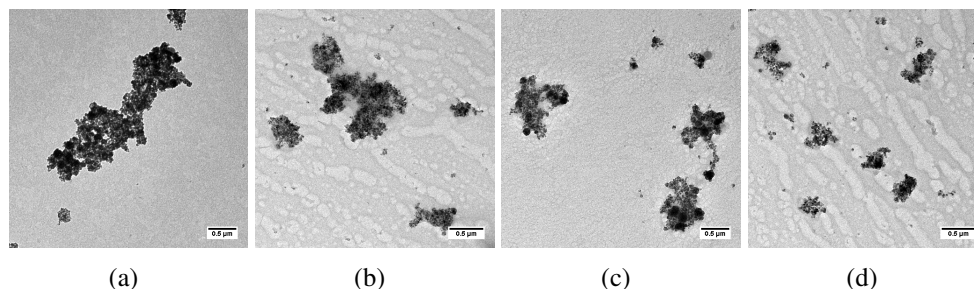


**Figure 3.43:** The addition of  $10 \mu\text{l/ml}$  hydrochloric acid results in the decomposition of the nanoparticles in the TEM micrographs.

The addition of  $10 \mu\text{l/ml}$  changed the appearance of the nanoparticles (compare Figure 3.43). The nanoparticles decomposed and aggregates of the nanoparticle residues were formed. Some spherical structures with a diameter of  $200 \text{ nm}$  are visible in the TEM micrographs. They are surrounded by the aggregates of magnetite. Adding  $10 \mu\text{l/ml}$  of a  $0.1 \text{ mol/l}$  HCl solution already destroyed a high amount of nanoparticles. The addition of  $15 \mu\text{l/ml}$  resulted in a complete decomposition of the nanoparticles (Figure 3.44). The high amount of acid in the dispersion lead to a destabilization of the nanoparticles. A high concentration of ions in the dispersion lowers the electrostatic force that prevents the nanoparticles to aggregate. The aggregation results in the loss of the spherical shape of the new formed structure.

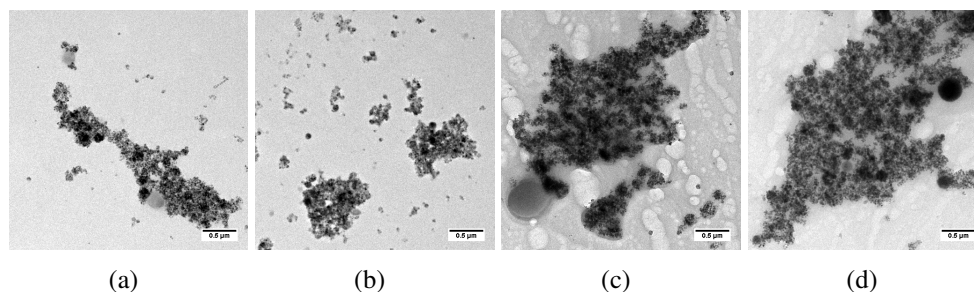


**Figure 3.44:** TEM micrographs of the  $15 \mu\text{l/ml}$  acidification.

All nanoparticles decomposed and only aggregates are visible in the dispersion (Figure 3.44) with the addition of  $15 \mu\text{l/ml}$  hydrochloric acid. In conclusion, it can be stated that an acidification of the nanochain dispersion with more than  $5 \mu\text{l/ml}$  of a  $0.1 \text{ mol/l}$  HCl leads to a decomposition of the nanoparticles because the low pH destabilizes them and aggregates are formed.

The pH triggered disassembly of the nanochains was further studied for lower acid concentrations. The mean diameter of the nanochain dispersion as well as the pH was determined

after a stepwise addition of 1, 2.5, 5 and 10  $\mu\text{l/ml}$  of the 0.1 mol/l HCl solution. A possible connection between the mean diameter and the pH was also evaluated (compare Figure 3.45).

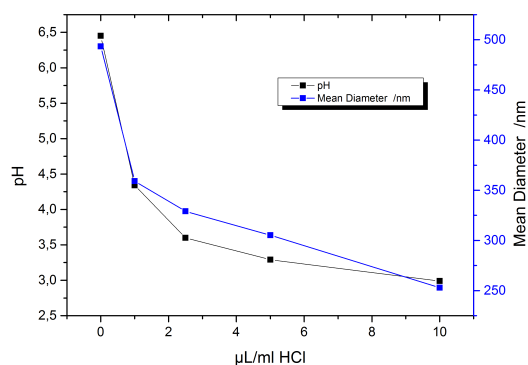


**Figure 3.45:** pH curve with increasing acidification and the corresponding mean diameter of the dispersion.

The curves show an exponential decrease of the pH and the mean diameter with an increasing acid concentration. The black curve displays the pH dependence of the addition, whereas the blue curve the dependence of the mean diameter. Remarkably, a drastic decrease in pH and mean diameter already occurred for the addition of 1  $\mu\text{l/ml}$ . The pH drops from a rather neutral pH of 6.5 to 4.3 while the mean diameter decreases from almost 500 nm to  $\approx 350$  nm. The slope of both curves decreases with increasing amount of acid. The decomposition of the nanoparticles begins at a pH between 3.25, which is the pH for the 5  $\mu\text{l/ml}$  addition, and a pH of 3. So it is a narrow range between disassembly and decomposition of the nanoparticles. The decrease in the mean diameter can be better explained taking the Gaussian distribution curves of the mean diameters displayed in Figure 3.46 into account.

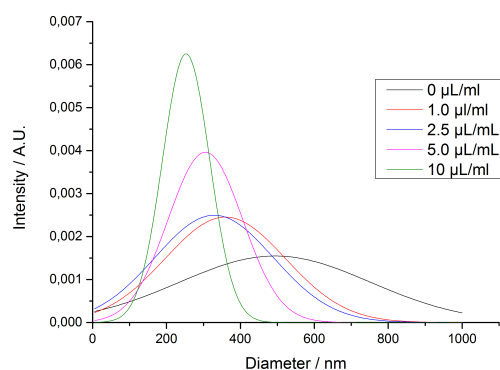


**Figure 3.46:** The Gaussian distribution curves of the acidification steps visualize the disassembly of the nanochains by the subsequent addition of hydrochloric acid.

On the basis of the Gaussian distribution curves of the mean diameters it can be distinguished

at which pH the disassembly of the nanochains begins. While the nanochain dispersion has a broad distribution, the addition of 1 and 2.5  $\mu\text{l/ml}$  HCl results in a decrease of the mean diameter and the standard deviation becomes more narrow. The two samples still show a distribution different from the nanoparticle dispersion distributions, they are too broad. The addition of 5  $\mu\text{l/ml}$  hydrochloric acid depicts a distribution which can be dedicated to nanoparticles. Since the mean diameter is only decreasing in about 25 nm, it is quite reasonable that the nanochain disassembly takes place within the range of the 2.5 and 5  $\mu\text{l/ml}$  addition.

### 3.3.9 Reassembly of *N*-methyl-diaminoethyl functionalized nanoparticles

The 5  $\mu\text{l/ml}$  HCl dispersion, which still contained copper, was neutralized with 5  $\mu\text{l/ml}$  of a 0.1 NaOH solution and redirected through the magnet to examine the possible reassembly of the *N*-methyl-diaminoethyl functionalized nanoparticles. Nanochains shown in Figure 3.47 were obtained after the merging process. The nanochains had a mean diameter of 320 nm with a standard deviation of 55%.

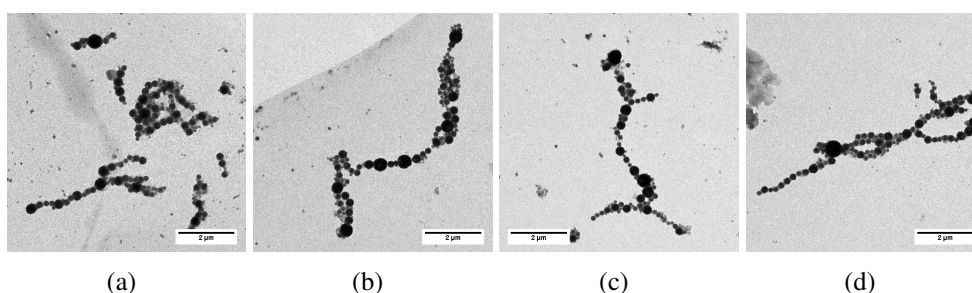


**Figure 3.47:** The TEM micrographs show the reassembled chains.

The reassembled nanochains are not as long as for the first magnetic assembly, but they have a length of several micrometers (Figure 3.47). The nanochains have a thickness of one to three nanoparticles. The thickness is lower compared to the first assembly of the *N*-methyl diaminoethyl functionalized nanoparticles. The reassembled nanochains show a diminished tendency to collide since only a small amount of chains build up by several smaller chains were observed. The TEM images with a higher magnification again allow to have some more insight in the interparticular linkage.

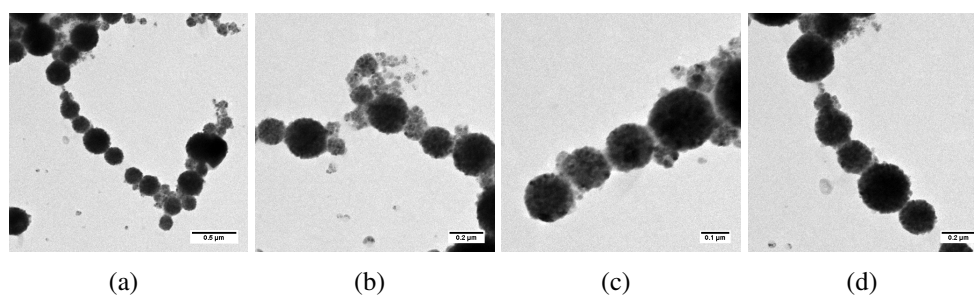


**Figure 3.48:** The magnified TEM micrographs of reassembled chains show no difference to the first assembly.

In Figure 3.48, the connection between the nanoparticles can be seen. As it was the case for the first assembly, the particle linkage is created by an entanglement layer. Therefore a chain like structure resulted by drying effects can be excluded.

### 3.3.10 Conclusion

A pH responsive assembly/disassembly system with *N*-methyl-diaminoethyl functionalized magnetic polystyrene nanoparticles was investigated. This chapter demonstrated the ability of the nanoparticles to align in a static magnetic field into chains using a copper complex as a locking function. The copper complex was stable against mechanical stress and base. Furthermore, the nanochains could be disassembled just by the protonation of the *N*-methyl-diaminoethyl functionality. By choosing the right pH range, a decomposition of the nanoparticles was also avoided. The very effective reassembly of the disassembled nanoparticles at neutral pH in the last part demonstrated the full reversibility of this outstanding system.

### 3.4 Magnetic nanocapsule synthesis and polymer film formation

#### 3.4.1 Synthesis of magnetic nanocapsules

Magnetic nanocapsules were synthesized with two different ratios of *n*-octane and hexadecane. A 1:1 mixture and a 1.5:8.5 mixture of *n*-octane and hexadecane were used and the nanocapsule dispersions were examined with DLS.

**Table 18:** The hydrodynamic diameters of the magnetic nanocapsules synthesized with different ratios of *n*-octane and hexadecane.

Ratio ( <i>n</i> -octane : hexadecane)	$D_H$ / nm	$\sigma_{DLS}$ (%)
1:1	437	31
1.5:8.5	640	38

The hydrodynamic diameters of the magnetic nanocapsules with different ratios differ by 32%. The mixture containing a higher amount of hexadecane possesses a large mean diameter of 640 nm. The increase in the mean diameter is related to the hexadecane amount. The *n*-octane that is enclosed in the miniemulsion droplet evaporates during the polymerization step and the diameter of the droplet decreases. The decrease in the diameter is larger for a higher amount of *n*-octane. Therefore the mean diameter of the 1:1 mixture of *n*-octane and hexadecane is smaller compared to the mean diameter of the 1.5:8.5 mixture.

The micrographs of the nanocapsule dispersion in Figure 3.49 show magnetite polystyrene nanocapsules surrounded by a high amount of magnetite nanoparticles.

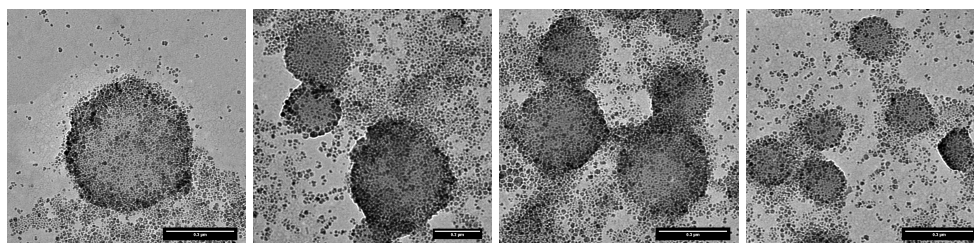


**Figure 3.49:** TEM micrographs of particles with a 1:1 *n*-octane-hexadecane mixture as dispersed phase show magnetic nanocapsules and a high amount of magnetite nanoparticles surrounding them.

The nanocapsule shell contains also magnetite nanoparticles. It is not possible to determine the origin of the  $\text{Fe}_3\text{O}_4$  nanoparticles in the media surrounding the nanocapsules in Figure 3.49. Two different options for the origin of magnetite in the TEM micrographs are possible, the encapsulation of the nanoparticles in the nanocapsules and the existence of magnetite nanoparticles that are dispersed together with the nanocapsules. The nanoparticles would be dispersed in the hydrophobic hexadecane phase inside the nanocapsules in the first option. A release

of the magnetite nanoparticles occurs when the dispersion is dried under vacuum. The hexadecane can evaporate and create a high pressure inside the nanocapsule. It is possible that nanocapsule shell breaks due to the high pressure and releases the hexadecane and the magnetite nanoparticles. The magnetite nanoparticles that surround the nanocapsules would then be a drying artifact of the TEM. The second possibility is that  $\text{Fe}_3\text{O}_4$  nanoparticles are separately dispersed in the nanocapsule dispersion. To distinguish which option is valid, cryo-TEM and field-flow-fractionation (FFF) experiments were performed.

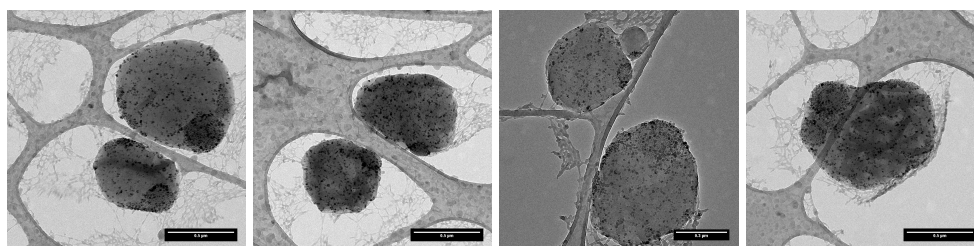


**Figure 3.50:** The presence of free magnetite nanoparticles in the dispersion cannot be stated in cryo TEM.

The magnetite nanoparticles in the cryo-TEM micrographs are situated inside the nanocapsules (Figure 3.50). Remarkably, the encapsulated nanoparticles are not homogeneously distributed in the nanocapsules, but they are concentrated in one certain area of the nanocapsule. This areas possess a high concentration of the magnetite nanoparticles, whereas the rest of the nanocapsules has a homogeneous distribution of  $\text{Fe}_3\text{O}_4$  nanoparticles.

The results of the cryo-TEM experiment show that magnetite nanoparticles are dispersed in the nanocapsule core. But it cannot be excluded that oleate capped  $\text{Fe}_3\text{O}_4$  nanoparticles are also dispersed in the nanocapsule dispersion by only regarding the TEM micrographs. A field flow fractionation (FFF) would afford two clearly separated fractions if magnetite nanoparticles were also dispersed in the nanocapsule dispersion. Due to fractionation principle of the FFF magnetite nanoparticles would elude first, since they possess a small hydrodynamic radius of  $\approx 6$  nm and a high density. The nanocapsules have a much higher hydrodynamic radius and therefore elude later. The field flow fractionation however afforded two different fractions that are not clearly separated (see Figure 3.51 (a)).

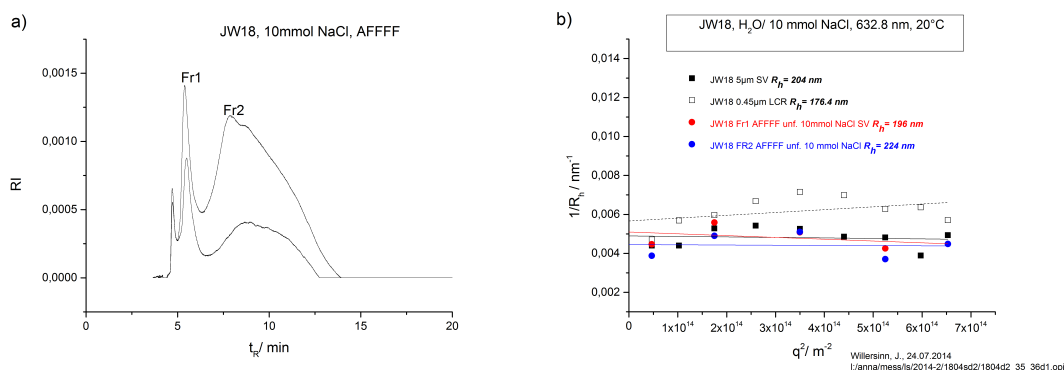


**Figure 3.51:** The FFF of the nanocapsule afforded two different fractions (a) that showed a hydrodynamic radius similar to the dispersion in DLS (b).

One sharp signal is visible at a retention time of 5.5 min and one broad signal at a retention time of 8.2 min that overlaps with the first signal. Assuming that both fractions possess the same refractive index, 16% of the dispersed material can be accredited to fraction Fr1 with a smaller hydrodynamic radius than the other fraction. The amount of fraction Fr2 is therefore 84% of the dispersed material, that possesses a larger  $R_h$ . Furthermore, the first fraction has only a narrow size distribution whereas the second fraction possesses a very broad distribution in the size. The DLS examination of the different fractions results in hydrodynamic radii of Fr1 and Fr2 that are close to the dispersion before the fractionation (see Figure 3.51 (b)).

**Table 19:** The hydrodynamic radii of the nanocapsule dispersion before and after the field flow fractionation were determined with DLS.

Sample	$R_h$ / nm	Amount in dispersion / (%)
Initial dispersion	204	100
Fr1	198	16
Fr2	224	84

The first fraction has a hydrodynamic radius that is with 198 nm 12% smaller compared to the second fraction with 224 nm. A comparison of the hydrodynamic radii of the two fractions with the hydrodynamic radius of the nanocapsule dispersion displays, that the hydrodynamic radius of the nanocapsule dispersion is in between the  $R_h$  of the two fractions. The result of the field flow fractionation and the DLS experiment state that no free magnetite nanoparticles are dispersed in the nanoparticle dispersion. The retention times and the hydrodynamic radii of the two fractions cannot match with oleate capped  $\text{Fe}_3\text{O}_4$  nanoparticles.

The recorded TEM micrographs of Fr1 and Fr2 show a further difference for the two fractions. There is not only a difference in size, but also in the amount of magnetite nanoparticles situated in the nanocapsules (Figure 3.52). The smaller nanocapsules of the first fraction appear to possess a higher amount of magnetite compared to the second fraction. The projections of

the nanocapsules of the second fraction show a structure in the nanocapsule cores, that has a lower electron density compared to the first fraction. Furthermore, the amount of free magnetite nanoparticles surrounding the nanocapsules is much higher for the second fraction.

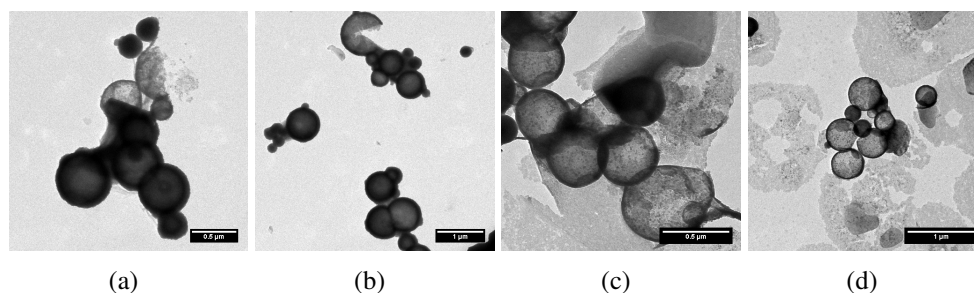


**Figure 3.52:** The smaller nanocapsules of the first fraction (a) and (b) show a higher electron density in the core than the larger nanocapsules of the second fraction (c) and (d).

The field flow fractionation experiment and the DLS examination of the separated fractions stated that the magnetite nanoparticles visible in the TEM micrographs origin from the core of the nanocapsules. No fraction was obtained that possessed a hydrodynamic radius within the range of oleate capped  $\text{Fe}_3\text{O}_4$  nanoparticles.



The magnetic nanocapsules synthesized with a 1.5:8.5 mixture of *n*-octane and hexadecane in Figure 3.53 have a higher concentration of magnetite in the inside of the nanocapsules and also in the surrounding media compared to the 1:1 mixture.

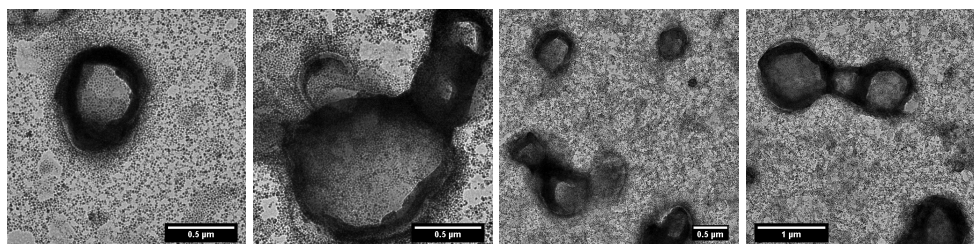


**Figure 3.53:** An increase of the hexadecane amount to 85% results in a larger magnetic nanoparticles that contain more magnetite nanoparticles.

The increase of the hexadecane amount in the mixture of *n*-octane and hexadecane increased the mean diameter of the magnetic nanocapsules and increased the amount of oleate capped  $\text{Fe}_3\text{O}_4$  nanoparticles that were encapsulated in the nanocapsules. A possible explanation for the increased encapsulation is the solubility of the magnetite nanoparticles. The magnetite nanoparticles can only be re-dispersed in *n*-octane. Therefore, the *n*-octane amount is deciding for the solution of the nanoparticles in the mixture. A high amount of *n*-octane results in a better distribution of the magnetite nanoparticles in the organic phase. For that reason, the miniemulsion droplets contain less magnetite since the nanoparticles are equally distributed in the droplets and the organic supernatant that is present after the ultrasonication. A low amount of *n*-octane increases the amount of oleate capped  $\text{Fe}_3\text{O}_4$  nanoparticles in the miniemulsion droplets because the particles have a smaller volume in that they can be dissolved. Under the presumption that the same mixture of *n*-octane and hexadecane is present in the miniemulsion droplets and in the organic supernatant, the encapsulated amount of oleate capped  $\text{Fe}_3\text{O}_4$  nanoparticles is higher for a lower concentration of *n*-octane.

### 3.4.2 Synthesis of the magnetic nanocapsules containing DCPD

In order to be incorporated into a self-healing system, the magnetic nanocapsules need to carry a self-healing agent which is encapsulated in the core. Therefore DCPD was encapsulated in the nanocapsules using a 1:3:5 mixture of *n*-octane, hexadecane, and DCPD. Nanocapsules with a mean diameter of 530 nm and a standard deviation of 42% were obtained using the same preparation method as for the nanocapsules described before.

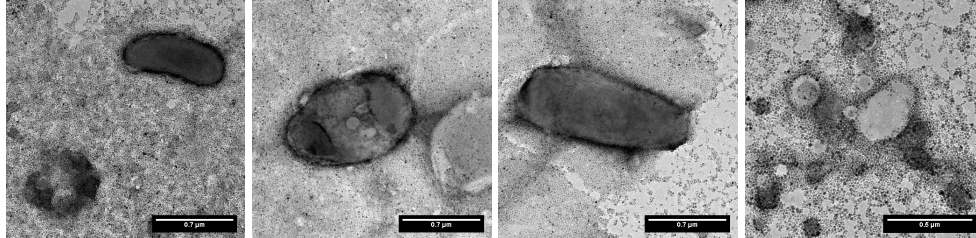


**Figure 3.54:** TEM micrographs of self-healing agent containing nanocapsules.

### 3.4.3 Magnetic polymer films

Four different polymer films were formed with the synthesized magnetic nanoparticles to investigate the effect of the magnetic field on the alignment of the nanocapsules.

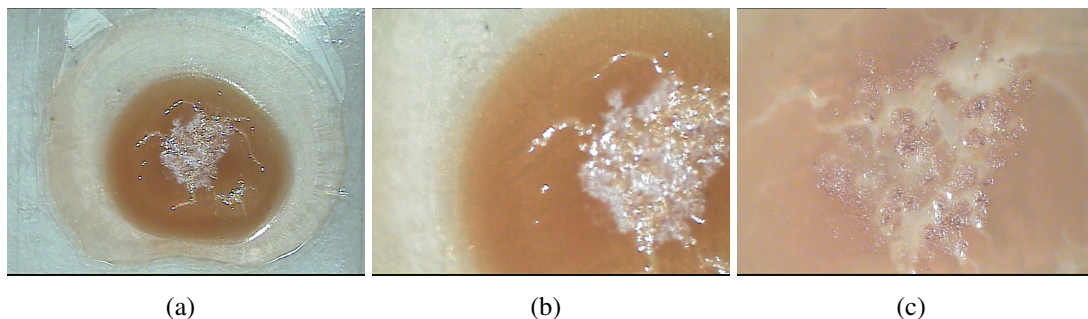


**Figure 3.55:** Optical images of the polymer film that formed without the influence of a magnetic field of the formed film (a), a magnification of the area enriched with magnetic nanocapsules (b) and the furrows formed by the drying effect (c).

**Polymer film without magnetic field** The polymer film formed without the influence of a magnetic field possessed two areas with a different amount of magnetic nanocapsules. The outer area has a slight brown color and therefore a low amount of magnetic nanocapsules (compare Figure 3.55 (a) and (b)). The inner area of the polymer film is of a dark brown color and has higher concentration of magnetic nanocapsules. The center of this area displays a rough surface with many furrows that origin from the drying of the polymer film (see Figure 3.55

(c)). Comparing the outer area with the inner area of the polymer film, a phase separation of the magnetic nanocapsules and the acrylate nanoparticles took place during the drying of the film. With the progress of the evaporation of the continuous phase of the dispersion the acrylate latex nanoparticles get into contact with each other and merge to a polymer film due to their low glass transition temperature. The magnetic nanocapsules possess a  $T_g$  that is much higher than the one of the acrylate nanoparticles and cannot merge with the polymer film. Therefore, the nanocapsules that are not enclosed by the forming polymer film move with decreasing continuous phase to the center of the dropcasted area. The increasing concentration of the nanocapsules in the dispersed phase during the drying process of the polymer film leads to a higher incorporation rate of the nanocapsules into the polymer film. This results in an increasing intensity of the brown color when the center of the dropcasted area is approached. A similar outcome for the drying process on a silicon wafer is also visible in Figure 3.56.

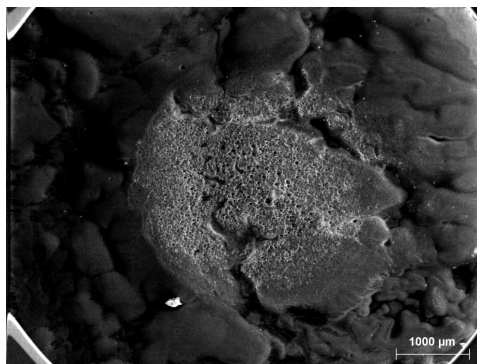


**Figure 3.56:** The SEM micrograph displays the same furrowed structure of the center of the polymer film as it was the case for the film casted on the glass plate.

The center of the polymer film is characterized by the furrows and the porous structure in the surrounding area of the furrows. Unlike the homogeneous distribution of carbon and oxygen atoms in the polymer film in the SEM-EDX mapping experiments, the iron atoms are concentrated in the center of the polymer film, with a high iron atom density for the areas that possess the porous structure. Silicon atoms are only visible at the bottom of the furrows (compare Figure 3.57).

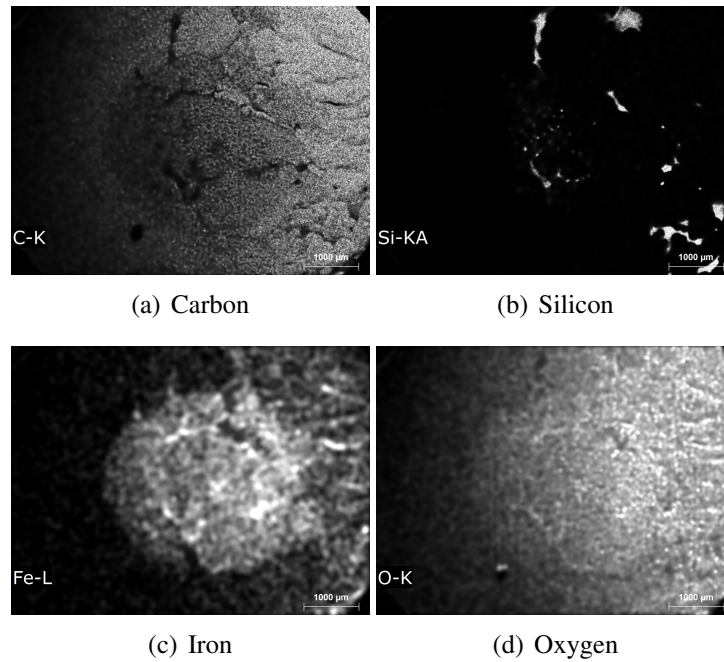


**Figure 3.57:** EDX intensity mapping of the field free polymer film for the elements carbon, oxygen, silicon, and iron results in different atom intensities of the elements, depending on the structure of the polymer film.

The distribution of carbon and oxygen results in the composition of the polymer film and the surfactant of the acrylate dispersion, which consist mainly of these two elements. The difference between the intensity of carbon and oxygen in the center of the polymer film can be explained by a high amount of  $\text{Fe}_3\text{O}_4$  and therefore, a higher oxygen amount compared to carbon present in the center. The high amount of iron in the center of the polymer film can be accredited to the drying effect of the polymer film that was described before.

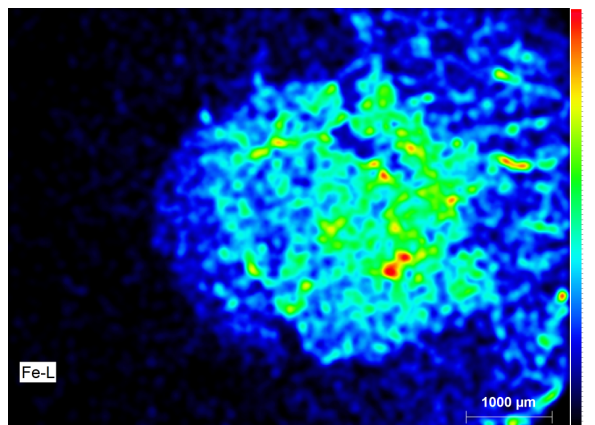


**Figure 3.58:** A color gradient applied on the elemental intensity spectrum of iron shows that the highest amount of the X-rays generated by iron is in the center of the polymer film.

The inhomogeneous distribution of iron was confirmed by applying a color gradient on the elemental intensity of the SEM-EDX measurement. Over 50% of the detected x-rays in the center of the polymer film are caused by iron. Some exposed areas display an even higher amount of more than 90% (compare Figure 3.58). The concentration gradient of the magnetic nanocapsules caused by the drying effect of the polymer film is also visible from the image. The amount of detected X-rays from iron increases from below 10% to a maximum of 95% from left side to the center of the polymer film.

**Cuboid permanent magnet as stimulus** Using a cuboid magnet to generate a permanent magnetic field which influences the magnetic nanocapsules in the polymer dispersion results in the following images after the drying process (Figure 3.59).

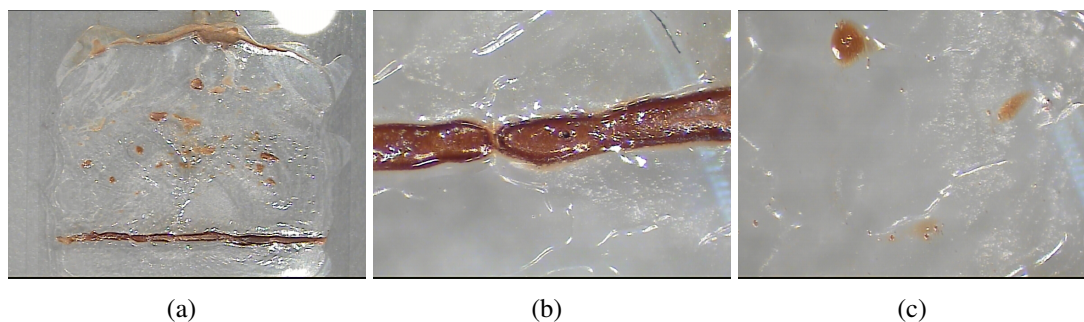


**Figure 3.59:** Optical images of the polymer film with a cuboid permanent magnet as stimulus show the complete polymer film (a), the formed line at the edge of the magnet (b) and the dots in the center of the polymer film (c).

The appearance of the polymer film that was formed under the influence of the cuboid magnet is different to the polymer that formed without a magnetic field (Figure 3.55). The slightly brown color that was present in the polymer film formed without a magnetic stimulus, disappeared. The polymer film is colorless, but a thick brown line at the bottom of the polymer film

and several brown dots with a high amount of magnetic nanocapsules in the center are visible. The thick line and the dots reflect the magnetic field lines of this certain side of the cuboid magnet. The line developed exactly at the edge of the magnet, where the magnetic field lines are the most dense and therefore create the highest magnetic field. The line has the shape of a riverbed, *e.g.* it is oval shaped. Also, an interruption of the line is visible in Figure 3.59 (b). This can be caused by a damage at the magnet edge so that the field lines are less intense there, resulting in less magnetic nanocapsules aligning at this point.

The dots in the center of the polymer film representing the magnetic field in center of the magnet, have no logical explanation. Since no magnetic field lines should origin or end at this points, they might be the result of small defects in the magnetic structure of the cuboid magnet, acting as magnetic hot spots with a high local magnetic field.

The investigations of the line and the dots containing magnetic nanocapsules with SEM-EDX experiments were performed separately. The investigation of the inner structure of the formed line of magnetic nanoparticles was performed with a SEM cross section experiment (see Figure 3.60).

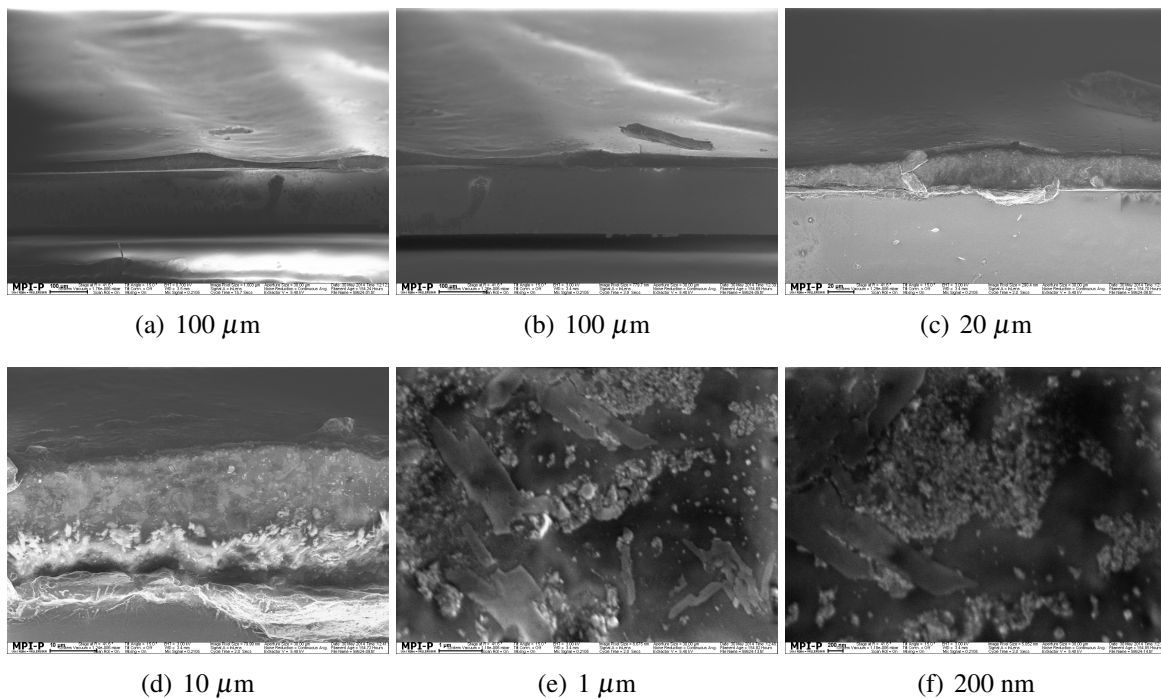
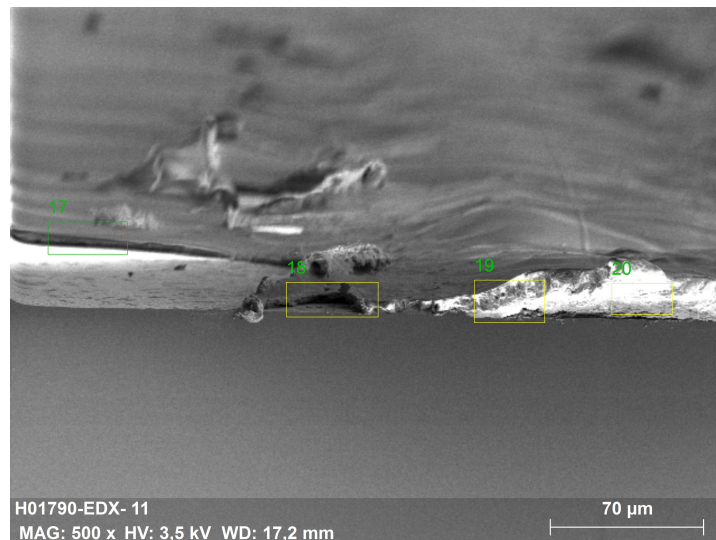


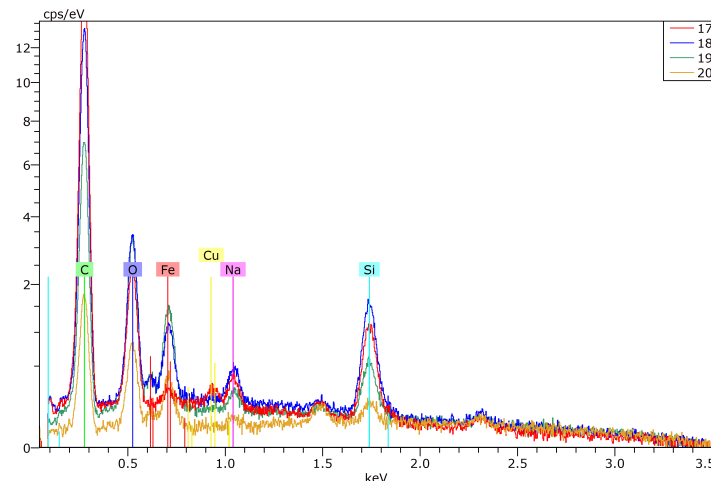
**Figure 3.60:** Cross section micrographs of the polymer film with a cuboid permanent magnet as stimulus.

The concave structure of the nanocapsule containing line with a width of  $700\ \mu\text{m}$  represents the magnetic field lines. The hillocks containing a high amount of magnetic nanocapsules extend over a width of  $200\ \mu\text{m}$  and have a height of  $50\ \mu\text{m}$ . A magnification of the hillock area enabled the determination of the composition of the polymer film. Aggregates of oleate capped  $\text{Fe}_3\text{O}_4$  nanoparticles are visible that are arbitrary distributed in the observed area. The

presence of intact nanocapsules or shell fragments of the nanocapsules was not observed in the micrographs. Furthermore, aggregates of magnetite nanoparticles were observed in areas of the polymer film cross section, where no nanocapsules were expected. The surface was either decorated with magnetite nanoparticles during the preparation of the cross section or the nanocapsules are distributed in the complete polymer film and only concentrate at the area where the magnetic field of the permanent magnet was the strongest. To distinguish between the two possibilities an SEM-EDX spectrum of a polymer cross section was recorded with an acrylate film prepared similar to this polymer film.



(a) Cross section image with examined areas.



(b) Resulting elemental spectra for examined areas.

**Figure 3.61:** The cross section and the corresponding elemental spectra of the SEM-EDX examination of the polymer film with a cuboid permanent magnet as stimulus.

In order to determine the distribution of magnetite in the polymer areas of the cross section

in Figure 3.61 (a) was examined with SEM-EDX spectroscopy. The selected areas should represent a part of the polymer film, where no magnetic nanocapsules were expected (17), an area on the slope of the hillock with a higher amount of iron (18), and two areas where a high amount of the nanocapsules was expected (19 and 20). An increase of the iron peak from the left to the right of the polymer film can be seen in the EDX spectrum in Figure 3.61 (b). The areas 17, 18 and 19 follow the expected increase of the amount of iron. The intensity of the iron peak increases from  $\approx 0.4$  cps/eV to  $\approx 1.2$  cps/eV from area 17 to area 18, and increases a bit more for area 19 to  $\approx 1.6$  cps/eV. This result states the expectations of the alignment of the nanocapsules in the polymer film. Surprisingly, area 20 has only a slightly higher iron intensity than area 17. This is not conform with the expected result. Since area 20 is almost in the center of the hillock, an equal intensity of iron compared to area 19 should be present. A possible explanation for the difference is a damage of this area during the preparation of the cross section. Then, only a thin layer of the polymer film was examined and not a large section as it was the case for the other areas. This would result in a decreased intensity for all detected elements in area 20. The elemental graph of area 20 in Figure 3.61 (b) shows that this is the case.

The experiment demonstrated that the magnetic nanocapsules align and concentrate at the magnetic field. It was still not possible to exclude a random effect, since iron was also detected at area 17 of the cross section where no or at least a very low amount of magnetite should be present. For further insight into the area of the magnetic nanocapsule concentration, the surface of the cross section was also examined with SEM-EDX spectroscopy.

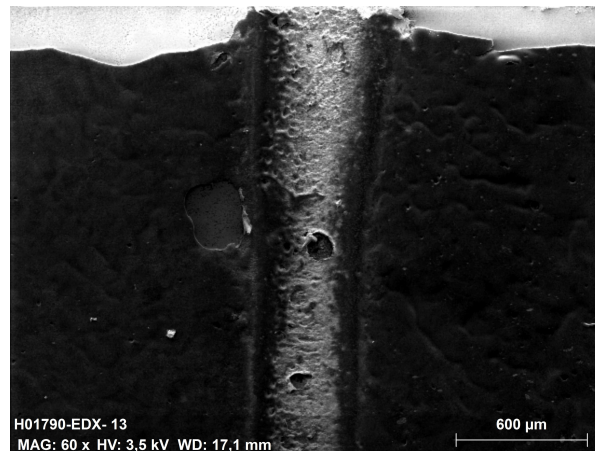


**Figure 3.62:** SEM image of the polymer film surface formed with a cuboid magnet as stimulus.

The surface of the polymer film is divided by a thick line in the center of the micrograph. The line was formed by the influence of the applied magnetic field and should therefore contain the highest amount of the magnetic nanocapsules. Several damages are visible on the polymer film surface. This damaged areas should display a different elemental composition in the SEM-EDX experiment.



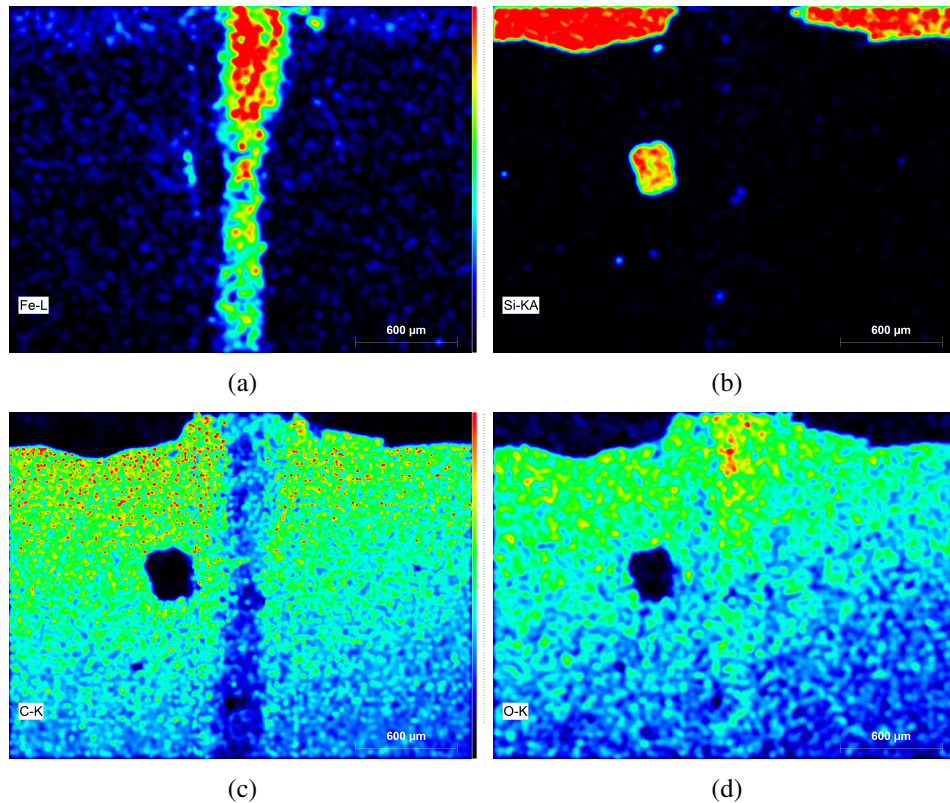


**Figure 3.63:** SEM-EDX examination of images of the polymer film with a cuboid permanent magnet as stimulus.

The elemental examinations of iron, silicon, carbon, and oxygen are shown in Figure 3.63. The major amount of iron is situated in the line in the center of the polymer film. A high concentration of iron is present in the upper region of the line, slightly decreasing towards the bottom of the polymer film. The amount of iron is slightly higher at the edge of the cross section than the amount on the left and right side of the line. For that reason, the previous assumption that the cross section was decorated with magnetite can be stated. A high concentration of silicon and no intensity signal for carbon or oxygen are visible in at the damaged area on the left side of the polymer film. The acrylate film was destroyed at this area and the strong silicon signal is dedicated to the excitation of silicon atoms of the wafer. The presence of magnetite in the line can also be stated by the higher oxygen amount. The area with a high iron concentration shows also a high intensity of oxygen. The high intensity of iron and oxygen in the brown line of the polymer film is consistent with the previous experiments and indicates the predominant alignment of  $\text{Fe}_3\text{O}_4$  and therefore magnetic nanocapsules in the line formed by the magnetic field.

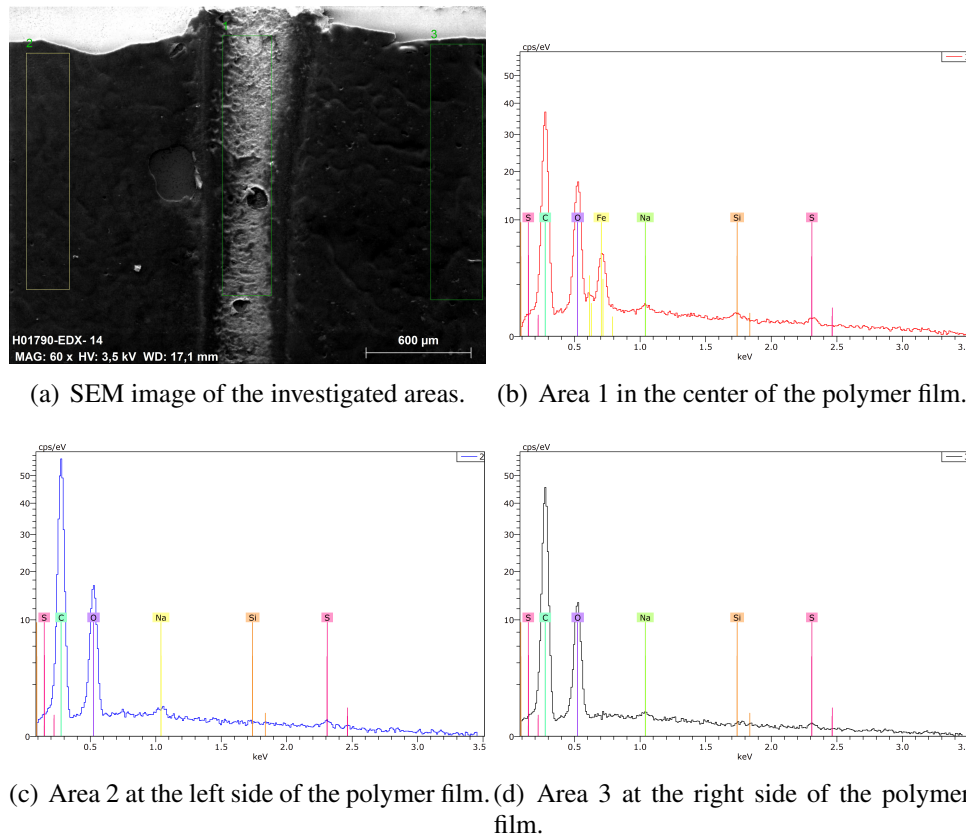


**Figure 3.64:** The SEM-EDX spectra of the mapping examination of the polymer film with a cuboid permanent magnet as stimulus (a) only show an iron peak for area 1 (b) in the center of the film. The spectra recorded in the areas 2 (c) and 3 (d) have no iron peak.

The SEM-EDX spectra of the three examined areas 1, 2 and 3 of the polymer film show that the magnetic nanocapsules are aligned along the line the magnetic field formed. The iron peak of the EDX spectra at 0.7 keV is only present in the central area of the polymer film corresponding to the line (see Figure 3.64 (b)). The areas 2 and 3 do not possess this peak. Furthermore, the spectra 2 and 3 show a higher concentration of carbon and oxygen, than it is the case for spectrum 1 (compare Figure 3.64 (c) and (d)). The differences indicate that the line contains a high percentage of iron and therefore magnetic nanocapsules, respectively. The last measurement performed with this sample was a line scan across the film. This spectrum shows a distribution of the elemental amount of iron, carbon, oxygen, and silicon along the cross section (Figure 3.65).

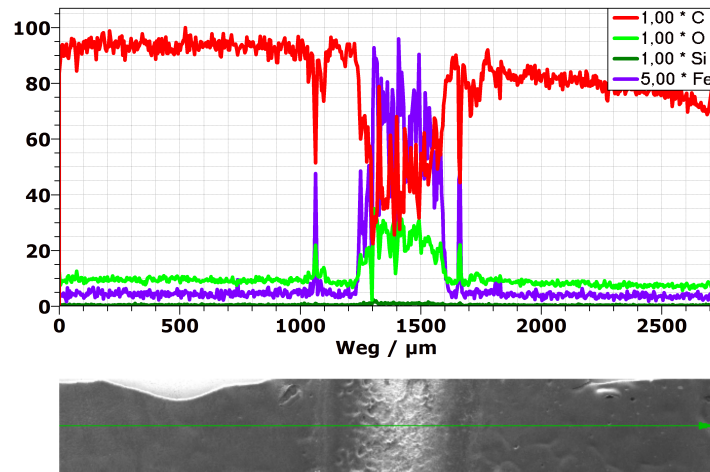


**Figure 3.65:** EDX line scan across the polymer film.

The distribution of magnetic nanocapsules according to the spectrum of the line scan is interesting. The iron intensity has a broad maximum from  $1350 \mu\text{m}$  to  $1600 \mu\text{m}$ , which is consistent with the shape of the line containing the nanocapsules, but four satellite peaks of iron are also visible. The larger satellites can be found at  $1050 \mu\text{m}$  and  $1650 \mu\text{m}$ , the smaller ones can be sensed at  $750$  and  $1850 \mu\text{m}$ . These satellite peaks can also be found for the oxygen spectrum and, in the negative fashion, for the carbon spectrum. The satellite peaks of iron mirror the applied permanent magnetic field of the cuboid magnet. Therefore, it can be assumed that a strong magnetic field originates from the edge of the magnet, followed by a set weaker areas of field lines which decrease the larger the distance from the edge is.

The SEM-EDX experiments demonstrated how the magnetic nanocapsules incorporate in a polymer film when the magnetic field of a cuboid magnet is applied. Despite only the upper layers of the polymer film could be analyzed with this technique, the initial expectations for the film formation and the alignment of the magnetic nanocapsules were stated. Furthermore, an unexpected alignment of the nanocapsules in satellite maxima was observed.

The polymer film that formed in the center of the face of the cuboid magnet (Figure 3.59 (a) and (c)), possessed several spots with a high concentration of the magnetic nanocapsules. The origin of these spots can be ascribed to magnetic disorders inside the permanent magnet. Magnetic disorders cannot be excluded since the used magnet is no high precision tool. However, the magnetic disorders generate hot spots at the face of the cuboid magnet, where magnetic substances concentrate as it is the case for the magnetic nanocapsules used. To demonstrate, that this assumption is also valid for prepared the polymer film, a SEM-EDX spectroscopy experiment was performed with this area (see Figure 3.66).

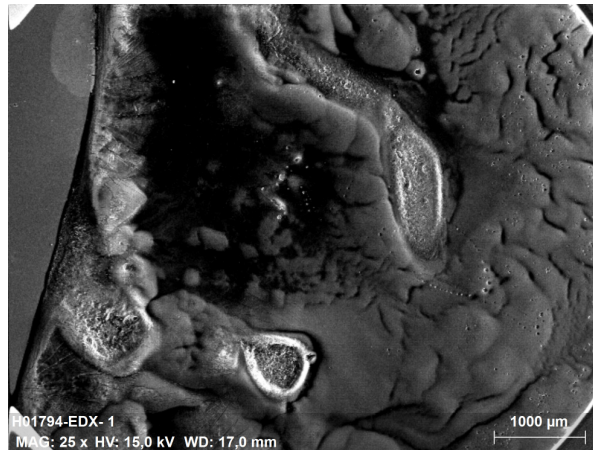


**Figure 3.66:** SEM image of the center of the cuboid magnet examined with SEM-EDX spectroscopy.

The examined polymer film has a similar structure compared to the polymer dropcasted on the glass plate. The two spots in the bottom and the curvy structure, which runs from the center to the top of the image, are the areas where the magnetic nanocapsules are expected. This image also indicates that the magnetic hot spots generated by disorders do not follow any regularity. They appear in a random fashion at the surface of the magnet. The SEM-EDX spectrum of iron shows areas where the magnetic nanocapsules concentrate (Figure 3.67).

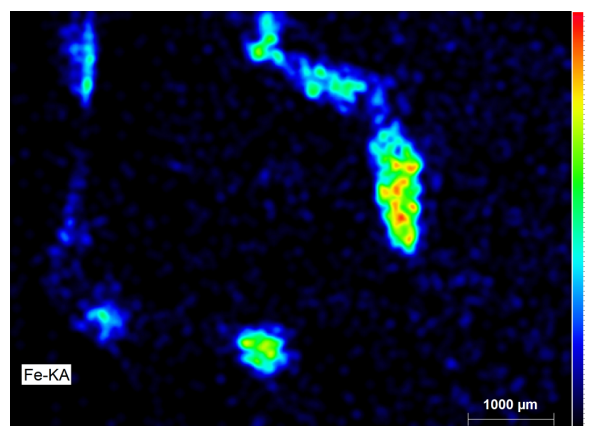


**Figure 3.67:** SEM-EDX elemental spectrum of iron at the center of the cuboid magnet.

The areas where the magnetic nanocapsules were expected, possess a high concentration of iron. The upper left side of the polymer film also showed a higher concentration of iron compared to the rest of the polymer film. It cannot really be stated, if another hot spot is present there or if it is only a drying effect, since it is the end of the polymer film. Compared to the other polymer films, which were created at the edges of the magnets, the concentration of iron and therefore of the magnetic nanocapsules is not that high. For that reason, it can be assumed that the magnetic field strength of the magnetic hot spots is not that large as it is the case for the magnet edges of the magnet.

**Center of a permanent ring magnet as magnetic stimulus** When the acrylate dispersion containing magnetic nanocapsules was dropcasted on a glass plate or a silicon wafer, which was situated at the center, the magnetic field lines directed the magnetic nanocapsules in a way shown in Figure 3.68.

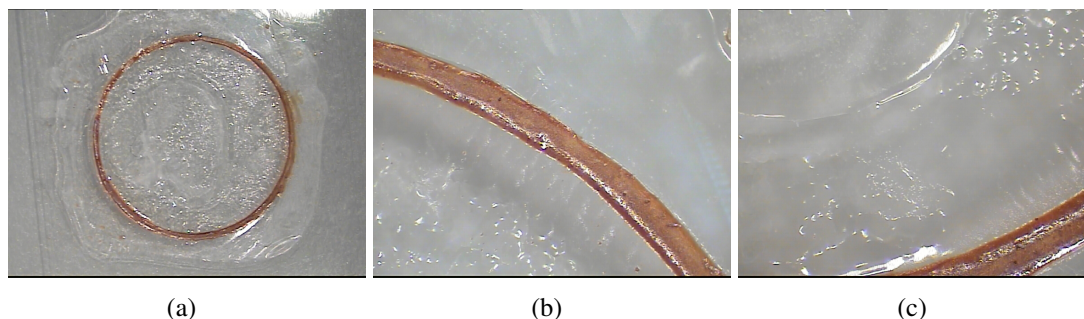


**Figure 3.68:** Optical images of the polymer film with a permanent ring magnet as stimulus show that a ring of magnetic nanocapsules has formed.

The magnetic nanocapsules aligned in a circle following the inner edge of the ring magnet (compare Figure 3.68 (a)). Unlike the cuboid magnet, no random generated hot spots were observed on the surface of the ring magnet. The magnified optical images 68(b) and 68(c) show, that the inner edge of the ring magnet creates a circle following the magnet edge which has the shape of an embankment. The thickness of the magnetic nanocapsule ring is not always identical. Moreover, the divergence in thickness is a result of the concentration of the magnetic nanocapsules in the surrounding area.

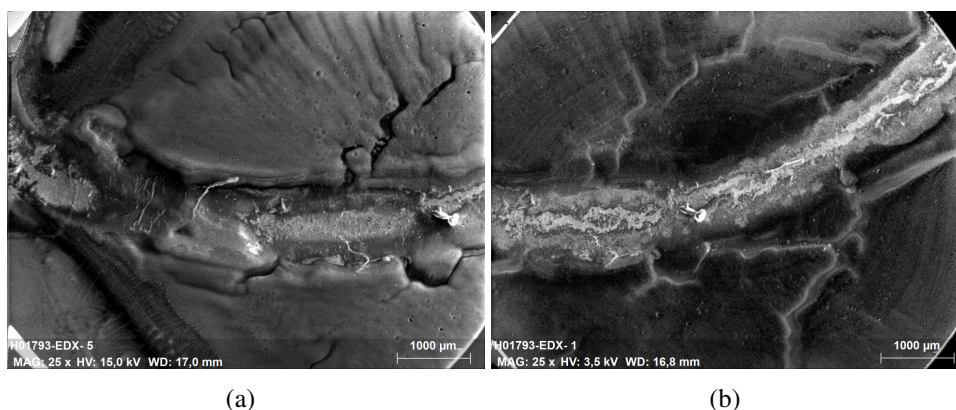


**Figure 3.69:** SEM images of the formed ring with a ring magnet as stimulus performed at 15 kV (a) and 3.5 kV (b).

The formed circle of magnetic nanocapsules in polymer film was investigated with two SEM-EDX experiments at different voltages. The examined areas of the two experiments partially overlap (Figure 3.69). The circular alignment of the nanocapsules in the formed polymer

film can be stated by the SEM micrographs. Furthermore, differences in the thickness of the nanocapsule containing ring that were described before are also visible. The left side of the first micrograph recorded at 15 kV has a turbulent structure of the formed ring containing magnetic nanocapsules, which is caused by a drying effect. Not the complete inner ring of the permanent magnet was covered by the wafer, since only a 20 mm x 20 mm silicon wafer was used. Therefore, the polymer film ends at the left side of the examined area in Figure 3.69. The micrograph recorded at 3.5 kV shows a smooth structure and the ring where the magnetic nanocapsules are expected is not interrupted. The surface of the 15 kV image appears to be more structured, whereas the 3.5 kV image appears rather flat. The reason is that more secondary electrons are generated for a higher voltage and can therefore be detected. This results in a three dimensional appearance of the images recorded at higher voltages. The EDX elemental analysis resulted a distribution of the iron amount in the two parts of the polymer film in Figure 3.70. SEM-EDX experiments were performed with both areas and the elemental amount of iron was recorded (Figure 3.70).

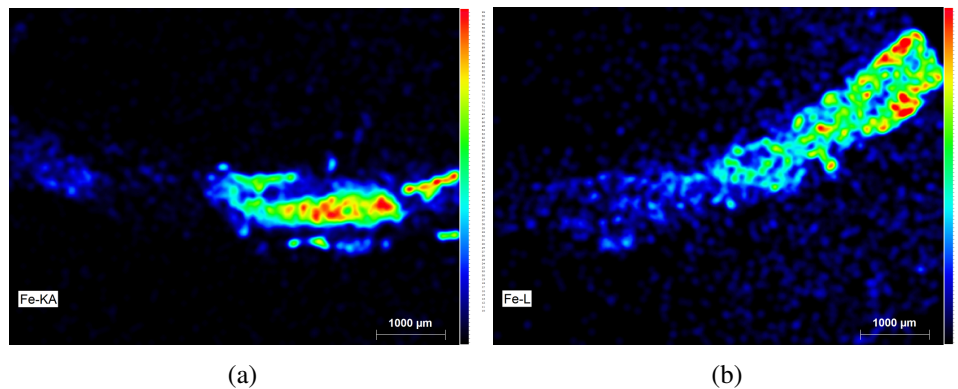


**Figure 3.70:** EDX images of the formed ring with a ring magnet as stimulus performed at 15 kV (a) and 3.5 kV (b).

The strong difference in the intensity of the iron signal is visible between the images recorded at different voltages for the same area. The first iron spectrum was recorded at 15 kV and has a high concentration of iron on the right hand side of the image. Compared to this, the iron intensity in the second micrograph recorded at 3.5 kV has only a low intensity of iron signals at this area, but a high amount in the right part of the film. The different voltages affect also the intensity of the elements in the SEM-EDX spectrum. With higher voltages, layers situated deeper in the polymer film are excited and therefore the spectrum indicates a higher amount of the investigated element than for lower voltages. This can also be confirmed for the elemental spectra of the different areas (compare Figure 3.71). The 3.5 kV spectrum has only one excitation peak of iron at 0.7 keV, while the 15 kV has three peaks, which are at 0.7 keV, 6.4 keV and 7.1 keV, respectively.

The SEM-EDX images show a decrease in the amount of the magnetic nanocapsules going from the right to the left. This decrease is consistent with the expectations, because the thick-

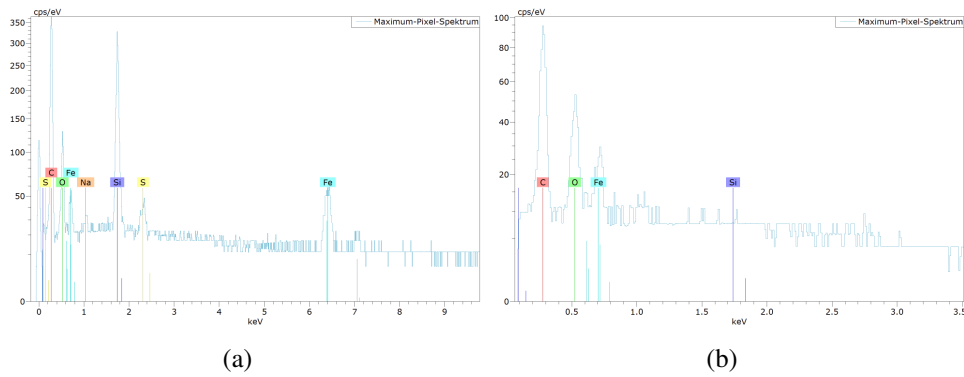


**Figure 3.71:** EDX spectra of the formed ring with a ring magnet as stimulus performed at 15 kV (a) and 3.5 kV (b).

ness of the polymer film is decreasing from the center of the film to the outside. The drop-casting method results in a polymer film where the concentration in the center of the film is higher than at the outside. This also affects the concentration of the magnetic nanocapsules in the formed ring, because more nanocapsules are present in the center.

#### 3.4.4 Conclusion

It was possible to extend the magnetic nanoparticle synthesis to the synthesis of magnetic nanocapsules and to encapsulate the self-healing agent DCPD inside these nanocapsules. Furthermore, these magnetic nanocapsules could be successfully incorporated into a polymer film. Using permanent magnets such as a cuboid and a ring magnet, the polymer films were manipulated to create areas of highly concentrated magnetic nanocapsules and areas where almost no nanocapsules are present inside the polymer film.

## 3.5 Superamphiphobic Surfaces Containing Magnetic Spherical Colloidal Building Blocks

### 3.5.1 First Setup

A magnetic polystyrene nanoparticle dispersion was dropcasted on a heated silicon wafer, which was placed on a permanent magnet. The dispersion was allowed to evaporate under air atmosphere in an oven.

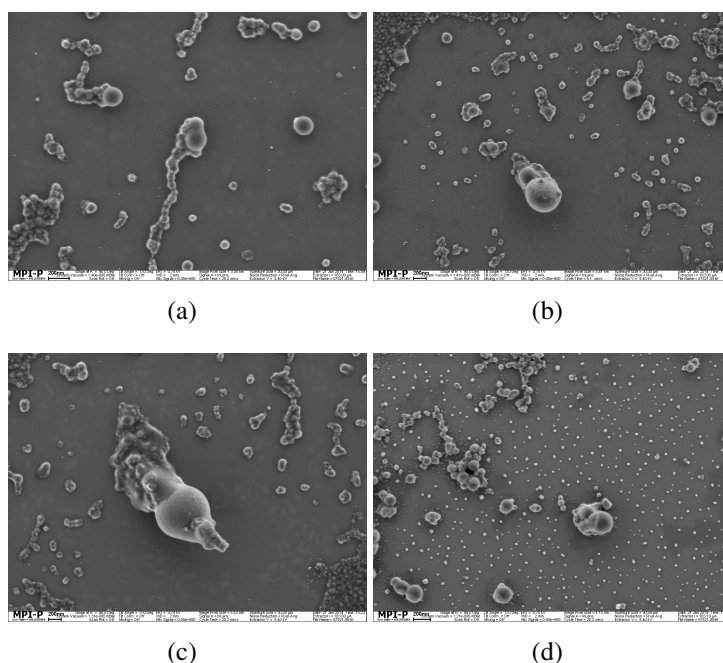


**Figure 3.72:** The first approach towards superamphiphobic surfaces resulted in a low amount of linear assemblies and most of them turned on the silicon wafer surface.

The examination of the surface shows that the concentration of the nanoparticle dispersion was too low (compare Figure 3.72). Only 15% of the silicon wafer was covered with nanoparticles. Nonetheless, linear nanostructures of nanoparticles were observed on the surface. Some linear structures have the appearance of pillars pointing towards the detector Figure 3.72 (b) and (c). Other linear nanoparticle assemblies lie on the surface of the wafer. The low amount of nanoparticles in the dispersion lead to a homogeneous distribution of the nanoparticles on the silicon wafer surface. The application of the magnetic field and heat merged the nanoparticles onto the wafer surface. Nanoparticles in contact with others merged to linear shaped structures, but for a formation of a pillar shaped surface a higher concentration and a smaller surface is necessary. The distance between the nanoparticles in the dispersion is too large to perform a linear assembly of pillar structures. Instead of an assembly onto a nanoparticle that already merged to the surface, the nanoparticles align at the wafer surface too. The possibility that the structure turns onto the surface due to the attraction of the magnet is very high. For that reason, it is difficult to achieve a high amount of pillar shaped nanostructures with this experimental



setup. A method to overcome the problems of a large surface and a low concentration was used in the second setup.

### 3.5.2 Second Setup

A highly concentrated nanoparticle dispersion was filled in a capillary which was fixed on a silicon wafer coated with polystyrene to overcome the problems that occurred in the first experimental setup. The localized spot on the magnet should prefer a pillar shaped assembly of the nanoparticles onto the surface. Furthermore, drying effects can be avoided when the capillary is removed after the assembly process.

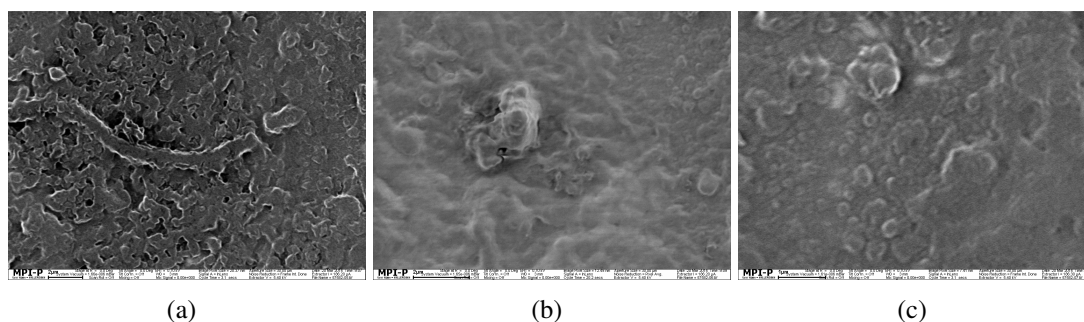


**Figure 3.73:** The second approach towards superamphiphobic surfaces displayed a surface covered with linear shaped assemblies, but the assemblies lie on the surface of the silicon wafer and did not form pillar shaped structures.

As shown in Figure 3.73 the nanoparticles merged with the polystyrene coated surface. Some linear structures of magnetic nanoparticles that merged with the polystyrene surface are visible in the micrographs (Figure 3.73 (a)) as well as several layers of merged nanoparticle assemblies. Other areas show that the nanoparticles merged completely with the surface. Only the shape of some nanoparticles were visible on the surface of the silicon wafer (compare Figure 3.73 (b) and (c)). No pillar shaped structures were observed in this sample. The presence of linear assemblies on the wafer surface could indicate that the pillar structures may have formed during the process, but turned on the surface when the sample was dried. Furthermore, the magnetic attraction of the permanent magnet could also force the linear assemblies to lie down on the surface of the coated wafer.

With the use of a higher concentration of magnetic nanoparticles it was possible to cover the surface of the coated silicon wafer. More linear structures were observed but the strength of the magnetic field was too high to avoid a collapse of the linear assemblies.

### 3.5.3 Third Setup

A last experimental setup was tested with the permanent magnet on top of capillary. The gravity should work as an opposite force for the magnetic force to prevent that possible formed pillar shaped structures overturn and merge with the polystyrene coated surface.

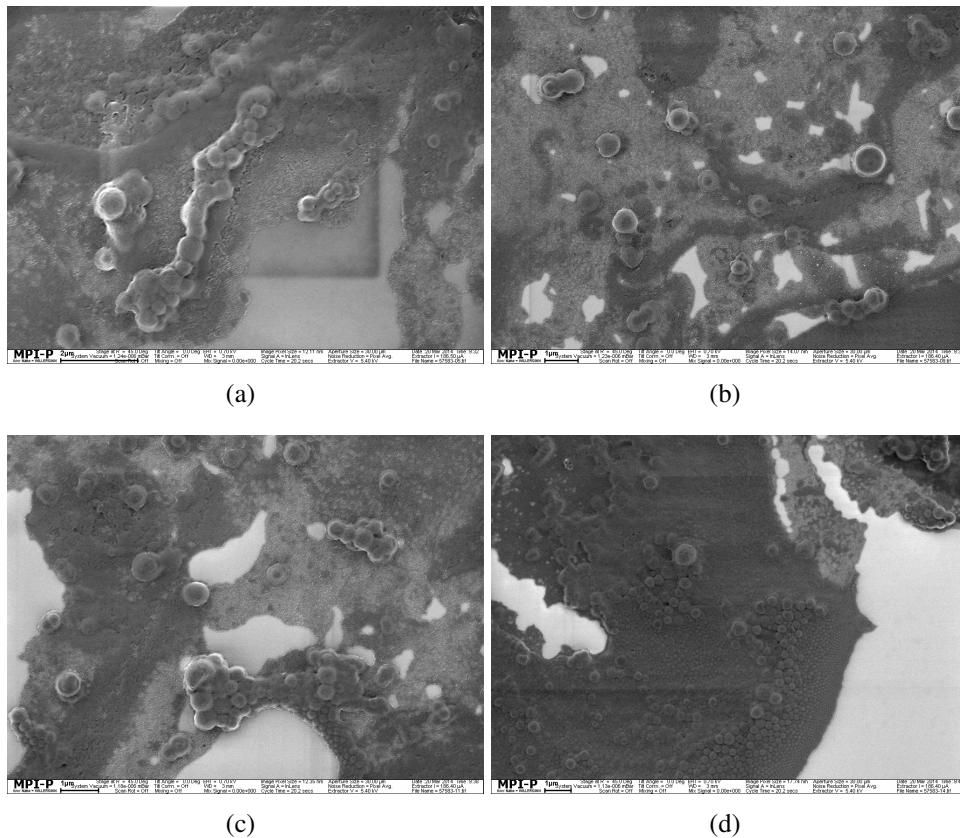


**Figure 3.74:** The third approach towards superamphiphobic surfaces resulted in several layers of nanoparticles fused to the polystyrene coated surface.

Several layers of magnetic nanoparticles aligned on the silicon wafer surface coated with polystyrene (see Figure 3.74). Chain like structures were formed, which appear to be tipped over again. The nanoparticles again formed several layers upon the polystyrene coating. This is clearly visible in 74(d). Here, the layers that are directly on top of the polystyrene coating merged with the polystyrene to a high degree. This degree of merging reduces until the highest layer, where the shape of the single nanoparticles can be recognized. A size separation of the nanoparticles was also observed where smaller nanoparticles align at the interface between silicon wafer and polystyrene coating (compare Figure 3.74 (d)). With increasing distance to this interface, the nanoparticle size also increases. The effect of a stacking of nanoparticle layers is accredited to an artifact of the SEM measurement and the drying of the surface. In conclusion, no superamphiphobic surfaces were formed with this setup. The fact that chain like structures are also visible indicates that the magnetic force is still too strong. Furthermore, the drying of the sample caused an aggregation of the nanoparticle pillars on the surface.

### 3.6 Conclusion

The attempt to create a superamphiphobic surface build up by magnetic polystyrene nanoparticles with a simple setup was not successful. It was possible to attach the magnetic polystyrene

nanoparticles on a surface and also form chain like structures, but several attempts could not prevent these structures to merge with the surface. It seems more complicated to prevent the nanoparticles to completely merge at the surface.

## 4 Summary and Outlook

Within this thesis, the synthesis the merging behavior of magnetic nanoparticles aligned with different triggers and the extension of the magnetic alignment of nanomaterials to novel fields was investigated.

Oleate capped  $\text{Fe}_3\text{O}_4$  nanoparticles were successfully incorporated in polystyrene nanoparticles. The nanoparticle dispersion was size separated with centrifuge into fractions of narrow size distributions. With this technique, six fractions of a different size distribution were obtained. The examination with DLS and TEM displayed that a complete removal of the supernatant of the centrifuged dispersion from the sedimented nanoparticles was only possible to a certain degree. Therefore, the size distributions of the hybrid nanoparticles were not as narrow as desired. But with these narrow distributed fractions of nanoparticles the dependence of the nanoparticle size on the merging behavior can be investigated.

The synthesized nanochains for the investigation of the merging behavior of the magnetic hybrid particles only possessed chain lengths which were not long enough for a statistical investigation of the merging behavior of the different nanoparticle sizes. The experiments showed that the merging of the nanoparticles to linear assemblies does not only depend on the amount or distribution of magnetite nanoparticles inside the polystyrene nanoparticles, the surfactant concentration and the temperature. Furthermore, another parameter affects the merging behavior so that even nanoparticles with well distributed magnetite nanoparticles and a low surfactant concentration do not always show a good merging behavior. Therefore, it was not possible to synthesize nanochains with a chain length of more than 10 nanoparticles. The parameter that affects the merging needs to be investigated for future experiments.

A further project of this thesis was the synthesis of a pH triggered assembly/disassembly of magnetic hybrid nanoparticles. The formation of a pH responsive system was achieved by the use of a comonomer with a *N*-methyl diaminoethyl functionality. The functionality is a good complexing group for many transition metal ions and can be protonated easily. The nanoparticles with the functionalization were synthesized similar to the standard nanoparticles at a higher pH value of continuous phase and examined with TEM and DLS experiments. It was possible to adjust the broad size distribution to an acceptable value using centrifugation. The nanoparticles could also be stabilized with the non-ionic surfactant Lutensol AT 50. With the addition of a low concentrated copper(II) chloride solution during the merging process of the nanoparticles, long nanochains with branching points were obtained. The nanoparticles of these linear structures were linked by a copper complex that formed during the merging process. This was pointed out by a UV-vis experiment, where the absorption peak of the formed complex was visible. The chainlike nanostructures displayed a high stability towards mechanical influences, such as ultrasound and concentration differences of copper in the dispersion solution. The performed ICP-OES measurement afforded a high copper concentration. The nanochains did not disassemble when the copper which was present in the dispersion was completely removed.

The disassembly of the nanochains was performed with a subsequent addition of dilute hy-

drochloric acid. The pH triggered disassembly at a decreasing pH was monitored with TEM and DLS experiments. It was figured out that the synthesized nanochains disassembled at a pH value between 3.5 and 3.0. A further decrease of the pH led to a decomposition of the nanoparticles, which was observed in the TEM micrographs. It was able to reassemble the disassembled chains by neutralizing the nanoparticle dispersion with a sodium hydroxide solution and redirecting the dispersion through the ring magnet. The performed TEM and DLS measurements displayed reassembled nanochains which had a shorter chain length, but showed no difference compared to the first assembly.

The experiments demonstrated that a pH triggered assembly/disassembly system with magnetic nanoparticles can be achieved. Since the used *N*-methyl diaminoethyl functionality is not only able to complex copper ions but for a wide range of transition metals, the complexing of other transition metal ions, such as palladium, iron, and mercury should also be studied in the future. It is also difficult to investigate the length and the shape of the formed nanostructures. TEM micrographs only display a static state of the dried nanochains and DLS measurements cannot resolve the chain lengths. For a better determination of the nanochain shape and size, a new method is necessary that is able to determine the shape and size in the continuous phase. The incorporation of a pigment or a dye could enable an observation of the nanochains in the continuous phase with a different spectroscopic method.

It was possible to synthesize magnetic nanocapsules, that possessed magnetite nanoparticles distributed in the shell and in the core with a modified procedure for the synthesis of the magnetic hybrid nanoparticles. A field flow fractionation of the nanocapsule dispersion showed that no free magnetite was present in the dispersion, but that the concentration of the magnetite nanoparticles is not equal for all nanocapsules. Two fractions of nanocapsules were obtained, one with a higher concentration of magnetite and one fraction with a lower concentration. The nanocapsules however had a similar hydrodynamic radius. The difference in the magnetite concentration was monitored with TEM experiments. Furthermore, nanocapsules with the encapsulated self-healing agent dicyclopentadiene were synthesized.

The synthesized nanocapsules were successfully embedded in an acrylate film. The application of an external magnetic field to the acrylate-nanocapsule dispersion during the drying of the film resulted in a concentration of the magnetic nanocapsules at areas with a high magnetic field. The resulting films showed a distribution of the magnetic nanocapsules that is corresponding to the magnetic field. The formed polymer films were examined with SEM and SEM-EDX experiments. It turned out that the majority of the nanocapsules follow the magnetic field lines and concentrate along them. The surrounding area of the polymer film has a very low concentration of magnetic nanocapsules.

The successful embedding of the magnetic nanocapsules in the polymer film demonstrated that it is possible to manipulate the distribution of the nanocapsules in the polymer film. The next step would be the formation of polymer films with more advanced distributions of the nanocapsules. Therefore more than one permanent magnet could be used. Another point is that the nanocapsules need to be tested for their self-healing behavior. For that reason, the embedding of a catalyst into the polymer film is necessary.

In the last project of the thesis it was tried to form a superamphiphobic surface using the directed self-assembly of the magnetic hybrid nanoparticles. Despite using several different approaches to form linear assemblies of nanoparticles on the surface it was not possible to prevent a collapse of the formed structures and the fusion at the surface.

## 5 Apparatus and Methods

The following chapter discusses the technical devices which were predominantly used for the characterization of the materials produced in this thesis.

### 5.1 Centrifugation

The centrifugation technique is a useful tool for the separation of dispersed or suspended particles with different densities [71]. The particles can be divided into fractions of different densities, by applying a centrifugal force that pushes the particles to the ground.

The sedimentation of the particles is connected to the forces effecting the particle, the surrounding media and the physical properties of the particle itself for a suspension of particles. An important value affecting the sedimentation of particles is the viscosity of the suspending media. A higher centrifugation force has to be applied for a highly viscous media. The frictional force affecting a particle with the radius  $r_p$  was connected with the viscosity by Stokes in the following equation,

$$F = 6\pi\eta r_p \frac{dr}{dt} \quad (5.1)$$

where  $dr/dt$  is the velocity of the particle in the suspension or dispersion. Another important value is the difference in the density between the particle and the surrounding media. For the centrifugation, where the centrifugal forces are much stronger than the gravity, the velocity of a particle is a function of the density difference, the viscosity, and the centrifugal force.

$$\frac{dr}{dt} = \frac{r_p^2 \cdot (\rho_p - \rho_m) \cdot \omega^2 r}{4\eta} \quad (5.2)$$

Here,  $\omega^2$  is the centrifugal force,  $(\rho_p - \rho_m)$  the density difference, and  $r$  the radial distance of the particle to the rotation axis. The connection between the centrifugal force and the sedimentation of the particles shows that the applied centrifugation force decisive for the particle separation. Therefore it is necessary to determine the centrifugation force. By convention, the relative centrifugation force  $RCF$  is given by:

$$RCF = \frac{\omega^2 r}{g} = 11.18 \cdot r \left( \frac{N}{1000} \right)^2 \quad (5.3)$$

where  $N$  is the value for the revolutions per minute of the used centrifuge. The equation for the transfer from revolutions per minute into relative centrifugation force for the centrifuged used in the thesis:

$$RCF = 11.18 \cdot 9.2 \cdot \left( \frac{rpm}{1000} \right)^2 \quad (5.4)$$

With this equation given by Eppendorf, the relative revolutions per minute can be converted to the relative centrifugation forces.

## 5.2 Dynamic Light Scattering (DLS)

The dynamic light scattering technique provides a method to estimate the size as well as the size distribution of a solid particle in a colloidal system [72]. Particles which are dispersed or dissolved in a liquid phase can move through the continuous phase. This Brownian motion can be detected with the irradiation of light. The moving particles scatter the incident light and the Brownian motion is given by the fluctuations of the scattered light with time. For the determination of the velocity of a particle through the scattering volume, only the distance covered by the particle is of importance, not the time which was necessary to that distance. With the velocity it is possible to calculate the hydrodynamic radius  $R_h$  using the self-diffusion coefficient  $D_s$ , which is given in the Stokes Einstein relation for spherical solid particles in 5.5

$$D_s = \frac{k_B T}{f} = \frac{k_B T}{6\pi R_h \eta} \quad (5.5)$$

Velocity and hydrodynamic radius are directly connected in this equation. Since a detailed analysis of the intensity fluctuations over the measuring time is necessary for a determination of  $R_h$ , the time dependent scattering intensity is converted in an evaluable signal with an autocorrelation function.

$$F_s(q, t) = \exp(-D_s q^2 \tau) = \sqrt{\frac{\langle I(q, t) I(q, t + \tau) \rangle}{\langle I(q, t)^2 \rangle}} - 1 \quad (5.6)$$

Here,  $q$  is the scattering angle,  $\langle I(q, t)^2 \rangle$  is the average scattering intensity and  $\langle I(q, t) I(q, t + \tau) \rangle$  is the autocorrelation function. To avoid possible intensity fluctuations caused by fluctuations of the incident beam, a laser is used as light source due to high temporal and spacial coherence in dynamic light scattering. The scattered light from the particles is detected with a photomultiplier at a certain angle. The detected signals from the photomultiplier are then converted by the autocorrelation function from an electric signal to a distribution function, which is examined by a computer.

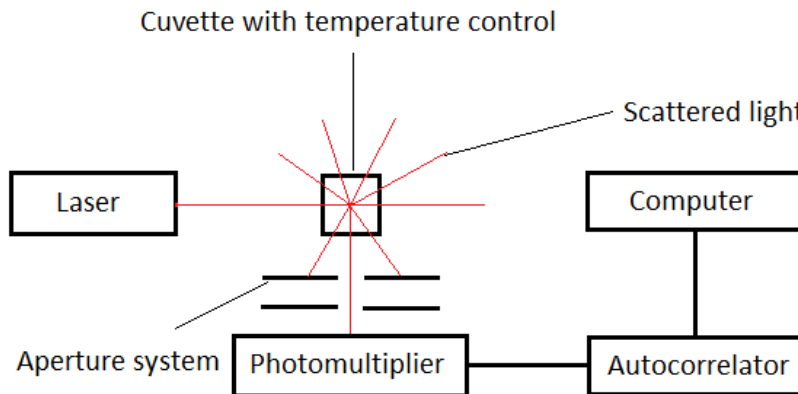


**Figure 5.1:** Light scattering scheme described by Schärfl [72].



### 5.3 Electron microscopy

Electron microscopes enable a pathway for the resolution of the component structure in the micrometer and nanometer scale. This large magnification can be achieved by the use of an electron beam instead of light or other radiation. In principle, two different devices can be used to observe the structure in the nanometer scale with electron microscopy, the transmission electron microscope and the scanning electron microscope.

#### 5.3.1 Transmission electron microscope (TEM)

The transmission electron microscopy has a principle of function which is related to a conventional light microscope [73]. The microscope can be used to resolve structures at a length scale of several micrometers down to a few nanometers. High resolution TEM (HRTEM) devices can be used for a high resolution at even smaller length scales of below the nanometer scale. The generation of electron is carried out with the thermal emission at a thermoionic cathode, which is in many cases a LaB<sub>6</sub>-crystal. The generated electrons are accelerated towards the sample with a voltage between 50 kV and 200 kV and the beam is focused by electromagnetic lenses on the sample. Glass lenses, as they are used in optical microscopy, are not able to focus the electron beam, since the electrons interact with the matter due to their small wavelength. To avoid interactions between the electron beam and air molecules which cause an unfocused beam on the sample, electron microscopy has to be performed under high vacuum conditions. When the focused beam gets into contact with the sample, scattering and transmission of the electrons occurs. The degree of the scattering depends on the structure of the elements the sample contains. Heavy atoms scatter stronger than lighter ones. Also thicker samples scatter more than thinner, since there are more atom layers in the sample. Since only the transmitted electrons will be recorded, the sample needs a certain thickness, which has an optimum at 60 nm. The difference in the scattering intensity between heavy and light atoms can also be used to mark certain areas with heavy atoms to make them distinguishable from other areas with similar atomic composition. The transmitted light from the sample is then focused by electromagnetic lenses and can be detected with a fluorescent screen. CCD cameras are used for the recording of images.

#### 5.3.2 Scanning electron microscope (SEM) and X-ray analysis

Scanning electron microscopy enables the observation and characterization of heterogeneous inorganic and organic materials on a nanometer and micrometer scale [74]. The popularity of SEM technique is due the possibility of generating a three dimensional appearing image of a surface for various surface materials.

For the observation, the surface is screened with a fine focused electron beam, where the electrons are accelerated with a voltage of 0.5 kV to 30.0 kV and focused with electromagnetic lenses on the sample. The signal types are generated by the interactions of the electron beam with the sample. One important interaction is the occurrence of secondary electrons, but also backscattered electrons and X-rays can be detected with a camera. The importance of the image signals of secondary and backscattered electrons relates with the topographic insight

of the surface. The strength of the image signal is directly related to the emission of the secondary electrons at the sample surface, which are generated in a small volume surrounding the primary electron beam. Due to the fine focusing, a high resolution of the image signal can be achieved. The three dimensional appearance of the image comes from the direct connection of the orientation of the sample with the electron beam. Areas of the sample which point to the electron beam appear brighter than areas pointing away from the beam.

The SEM furthermore allows a technique for elemental analysis. The emission of element specific X-rays can be forced with an electron bombardment of the surface created with high voltage. The characteristic X-rays can be used for a qualitative and a quantitative analysis of the element composition of the sample. The characteristic X-rays can be detected with an energy dispersive spectrometer (EDS or EDX). With a mapping mode, not only the surface composition can be detected, but also an element frequency image for the investigated area can be yielded.

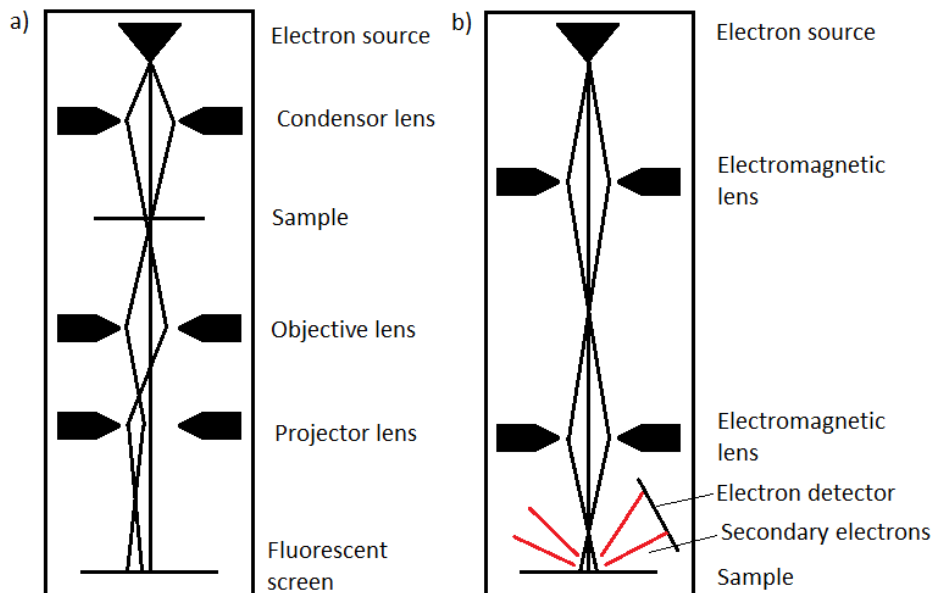


**Figure 5.2:** Schematic images of a TEM (a) and a SEM (b) Beam path described by Goldstein et al. [74].

## 6 Experimental Part

This chapter describes the synthesis of the different magnetic spherical colloidal nanoparticles, different magnetic nanocapsules, the assembly of these nanoparticles into nanochains, and the formation of magnetically manipulated polymer films containing self-healing capsules. Furthermore, the specifications of the used chemicals and the technical equipment are mentioned.

### 6.1 Synthesis of oleate capped $\text{Fe}_3\text{O}_4$ nanoparticles

Oleate capped iron oxide nanoparticles were synthesized after a slightly modified procedure described by Ramirez et al. [60]

12.01 g (60 mmol) of  $\text{FeCl}_3 \cdot 4 \text{H}_2\text{O}$  and 24.36 g (90 mmol) of  $\text{FeCl}_2 \cdot 6 \text{H}_2\text{O}$  were dissolved in 100 ml deionized water. 40 ml of a 28% aqueous ammonia solution were added dropwise within 5 min under rapid stirring with a mechanical stirrer at room temperature. 4.0 g (14.2 mmol) oleic acid were added, and the reaction mixture was heated to 70 °C for 1 h and afterwards to 110 °C for 2 h. The evaporating water was constantly refilled with deionized water. During the heating step, clustering and precipitation of the iron oxide nanoparticles was observed. After cooling the reaction mixture, the resulting black residue was rinsed with deionized water several times followed by drying under vacuum at 40 °C overnight.

To examine the structure of the oleate capped iron oxide nanoparticles, TEM, DLS, TGA, and a saturation magnetization experiment were performed.

### 6.2 Magnetic spherical colloidal building blocks

#### 6.2.1 Synthesis of magnetic polystyrene nanoparticles

The synthesis of the magnetic polystyrene nanoparticles with homogeneously distributed magnetite was done after a modified synthesis by Herrmann et al. [57]. To optimize the particle formation, several experiments were done with different amount of *n*-octane and different ultrasonication times.

1.0 g of oleate capped  $\text{Fe}_3\text{O}_4$  nanoparticles were re-dispersed in *n*-octane and 50 mg oleic acid (0.17 mmol) for 1 h in a sonication bath followed by the addition of 24.0 g of an aqueous solution of 25 mg (0.09 mmol) SDS. The two phase system was sonicated with a tip sonifier under ice cooling and stirred with a mechanical stirrer at room temperature. At the same time, 1.0 g (9.6 mmol) of styrene was mixed with 50.0 mg (0.22 mmol) hexadecane and 24.0 g of an aqueous solution of 10.0 mg (0.06 mmol) SDS and sonicated with a tip sonifier under ice cooling for 1 min (10% amplitude, 5 s pulse, 5 s pause). The dispersion was added to the magnetite dispersion and argon was bubbled through for 7-10 min. 30.0 mg (0.11 mmol) of potassium peroxy disulfate was added to the combined dispersion and the mixture was heated to 80 °C and stirred 40 min. Then 30.0 mg (0.14 mmol) sodium styrene sulfonate were added and the dispersion was stirred additional 7.5 h at 80 °C. Purification of the magnetic polystyrene nanoparticles was carried out magnetically.

**Table 20:** Assessment of different magnetic polystyrene nanoparticles.

Sample	$m_{n\text{-octane}}$ / mg	Sonification time / min	Amplitude / %
JW-04	0.6	3.0	70
JW-05	7.5	3.0	70
JW-09	10.0	3.0	30
JW-10	10.0	6.0	30

The synthesized magnetically purified particles were examined with DLS, TEM, and TGA. Furthermore, the  $\zeta$ -potential was determined.

### 6.2.2 Size-separation of magnetic polystyrene nanoparticles

The size-separation of the synthesized magnetic polystyrene nanoparticles was taken out with centrifugation. Therefore, the particle dispersion was filled in several 1.5 ml centrifugation vials and centrifuged first at 800 revolutions per min for 20 min. After centrifugation, the supernatant was collected with a glass pipette into a new centrifugation vial. The precipitant was re-dispersed with a 1 wt.% SDS solution. The re-dispersed supernatants of each vial were combined and investigated with DLS and TEM. This procedure was done several times with 1000, 1200, 1400, 1600 rpm, and the 1600 rpm, respectively.

### 6.2.3 Chain formation with magnetic polystyrene nanoparticles

The directed self-assembly of the synthesized magnetic polystyrene nanoparticles was carried out previously described by Bannwarth et al. [14].

The initial particle dispersion synthesized in 6.2.1 was concentrated on a magnet. The supernatant was removed with a pipette and the precipitant was re-dispersed with deionized water. This procedure was taken out two times to lower the surfactant concentration to a necessary minimum. A syringe was charged with 2.5 ml of this nanoparticle dispersion and then directed through a capillary passing through a permanent ring magnet with a flow rate of 25, 30, and 35 ml/h. The capillary and the ring magnet are situated in a pre-heated oil bath at 98 °C to ensure that the  $T_g$  of the nanoparticles is reached at the magnet and the particles can merge to nanochains. The collected dispersion was allowed to cool to room temperature and was afterwards purified magnetically. The received nanochains were examined with DLS and TEM.

## 6.3 Synthesis of *N*-methyl-diaminoethyl derived polystyrene magnetic nanoparticles

A locking process of the nanoparticles with a copper complex was performed using the synthesized nanoparticles containing *N*-methyl-diaminoethyl-functionality. To achieve this aim 4-[*N*-(Methylaminoethyl)aminomethyl]styrene was used as comonomer instead of sodium styrene sulfonate was used.

### 6.3.1 Synthesis of the *N*-methyl-diaminoethyl magnetic nanoparticles

1.0 g of oleate capped  $\text{Fe}_3\text{O}_4$  nanoparticles was re-dispersed in 2.0 g (17.5 mmol) *n*-octane and 50 mg oleic acid (0.17 mmol) for 1 h in a sonication bath followed by the addition of 24.0 g of an aqueous solution of 0.032 mol/l NaOH solution containing 25 mg (0.09 mmol) SDS. The two phase system was sonicated with a tip sonifier for 4 min under ice cooling (50% amplitude, 10 s pulse, 5 s pause) and stirred with a mechanical stirrer at room temperature. At the same time, 1.0 g (9.6 mmol) of styrene was mixed with 50.0 mg (0.22 mmol) hexadecane and 24.0 g of a 0.032 mol/l NaOH solution with 10.0 mg (0.06 mmol) SDS and sonicated with a tip sonifier under ice cooling for 1 min (10% amplitude, 5 s pulse, 5 s pause). The dispersion was added to the magnetite containing dispersion and argon was bubbled through for 7-10 min. 30.0 mg (0.11 mmol) of potassium peroxy disulfate was added to the combined dispersion and the mixture was heated to 80 °C and stirred 40 min. Then 20.0 mg (0.1 mmol) of 4-[*N*-(methylaminoethyl)aminomethyl]styrene, which was dissolved 0.5 ml of a 1:1 mixture of 0.032 mol/l NaOH solution and *n*-octane was added and the dispersion was additionally stirred 7.5 h at 80 °C. Purification of the *N*-methyl-diaminoethyl-functionalized magnetic nanoparticles was carried out magnetically and with centrifugation. The synthesized and purified particles were examined with DLS, TEM, and TGA. Furthermore,  $\zeta$ -potential was determined.

### 6.3.2 Synthesis of Lutensol AT 50 stabilized *N*-methyl-diaminoethyl functionalized magnetic nanoparticles

For the complexing with copper chloride and the subsequent acidification, it is beneficial to lower the ionic strength of the dispersion to avoid aggregation before the complexing step takes place. Therefore 10 ml of a *N*-methyl-diaminoethyl functionalized nanoparticle dispersion was dialyzed with a 1 wt.% aqueous Lutensol AT 50 solution to carry out the surfactant exchange from SDS to Lutensol AT 50. The dispersion was dialyzed for 4 d with a mechanical stirrer to avoid precipitation. Within this time, the Lutensol AT 50 solution was exchanged two times. The progress was monitored with a potentiometer. The Lutensol AT 50 stabilized nanoparticle dispersion was examined with DLS, TEM, and  $\zeta$ -potential measurements.

### 6.3.3 *tert*-butyloxycarbonyl protection of 4-[*N*-(methylaminoethyl) aminomethyl] styrene

The protection of 4-[*N*-(methylaminoethyl) aminomethyl] styrene was performed after a modified procedure described by Bold et al. [75]. To a solution of 0.05 g (0.263 mmol) 4-[*N*-(methylaminoethyl)aminomethyl]styrene in 3.0 ml anhydrous THF under argon atmosphere, 0.138 g (0.631 mmol; 2.4 eq.) Di-*t*-butyl dicarbonate and 0.064 g (0.526 mmol; 2 eq.) 4-dimethylaminopyridine were added at 0 °C. The reaction mixture was stirred at room temperature. The formation of the product was monitored by TLC (hexane / EtOAc = 4:1). After 2 h, the reaction mixture was cooled to 0 °C and 5.0 ml  $\text{H}_2\text{O}$  was added. The product was extracted with EtOAc (3 x 5.0 ml). The combined organic layers were washed with 5.0 ml of a saturated NaCl solution, dried over  $\text{Na}_2\text{SO}_4$  and concentrated to afford a slightly yellow oil. The product was purified by column chromatography (hexane / EtOAc = 4:1).

### 6.3.4 Synthesis of *tert*-butyloxycarbonyl-protected *N*-methyl-diaminoethyl-functionalized magnetic nanoparticles

1.0 g of oleate capped  $\text{Fe}_3\text{O}_4$  nanoparticles was re-dispersed in 2.0 g (17.5 mmol) *n*-octane and 50 mg oleic acid (0.17 mmol) for 1 h in a sonication bath followed by the addition of 24.0 g of an aqueous solution of 0.032 mol/l NaOH solution containing 25 mg (0.09 mmol) SDS. The two phase system was sonicated with a tip sonifier for 5 min under ice cooling (60% amplitude, 10 s pulse, 5 s pause) and stirred with a mechanical stirrer at room temperature. At the same time, 1.0 g (9.6 mmol) of styrene was mixed with 50.0 mg (0.22 mmol) hexadecane and 24.0 g of a 0.032 mol/l NaOH solution with 10.0 mg (0.06 mmol) SDS and sonicated with a tip sonifier under ice cooling for 1 min (10% amplitude, 5 s pulse, 5 s pause). The dispersion was added to the magnetite containing dispersion and argon was bubbled through for 7-10 min. 30.0 mg (0.11 mmol) of potassium peroxy disulfate was added to the combined dispersion and the mixture was heated to 80 °C and stirred 40 min. Then 40.0 mg (0.1 mmol) of *tert*-butyl (2-((*tert*-butoxycarbonyl)(methyl)amino)ethyl)(4-vinylbenzyl)carbamate were added and the dispersion was further stirred 7.5 h at 80 °C. Purification of the *N*-methyl-diaminoethyl-functionalized magnetic nanoparticles was carried out magnetically and with centrifugation. The synthesized and purified particles were examined with DLS, TEM and TGA. Furthermore,  $\zeta$ -potential was determined.

### 6.3.5 Deprotection of Boc-protected *N*-methyl-diaminoethyl-functionalized magnetic nanoparticles

300  $\mu\text{l}$  of the 500 rpm dispersion of the boc-protected particles were diluted with 3 ml of a 1 wt.% SDS solution. 5  $\mu\text{l}$  of a concentrated  $\text{H}_2\text{SO}_4$  were added to the dispersion and it was put on a shaker for 24 h.

### 6.3.6 Chain formation of *N*-methyl-diaminoethyl functionalized magnetic nanoparticles with copper complexing

*N*-methyl-diaminoethyl-functionalized magnetic nanoparticles purified with centrifugation were used for the formation of the nanochains linked by a copper complex in a permanent magnetic field. 350  $\mu\text{L}$  of the nanoparticle dispersion was first diluted with 6 ml deionized water to lower the amount of surfactant stabilizing the nanoparticles. 160  $\mu\text{L}$  of a 0.0001 mol/L  $\text{CuCl}_2$  solution were added to the dispersion. A syringe was charged with 6 ml of the  $\text{CuCl}_2$  containing nanoparticle dispersion and then directed through a capillary passing through a permanent ring magnet with a syringe pump with a flow rate of 30 ml/h at room temperature. The formed nanochain dispersion was collected after this process. To determine shape and size of the nanochains, the dispersion was analyzed with DLS, and TEM experiments.

Furthermore, UV/Vis spectra were recorded of the diluted nanoparticle dispersion, the dispersion with added copper solution and the nanochain dispersion to determine if any change in the UV/Vis spectra can be observed for the chain formation.

The stability of the formed chains was also investigated. Therefore, 1 ml of the nanochain dispersion was put in an ultrasound bath for 15 min. To a further 1 ml sample, 60  $\mu\text{l}$  of a 0.032

mol/l NaOH solution were added and it was placed in an ultrasonication bath for 15 min. The samples were investigated with DLS and TEM to determine if any change in size and shape of the nanochains occurred.

The detection of copper in the formed chains was performed with ICP-OES spectrometry. Therefore, a high concentration *N*-methyl-diaminoethyl functionalized nanoparticles was used to generate a high amount of chains. The amount of copper solution added was increased that the dispersion had a copper concentration of 4 mg/l. The formed chains were collected and concentrated in a centrifuge with 2000 rpm for 20 min. The supernatant was removed and the chains were redispersed with 1 wt.% SDS solution. This procedure was repeated five times to remove all free copper ions. The sample was then acidified with 50  $\mu$ l / ml 0.1 HCl solution to release the copper ions. The acidified sample was centrifuged again with 2000 rpm for 20 min and the supernatant was analyzed with ICP-OES.

### **6.3.7 Chain formation of *N*-methyl-diaminoethyl functionalized nanoparticles stabilized with Lutensol with copper complexing**

For the nanochain formation of the *N*-methyl-diaminoethyl functionalized nanoparticles stabilized with Lutensol the same assessment was used as for the SDS stabilized nanoparticles. Size and shape of the formed nanochains were determined with DLS, and TEM experiments, respectively.

### **6.3.8 pH triggered disassembly of the nanochains**

A protonation of the *N*-methyl-diaminoethyl function of the formed copper complexes was chosen for the disassembly step for the nanochains. Therefore, a sample of formed chains was acidified with 0.1 mol/l HCl solution. The sample was acidified stepwise with 1.0  $\mu$ l, 2.5  $\mu$ l, 5.0  $\mu$ l, 10  $\mu$ l, and 15  $\mu$ l of 0.1 mol/l hydrochloric acid per ml nanochain dispersion to determine which amount of hydrochloric acid is necessary to fulfill the disassembly. After each addition of hydrochloric acid, the sample was placed in an ultrasonication bath for 10 min. The acidified samples were examined with DLS, and TEM to detect changes in size and shape of the nanochains. Furthermore, the pH of each sample was determined with a pH electrode.

### **6.3.9 Reassembly of the nanoparticles**

To proof the complete reversibility of this pH triggered assembly/disassembly process, the disassembled particles need to be reassembled in the magnetic field. Therefore, 350  $\mu$ L of the nanoparticle dispersion were first diluted with 6 ml deionized water to lower the amount of surfactant in the dispersion. 160  $\mu$ l of a 0.0001 mol/l  $\text{CuCl}_2$  solution was added to the dispersion. A syringe was charged with 6 ml of this  $\text{CuCl}_2$  containing nanoparticle dispersion and then directed through a capillary passing through a permanent ring magnet with a syringe pump with a flow rate of 30 ml/h at room temperature. The formed nanochain dispersion

was collected after this process. The nanochain sample was then treated with 30  $\mu\text{l}$  of a 0.1 mol/l HCl solution (5  $\mu\text{l}/\text{ml}$  dispersion) and put in an ultrasonication bath for 10 min. The disassembly of the nanochains was recorded with DLS and TEM experiments. 30  $\mu\text{l}$  of a 0.1 mol/l NaOH solution was added to the acidified dispersion and the dispersion was shaken on a mechanical shaker for 15 min. The dispersion was then again pulled up into a syringe and was directed through a capillary passing through the ring magnet with a syringe pump at a flow rate of 30 ml/h. The collected dispersion was examined with DLS, and TEM experiments.

## 6.4 Synthesis of magnetic nanocapsules and polymer film formation

### 6.4.1 Synthesis of magnetic polystyrene nanocapsules

1.0 g of oleate capped  $\text{Fe}_3\text{O}_4$  nanoparticles was re-dispersed in 5.0 g (43.75 mmol) *n*-octane and 50 mg oleic acid (0.17 mmol) for 30 min in a sonication bath followed by the addition of 5.0 g (22 mmol) hexadecane. 24.0 g of an aqueous solution containing 25 mg (0.09 mmol) SDS were added and this mixture was shaken rapidly on a shaker for 2 min and immediately sonicated with a tip sonifier for 5 min under ice cooling (25% amplitude, 10 s pulse, 5 s pause) and stirred with a mechanical stirrer at room temperature. At the same time, 1.0 g (9.6 mmol) of styrene was mixed with 50.0 mg (0.22 mmol) hexadecane and 24.0 g of an aqueous solution with 10.0 mg (0.06 mmol) SDS and sonicated with a tip sonifier under ice cooling for 1 min (10% amplitude, 5 s pulse, 5 s pause). The dispersion was added to the magnetite containing dispersion and argon was bubbled through the combined dispersions for 7-10 min. 30.0 mg (0.11 mmol) of potassium peroxydisulfate was added to the combined dispersion and the mixture was heated to 80 °C and stirred 40 min. Then 30.0 mg (0.1 mmol) of sodium-styrene-sulfonate was added and the dispersion was stirred additional 5.5 h at 80 °C. The organic supernatant was removed and the aqueous dispersion was purified magnetically.

This procedure was also followed with 1.5 g (13.13 mmol) *n*-octane and 8.5 g (37.4 mmol) hexadecane to investigate the influence of the content of hexadecane.

### 6.4.2 Synthesis of magnetic nanocapsules containing DCPD and hexadecane

1.0 g of oleate capped  $\text{Fe}_3\text{O}_4$  nanoparticles was re-dispersed in 2.0 g (17.50 mmol) *n*-octane and 50 mg oleic acid (0.17 mmol) for 30 min in a sonication bath followed by the addition of 3.0 g (13.2 mmol) hexadecane and 5.0 g (37.8 mmol) dicyclopentadiene. 24.0 g of an aqueous solution containing 25 mg (0.09 mmol) SDS was added and this mixture was shaken on a shaker for 2 min and immediately sonicated with a tip sonifier for 5 min under ice cooling (30% amplitude, 10 s pulse, 5 s pause) and stirred with a mechanical stirrer at room temperature. At the same time, 1.0 g (9.6 mmol) of styrene was mixed with 50.0 mg (0.22 mmol) hexadecane and 24.0 g of an aqueous solution with 10.0 mg (0.06 mmol) SDS and sonicated with a tip sonifier under ice cooling for 1 min (10% amplitude, 5 s pulse, 5 s pause). The dispersion was added to the magnetite containing dispersion and argon was bubbled through for 7-10 min. 30.0 mg (0.11 mmol) of potassium peroxydisulfate was added to the combined dispersion and the mixture was heated to 80 °C and stirred 40 min. Then, 30.0 mg (0.1 mmol)



of sodium-styrenesulfonate were added and the dispersion was further stirred for 5.5 h at 80 °C. The organic supernatant was removed and the aqueous dispersion was purified magnetically.

### 6.4.3 Synthesis of P(MMA-co-BA) nanoparticles

The acrylate nanoparticles stabilized with Lutensol AT 50 were synthesized after a procedure described by Lv et al. [76]

A mixture of methyl methacrylate (2.13 ml, 0.02 mol), butyl acrylate (2.25 ml, 0.02 mol), and hexadecane (0.194 ml, 0.66 mmol) was added to 16 ml of water containing 100 mg of Lutensol AT 50 and 10 mg potassium peroxy disulfate. After stirring under 1000 rpm for 1 h at room temperature, the mixture was ultrasonicated for 120 s at 70% amplitude under ice cooling. Before polymerization, the miniemulsion dispersion was degassed with Argon for 10 min. Then the reaction was carried in an oil bath under 72 °C for 20 h. A dispersion of P(MMA-co-BA) nanoparticles was obtained after polymerization.

### 6.4.4 Polymer-film formation

The acrylate films containing magnetic nanocapsules were prepared after a slightly derived method described by Lv et al. [76]

300  $\mu$ l of the DCPD containing magnetic nanocapsule dispersion (1 wt.%) were mixed with 110  $\mu$ l of the P(MMA-co-BA) nanoparticle dispersion (15 wt.%) and stirred for 1 h. The dispersion mixture was then dropcasted on four 10x10 mm Si-wafers (25  $\mu$ l) and three 20x20 mm glass plates (50  $\mu$ l). One of the samples was dried under air atmosphere at room temperature. The other ones were placed on the center of a ring magnet and on the edges and the center of a cuboid magnet and dried under air atmosphere at room temperature on the magnets. The films on the glass plates were examined with optical microscopy, while the ones on the Si-wafers were investigated with SEM, and SEM-EDX experiments.

## 6.5 Superamphiphobic surfaces with magnetic spherical colloidal building blocks

The formation of superamphiphobic surfaces using the magnetic alignment of spherical colloidal building blocks was tested for three different setups. In all cases, a magnetic nanoparticle dispersion was prepared as described in 6.2.3. The application of the magnetic nanoparticles on a Si-wafer surface was achieved by spincoating ozone cleaned 10x10 mm Si-wafer surfaces with a 5 wt.% polystyrene solution ( $M_{W(PS)} = 28\ 100$  g/mol) in toluene with 2000 rpm.

### 6.5.1 First Setup

A concentrated dispersion of the magnetic nanoparticles was dropcasted on a silicon wafer which was placed on a spacer positioned upon a permanent magnet in an oven at 90 °C. The

solvent was allowed to evaporate completely and the created surface was investigated via SEM experiments.

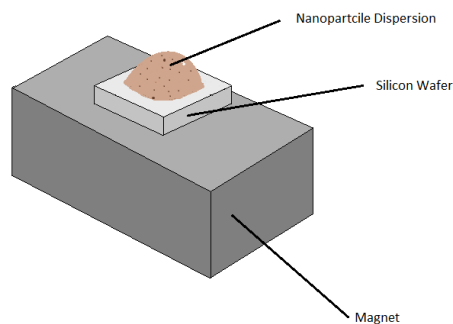


**Figure 6.1:** First setup scheme for superamphiphobic surfaces.

### 6.5.2 Second Setup

To overcome the problems that occurred in the first experimental setup a capillary filled with a highly concentrated nanoparticle dispersion was used instead of the dropcasting. This capillary was pushed onto the wafer surface with a clip and put on the magnet. The surface was investigated with SEM experiments.

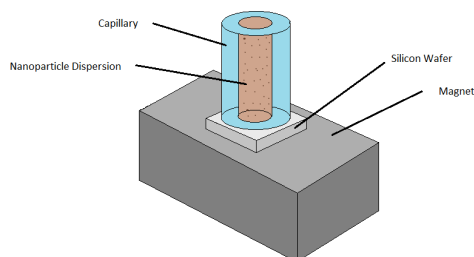


**Figure 6.2:** Second setup scheme for superamphiphobic surfaces.

### 6.5.3 Third Setup

A last experimental setup was tested with the permanent magnet on top of capillary. The conceptual idea was to use a counter force to the magnetic field strength. The gravity decreases the attraction of the magnet and allows a controlled assembly of the nanoparticles.

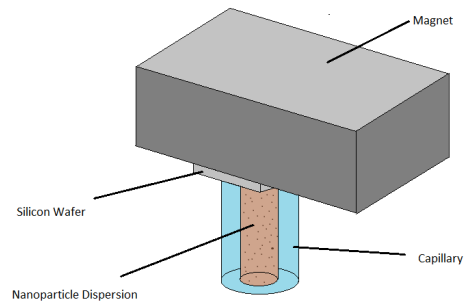


**Figure 6.3:** Third setup scheme for superamphiphobic surfaces.

## 6.6 Chemicals

The following table Table 21 displays the chemicals used in this thesis. All chemicals were used as purchased, except the monomers styrene, methyl-methylacrylate and butyl acrylate, which were purified from the stabilizer by a short column purification with alumina oxide. Deionized water was used for all experiments.

Table 21: Chemicals used for the experiments

Chemical Name	CAS number	Abbreviation	Manufacturer	Purity	other data
2,2-Azobis(2-methylpropanitrile)	78-67-1	AIBN	Acros Organics	98%	stabilized
Ammonia	7664-41-7	NH <sub>3</sub>	VWR	28%	28% aqueous solution
Butyl acrylate	141-32-2	BA	Acros Organics	99+%	stabilized
Dicyclopentadiene	77-73-6	DCPD	-	-	/
4-dimethylaminopyridine	1122-58-3	DMAP	-	99%	/
Di- <i>t</i> -butyl dicarbonate	24424-99-5	Boc <sub>2</sub> O	-	-	/
Copper(II)chloride dihydrate	10125-13-0	CuCl <sub>2</sub> x 2 H <sub>2</sub> O	-	99+%	/
Methyl methacrylate	80-62-6	MMA	Acros Organics	99%	stabilized
Potassium peroxodisulfate	7727-21-1	KPS	Acros Organics	99+%	stabilized
Sodium dodecylsulfate	151-21-3	SDS	Alfa Aesa	99%	/
Lutensol AT 50	68439-49-6	/	BASF	100%	/
Iron(III)chloride hexahydrate	10025-77-1	FeCl <sub>3</sub> x 6 H <sub>2</sub> O	Acros Organics	99+%	/
Iron(II)chloride tetrahydrate	13478-10-9	FeCl <sub>2</sub> x 4 H <sub>2</sub> O	Merck	99%	/
<i>n</i> -octane	111-65-9	/	Merck	99%	/
Oleic acid	112-80-1	OA	Merck	100%	/
Sodium hydroxide	1310-73-2	NaOH	Aldrich	97%	/
Sodium hydroxide aqueous sol.	1310-73-2	NaOH	Roth	/	0.1 mol/l
Hydrochloric acid aqueous sol.	7647-01-0	HCl	Roth	/	0.1 mol/l
4-styrenesulfonic acid, sodium salt	123333-94-8	/	Aldrich	90+%	/
4-[ <i>N</i> -(methylaminoethyl)aminomethyl]styrene	1255640-65-3	/	Aldrich	90+%	/
Hexadecane	544-76-3	HD	Acros Organics	99.8%	/
Polystyrene	/	PS	MPI-P	100%	M <sub>w</sub> ≈ 28 100 g/mol
Ethyl acetate	141-78-6	EtOAc	Aldrich	99.5%	/
<i>n</i> -hexane	110-54-3	/	Fischer	95%	/
Tetrahydrofuran	109-99-9	THF	Acros Organics	99.85%	/
Styrene	100-42-5	/	Aldrich	99%	stabilized

## 6.7 Devices and methods

**Ultrasound:** All samples were sonicated with a Branson Sonifier W450-D, using a 1/2-inch tip. The samples were always cooled with an ice bath.

**Dynamic light scattering:** The hydrodynamic diameter of the synthesized particle-, capsule- and nanochain dispersions were measured with a Nicomp<sup>TM</sup> 380 Submicron Particle Sizer of the company PSS Nicomp. For the measurements the samples were diluted with deionized water until the cloudiness of the sample almost disappeared. Each sample was measured for 4 min at a scattering angle of 90 °. As long as not stated differently, all mean diameters determined with DLS are the mean intensity values.

The determination of the hydrodynamic radii of the nanocapsules was performed with a ALV/CGS3 compact goniometer system with a He/Ne laser (632.8 nm), ALV/LSE-5004 correlator and ALV5000 software

**Transmission Electron Microscope:** All TEM experiments were executed at a JEOL 1400. Images were taken with a GATAN CCD camera and examined with ImageJ.

**Scanning Electron Microscope:** The SEM experiments were executed at a Zeiss 1530 Gemini LEO at different voltages. The images were examined with ImageJ.

**Energy dispersive X-Ray Microscopy:** The EDX spectra were recorded with a Hitachi SU8000 scanning electron microscope, using a Bruker AXS detector.

**Thermogravimetric Analysis:** All samples were measured at a TGA 851 of the company Mettler Toledo. The heating rate was 10 K, the temperature range was from 35 °C to 1000 °C and the measurements were taken out under nitrogen atmosphere.

**ζ-Potential** The ζ-potentials were recorded with a Malvern Zetasizer Nano series. For the measurements the samples were diluted with a 0.1 mol/l KCl solution until the cloudiness of the sample was only slightly visible.

**UV/VIS Spectrometry:** The UV/VIS spectra were recorded with a Lambda 25 UV/VIS spectrometer of the Company Perkin Elmer.

**Inductively Coupled Plasma Atomic Emission Spectroscopy:** The ICP-OES Spectrum was recorded at an ActivaM of the company Horiba.

**Field-Flow Fractionation:** The field flow fractionations were performed with an AFFFF machine from ConSensus GmbH. A P 2.1 flowbox with 2 pumps and an integrated flow control and control valve for the transverse flow control and a ConSensus AFFFF-5.0 channel with glass plate and a RI detector were used. The fractionation was performed in a 10 mmol NaCl solution and examined with the WinFFF3.0 software

## References

- [1] Philipp Reineck, George P Lee, Delia Brick, Matthias Karg, Paul Mulvaney, and Udo Bach. A solid-state plasmonic solar cell via metal nanoparticle self-assembly. *Advanced Materials*, 24(35):4750–4755, 2012.
- [2] De-Liang Long, Eric Burkholder, and Leroy Cronin. Polyoxometalate clusters, nanostructures and materials: from self assembly to designer materials and devices. *Chemical Society Reviews*, 36(1):105–121, 2007.
- [3] Donghai Wang, Rong Kou, Daiwon Choi, Zhenguo Yang, Zimin Nie, Juan Li, Laxmikant V Saraf, Dehong Hu, Jiguang Zhang, Gordon L Graff, et al. Ternary self-assembly of ordered metal oxide- graphene nanocomposites for electrochemical energy storage. *ACS nano*, 4(3):1587–1595, 2010.
- [4] Sara Cavaliere, Surya Subianto, Iuliia Savych, Deborah J Jones, and Jacques Rozière. Electrospinning: designed architectures for energy conversion and storage devices. *Energy & Environmental Science*, 4(12):4761–4785, 2011.
- [5] Stanley S Davis and Lisbeth Illum. Polymeric microspheres as drug carriers. *Biomaterials*, 9(1):111–115, 1988.
- [6] MS Romero-Cano and B Vincent. Controlled release of 4-nitroanisole from poly (lactic acid) nanoparticles. *Journal of controlled release*, 82(1):127–135, 2002.
- [7] Sampath Srinivasan, Vakayil K Praveen, Robert Philip, and Ayyappanpillai Ajayaghosh. Bioinspired superhydrophobic coatings of carbon nanotubes and linear  $\pi$  systems based on the *bottom – up* self-assembly approach. *Angewandte Chemie*, 120(31):5834–5838, 2008.
- [8] Andreas Greiner and Joachim H Wendorff. Elektrospinnen: eine faszinierende methode zur präparation ultradünner fasern. *Angewandte Chemie*, 119(30):5770–5805, 2007.
- [9] Daniel Crespy, Kathrin Friedemann, and Ana-Maria Popa. Colloid-electrospinning: Fabrication of multicompartment nanofibers by the electrospinning of organic or/and inorganic dispersions and emulsions. *Macromolecular rapid communications*, 33(23):1978–1995, 2012.
- [10] Liang Shi, Congjian Pei, Yeming Xu, and Quan Li. Template-directed synthesis of ordered single-crystalline nanowires arrays of  $\text{Cu}_2\text{ZnSnS}_4$  and  $\text{Cu}_2\text{ZnSnSe}_4$ . *Journal of the American Chemical Society*, 133(27):10328–10331, 2011.
- [11] Paulo N Martinho, Tibebe Lemma, Brendan Gildea, Gennaro Picardi, Helge Müller-Bunz, Robert J Forster, Tia E Keyes, Gareth Redmond, and Grace G Morgan. Template assembly of spin crossover one-dimensional nanowires. *Angewandte Chemie International Edition*, 51(48):11995–11999, 2012.



- 
- [12] Benjamin B Yellen. Binary colloidal structures assembled through ising interactions. *nATuRE*, 3(794), 2012.
- [13] Arlin Jose Amali, Padmanapan Saravanan, and Rohit Kumar Rana. Tailored anisotropic magnetic chain structures hierarchically assembled from magnetoresponse and fluorescent components. *Angewandte Chemie International Edition*, 50(6):1318–1321, 2011.
- [14] Markus B Bannwarth, Samuel W Kazer, Sebastian Ulrich, Gunnar Glasser, Daniel Crespy, and Katharina Landfester. Well-defined nanofibers with tunable morphology from spherical colloidal building blocks. *Angewandte Chemie International Edition*, 52(38):10107–10111, 2013.
- [15] Markus B Bannwarth, Thomas Weidner, Evelyn Eidmann, Katharina Landfester, and Daniel Crespy. Reversible redox-responsive assembly/disassembly of nanoparticles mediated by metal complex formation. *Chemistry of Materials*, 26(3):1300–1302, 2014.
- [16] Jiayin Yuan, Youyong Xu, and Axel HE Müller. One-dimensional magnetic inorganic-organic hybrid nanomaterials. *Chemical Society Reviews*, 40(2):640–655, 2011.
- [17] Haibing Xia, Ge Su, and Dayang Wang. Size-dependent electrostatic chain growth of pH-sensitive hairy nanoparticles. *Angewandte Chemie International Edition*, 52(13):3726–3730, 2013.
- [18] Q Lu, Alok Singh, Jeffrey R Deschamps, and EL Chang. Cu (ii)-containing cross-linked polymers for the hydrolysis of 4-nitrophenyl phosphate. *Inorganica Chimica Acta*, 309(1):82–90, 2000.
- [19] Hiroyasu Masunaga, Ayumi Nakano, Kenji Yamamoto, Kazuya Uezu, Kazuo Sakurai, and Isamu Akiba. Metalation-induced micelle formation of a block copolymer in non-selective solvent. *Journal of Physics: Conference Series*, 272(1):012023, 2011.
- [20] Nicholas Wettels, Jeremy A Fishel, and Gerald E Loeb. Multimodal tactile sensor. In *The Human Hand as an Inspiration for Robot Hand Development*, pages 405–429. Springer, 2014.
- [21] Rakesh B Katragadda and Yong Xu. A novel intelligent textile technology based on silicon flexible skins. *Sensors and Actuators A: Physical*, 143(1):169–174, 2008.
- [22] Stefan CB Mannsfeld, Benjamin CK Tee, Randall M Stoltenberg, Christopher V HH Chen, Soumendra Barman, Beinn VO Muir, Anatoliy N Sokolov, Colin Reese, and Zhenan Bao. Highly sensitive flexible pressure sensors with microstructured rubber dielectric layers. *Nature materials*, 9(10):859–864, 2010.
- [23] Wenfeng Zhang, Ying Xu, Haitao Wang, Chenhui Xu, and Shangfeng Yang. Fe<sub>3</sub>O<sub>4</sub> nanoparticles induced magnetic field effect on efficiency enhancement of p3ht: Pcbm bulk heterojunction polymer solar cells. *Solar Energy Materials and Solar Cells*, 95(10):2880–2885, 2011.

- 
- [24] Dieter Weller and Mary F Doerner. Extremely high-density longitudinal magnetic recording media. *Annual review of materials science*, 30(1):611–644, 2000.
- [25] Ajeet Kaushik, Pratima R Solanki, Anees A Ansari, G Sumana, Sharif Ahmad, and Bansi D Malhotra. Iron oxide-chitosan nanobiocomposite for urea sensor. *Sensors and Actuators B: Chemical*, 138(2):572–580, 2009.
- [26] Toshio Ogino, Hiroki Hibino, Yoshikazu Homma, Yoshihiro Kobayashi, Kuniyil Prabhakaran, Koji Sumitomo, and Hiroo Omi. Fabrication and integration of nanostructures on si surfaces. *Accounts of chemical research*, 32(5):447–454, 1999.
- [27] Jong-Hyun Kim, Makoto Yoneya, and Hiroshi Yokoyama. Tristable nematic liquid-crystal device using micropatterned surface alignment. *Nature*, 420(6912):159–162, 2002.
- [28] SUIZHOU Yang, K Yang, LANGANG Niu, Ramaswamy Nagarajan, SHAOPING Bian, Alope K Jain, and Jayant Kumar. Patterning of substrates using surface relief structures on an azobenzene-functionalized polymer film. *Advanced Materials*, 16(8):693–696, 2004.
- [29] Guangzhe Piao, Fumiko Kimura, and Tsunehisa Kimura. Simultaneous alignment and micropatterning of organic crystallites under a modulated magnetic field. *Langmuir*, 22(10):4853–4855, 2006.
- [30] Despina Fragouli, Raffaella Buonsanti, Giovanni Bertoni, Claudio Sangregorio, Claudia Innocenti, Andrea Falqui, Dante Gatteschi, Pantaleo Davide Cozzoli, Athanassia Athanassiou, and Roberto Cingolani. Dynamical formation of spatially localized arrays of aligned nanowires in plastic films with magnetic anisotropy. *ACS nano*, 4(4):1873–1878, 2010.
- [31] Masaki Nakahata, Yoshinori Takashima, Hiroyasu Yamaguchi, and Akira Harada. Redox-responsive self-healing materials formed from host–guest polymers. *Nature communications*, 2:511, 2011.
- [32] Yoshifumi Amamoto, Hideyuki Otsuka, Atsushi Takahara, and Krzysztof Matyjaszewski. Self-healing of covalently cross-linked polymers by reshuffling thiuram disulfide moieties in air under visible light. *Advanced Materials*, 24(29):3975–3980, 2012.
- [33] Scott R White, NR Sottos, PH Geubelle, JS Moore, M\_R Kessler, SR Sriram, EN Brown, and S Viswanathan. Autonomic healing of polymer composites. *Nature*, 409(6822):794–797, 2001.
- [34] José L Mietta, Mariano M Ruiz, P Soledad Antonel, Oscar E Perez, Alejandro Butera, Guillermo Jorge, and R Martín Negri. Anisotropic magnetoresistance and piezoresistivity in structured fe<sub>3</sub>o<sub>4</sub>-silver particles in pdms elastomers at room temperature. *Langmuir*, 28(17):6985–6996, 2012.
-

- 
- [35] Gerhard Lagaly, Oliver Schulz, and Ralf Zimehl. *Dispersionen und emulsionen. Steinkopff-Verlag, Darmstadt, 1997.*
- [36] Hans-Dieter Dörfler. *Grenzflächen und kolloid-disperse Systeme: Physik und Chemie; mit 88 Tabellen.* Springer, 2002.
- [37] Hans-Jürgen Butt, Karlheinz Graf, and Michael Kappl. *Physics and chemistry of interfaces.* John Wiley & Sons, 2006.
- [38] Katharina Landfester, Mirjam Willert, and Markus Antonietti. Preparation of polymer particles in nonaqueous direct and inverse miniemulsions. *Macromolecules*, 33(7):2370–2376, 2000.
- [39] Katharina Landfester. Polyreactions in miniemulsions. *Macromolecular Rapid Communications*, 22(12):896–936, 2001.
- [40] K Landfester. Synthesis of colloidal particles in miniemulsions. *Annu. Rev. Mater. Res.*, 36:231–279, 2006.
- [41] S Tesch and H Schubert. Influence of increasing viscosity of the aqueous phase on the short-term stability of protein stabilized emulsions. *Journal of food engineering*, 52(3): 305–312, 2002.
- [42] Constantinos M Paleos. *Polymerization in organized media.* CRC Press, 1992.
- [43] Markus Antonietti, Rainer Basten, and Sabine Lohmann. Polymerization in microemulsions a new approach to ultrafine, highly functionalized polymer dispersions. *Macromolecular Chemistry and Physics*, 196(2):441–466, 1995.
- [44] D. Hunkeler, F. Candau, C. Pichot, A. E. Hamielec, T. Y. Xie, J. Barton, V. Vaskova, J. Guillot, M. V. Dimonie, and K. H. Reichert. . *Advances in Polymer Science*, 112: 115–133, 1994.
- [45] Katharina Landfester. Recent developments in miniemulsions-formation and stability mechanisms. *Macromolecular Symposia*, 150(1):171–178, 2000.
- [46] Katharina Landfester. Miniemulsion polymerization and the structure of polymer and hybrid nanoparticles. *Angewandte Chemie International Edition*, 48(25):4488–4507, 2009.
- [47] Bernadette Charleux, Franck D Agosto, and Guillaume Delaittre. Preparation of hybrid latex particles and core-shell particles through the use of controlled radical polymerization techniques in aqueous media. In *Hybrid Latex Particles*, pages 125–183. Springer, 2010.
- [48] CS Chern, TJ Chen, and YC Liou. Miniemulsion polymerization of styrene in the presence of a water-insoluble blue dye. *Polymer*, 39(16):3767–3777, 1998. See also preceding publications of Chern.

- 
- [49] Anna Musyanovych, Renate Rossmanith, Christian Tontsch, and Katharina Landfester. Effect of hydrophilic comonomer and surfactant type on the colloidal stability and size distribution of carboxyl- and amino-functionalized polystyrene particles prepared by miniemulsion polymerization. *Langmuir*, 23(10):5367–5376, 2007.
- [50] Cédric Vancaeyzeele, Olga Ornatsky, Vladimir Baranov, Lei Shen, Ahmed Abdelrahman, and Mitchell A Winnik. Lanthanide-containing polymer nanoparticles for biological tagging applications: nonspecific endocytosis and cell adhesion. *Journal of the American Chemical Society*, 129(44):13653–13660, 2007.
- [51] Sonja Theisinger, Katrin Schoeller, Barry Osborn, Manish Sarkar, and Katharina Landfester. Encapsulation of a fragrance via miniemulsion polymerization for temperature-controlled release. *Macromolecular Chemistry and Physics*, 210(6):411–420, 2009.
- [52] Clemens K Weiss and Katharina Landfester. Miniemulsion polymerization as a means to encapsulate organic and inorganic materials. In *Hybrid Latex Particles*, pages 185–236. Springer, 2010.
- [53] S Lelu, C Novat, C Graillat, A Guyot, and E Bourgeat-Lami. Encapsulation of an organic phthalocyanine blue pigment into polystyrene latex particles using a miniemulsion polymerization process. *Polymer International*, 52(4):542–547, 2003.
- [54] Nina Bechthold, Franca Tiarks, Mirjam Willert, Katharina Landfester, and Markus Antonietti. Miniemulsion polymerization: applications and new materials. *Macromolecular Symposia*, 151(1):549–555, 2000.
- [55] Bedri Erdem, E David Sudol, Victoria L Dimonie, and Mohamed S El-Aasser. Encapsulation of inorganic particles via miniemulsion polymerization. i. dispersion of titanium dioxide particles in organic media using oloa 370 as stabilizer. *Journal of Polymer Science Part A: Polymer Chemistry*, 38(24):4419–4430, 2000.
- [56] Dirk Hoffmann, Katharina Landfester, and Markus Antonietti. Encapsulation of magnetite in polymer particles via the miniemulsion polymerization process. *Magneto-hydrodynamics*, 37:217–221, 2001.
- [57] Christine Herrmann, Markus B Bannwarth, Katharina Landfester, and Daniel Crespy. Re-dispersible anisotropic and structured nanoparticles: Formation and their subsequent shape change. *Macromolecular Chemistry and Physics*, 213(8):829–838, 2012.
- [58] Franca Tiarks, Katharina Landfester, and Markus Antonietti. Encapsulation of carbon black by miniemulsion polymerization. *Macromolecular chemistry and physics*, 202(1): 51–60, 2001.
- [59] Nico Steiert and Katharina Landfester. Encapsulation of organic pigment particles via miniemulsion polymerization. *Macromolecular Materials and Engineering*, 292(10-11): 1111–1125, 2007.

- 
- [60] Liliana P Ramirez and Katharina Landfester. Magnetic polystyrene nanoparticles with a high magnetite content obtained by miniemulsion processes. *Macromolecular Chemistry and Physics*, 204(1):22–31, 2003.
- [61] Franca Tiarks, Katharina Landfester, and Markus Antonietti. Preparation of polymeric nanocapsules by miniemulsion polymerization. *Langmuir*, 17(3):908–918, 2001.
- [62] Yingwu Luo and Xiangdong Zhou. Nanoencapsulation of a hydrophobic compound by a miniemulsion polymerization process. *Journal of Polymer Science Part A: Polymer Chemistry*, 42(9):2145–2154, 2004.
- [63] John MD Coey. *Magnetism and magnetic materials*. Cambridge University Press, 2010.
- [64] Nicola A. Spaldin. *Magnetic materials - fundamentals and applications*. Cambridge University Press, 2011.
- [65] Ralf Alsfasser and Erwin Riedel. *Moderne anorganische chemie*. Walter de Gruyter, 2007.
- [66] BJ Blaiszik, NR Sottos, and SR White. Nanocapsules for self-healing materials. *Composites Science and Technology*, 68(3):978–986, 2008.
- [67] Yi Zhao, Johannes Fickert, Katharina Landfester, and Daniel Crespy. Encapsulation of self-healing agents in polymer nanocapsules. *Small*, 8(19):2954–2958, 2012.
- [68] Johannes Fickert, Patrick Rupper, Robert Graf, Katharina Landfester, and Daniel Crespy. Design and characterization of functionalized silica nanocontainers for self-healing materials. *Journal of Materials Chemistry*, 22(5):2286–2291, 2012.
- [69] Gestis Stoffdatenbank. Iron (ii,iii) oxide. website, 2014. requested 14.08.2014 16:02.
- [70] Diandra L Leslie-Pelecky and Reuben D Rieke. Magnetic properties of nanostructured materials. *Chemistry of materials*, 8(8):1770–1783, 1996.
- [71] D Rickwood. *Centrifugation: A practical approach. ed.*. Oxford (United Kingdom), IRL Press, 1984.
- [72] Wolfgang Schärtl. *Light Scattering from Polymer Solutions and Nanoparticle Dispersions: With 16 Tables*. Springer, 2007.
- [73] David B Williams and C Barry Carter. *The Transmission Electron Microscope*. Springer, 1996.
- [74] Joseph I Goldstein, Dale E Newbury, Patrick Echlin, David C Joy, Charles Fiori, Eric Lifshin, et al. *Scanning electron microscopy and X-ray microanalysis. A text for biologists, materials scientists, and geologists*. Plenum Publishing Corporation, 1981.

- [75] Guido Bold, Heinz Steiner, Luzia Moesch, and Bernhard Walliser. Herstellung von semialdehyd-derivaten von asparaginsaeure-und glutaminsaeure durch rosenmund-reduktion. *Helvetica Chimica Acta*, 73(2):405–410, 1990.
- [76] Li-Ping Lv, Yi Zhao, Nicole Vilbrandt, Markus Gallei, Ashokanand Vimalanandan, Michael Rohwerder, Katharina Landfester, and Daniel Crespy. Redox responsive release of hydrophobic self-healing agents from polyaniline capsules. *Journal of the American Chemical Society*, 135(38):14198–14205, 2013.

*It always seems impossible until it's done.*  
- Nelson Mandela 1918 - 2013

## Acknowledgments

I would like to put my gratitude to Prof. Dr. Katharina Landfester for the provision of the interesting and challenging topic and the perfect working conditions I experienced at the institute. I would also like to thank Dr. Daniel Crespy for the excellent support and instruction during the thesis and his patience with the corrections.

Furthermore, I would like to thank:

- The Landfester group for the nice and friendly atmosphere i was welcomed with.
- Dr. Markus B. Bannwarth for fruitful discussions and proposals and the introduction into the project.
- Dipl. Ing. Gunnar Glasser for performing the SEM-EDX experiments and for helpful ideas concerning the polymer films.
- Dr Kristin Mohr, Christine Rosenauer, and Hueseyin Uzun for discussions on the nanocapsules, the AFFFF and DLS measurements of the magnetic nanocapsules.
- Max Bernhardt for the cryo-TEM measurements.
- Max Hofmann for the centrifugations of the magnetic polystyrene nanoparticles.
- Diego Estupinan for discussions on the magic of the magnetic nanoparticle formation.
- Sabrina Brand, Sarah Wald, and Shuai Jiang for the entertaining atmosphere in the lab.

My highest gratitude is dedicated to my family, especially my parents and my grandmother. I would have never come this far without your education, help, and support. I would like to thank Anna for her patience during this period.

*In a world of compromise... some don't.*  
- Karl Willets 2005